

INFORMATION TO USERS

This manuscript has been reproduced from the microfilm master. UMI films the text directly from the original or copy submitted. Thus, some thesis and dissertation copies are in typewriter face, while others may be from any type of computer printer.

The quality of this reproduction is dependent upon the quality of the copy submitted. Broken or indistinct print, colored or poor quality illustrations and photographs, print bleedthrough, substandard margins, and improper alignment can adversely affect reproduction.

In the unlikely event that the author did not send UMI a complete manuscript and there are missing pages, these will be noted. Also, if unauthorized copyright material had to be removed, a note will indicate the deletion.

Oversize materials (e.g., maps, drawings, charts) are reproduced by sectioning the original, beginning at the upper left-hand corner and continuing from left to right in equal sections with small overlaps.

ProQuest Information and Learning
300 North Zeeb Road, Ann Arbor, MI 48106-1346 USA
800-521-0600

UMI[®]

**Tropical Climate Sensitivities: Clouds, Water Vapor, Radiation and Large-Scale
Circulation**

Kristin Ann Larson

**A dissertation submitted in partial fulfillment of the
requirements for the degree of**

Doctor of Philosophy

University of Washington

2002

Program Authorized to Offer Degree: Department of Atmospheric Sciences

UMI Number: 3062975

UMI[®]

UMI Microform 3062975

Copyright 2002 by ProQuest Information and Learning Company.
All rights reserved. This microform edition is protected against
unauthorized copying under Title 17, United States Code.

ProQuest Information and Learning Company
300 North Zeeb Road
P.O. Box 1346
Ann Arbor, MI 48106-1346

In presenting this dissertation in partial fulfillment of the requirements for the Doctoral degree at the University of Washington, I agree that the Library shall make its copies freely available for inspection. I further agree that extensive copying of this dissertation is allowable only for scholarly purposes, consistent with "fair use" as prescribed in the U.S. Copyright Law. Requests for copying or reproduction of this dissertation may be referred to Bell and Howell Information and Learning, 300 North Zeeb Road, Ann Arbor, MI 48106-1346, to whom the author has granted "the right to reproduce and sell (a) copies of the manuscript in microform and/or (b) printed copies of the manuscript made from microform."

Signature: Kristen Larson

Date: Aug 5, 2002

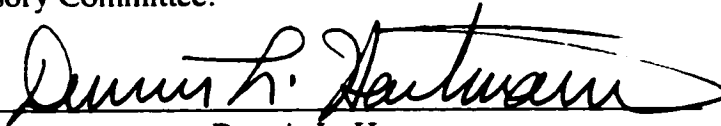
University of Washington
Graduate School

This is to certify that I have examined this copy of a doctoral dissertation by

Kristin Ann Larson


and have found that it is complete and satisfactory in all respects,
and that any and all revisions required by the final
examining committee have been made.

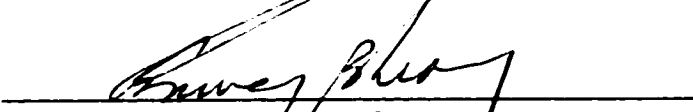
Chair of Supervisory Committee:


Dennis L. Hartmann

Reading Committee:


Christopher S. Bretherton


Dennis L. Hartmann


Conway Leovy

Date: Aug. 5, 2002

University of Washington

Abstract

**Tropical Climate Sensitivities: Clouds, Water Vapor,
Radiation and Large-Scale Circulation**

by Kristin Ann Larson

Chairperson of the Supervisory Committee:

Professor Dennis L. Hartmann

Department of Atmospheric Sciences

The physical mechanisms that affect the tropical sea surface temperature (SST) are investigated using a two box model and a mesoscale model with fixed uniform and sinusoidal SST gradients. Emphasis is placed on the large-scale circulation containing rising motion in regions with high humidity and high clouds and subsidence in regions with low upper tropospheric humidity, a trade inversion and low clouds. Changes in the area of the convective region are investigated as are effects of the high and low clouds. The results show that water vapor feedback in clear skies depends on the height of the moist boundary layer.

Radiative cooling in the cold pool constrains the large-scale circulation strength. The strength of the circulation decreases with increasing convective area, because the increase in dry static stability overwhelms the increase in cooling rate in the two box model and the mesoscale model with SST gradients.

For simulations with constant fixed SST and zero mean vertical motion, the sensitivities of the top of the atmosphere radiative quantities to SST are similar to observations comparing El Niño and La Niña SSTs and radiative quantities when averaged over an area including the ascending and descending branches of the tropical large-scale circulation. These simulations also show that the clear-sky temperature and water

vapor feedbacks are of about equal magnitude in opposite directions, and the lapse rate feedback is negative with a magnitude of approximately $2 \text{ W m}^{-2} \text{ K}^{-1}$.

Shortwave cloud forcing is related to the strength of the large-scale circulation in the SST gradient simulations. The longwave radiative cooling at the top of stratus clouds enhances the large-scale circulation. Increasing the mesoscale model SST gradient strengthens the large-scale circulation and decreases the average net absorbed shortwave radiation.

Table of Contents

List of Figures	iii
List of Tables	vi
Chapter 1: Introduction	1
Chapter 2: Two Box Model	4
2.1 Introduction	4
2.2 Model Description	5
2.2.1 Concept	5
2.2.2 Cold Pool Boundary Layer (CPBL) Equations	10
2.2.3 Tropospheric Energy Balance Equations	13
2.2.4 Ocean Energy Balance Equations	14
2.2.5 Moisture Budget Equations	15
2.2.6 Solution Procedure	19
2.3 Model Sensitivities	20
2.3.1 Base Climate	20
2.3.2 Area Ratio and Moisture Budget	23
2.3.3 Moisture Budget: Cold Pool Humidity	27
2.3.4 Warm pool cloud sensitivity	30
2.3.5 Cold pool boundary layer cloud sensitivity	31
2.3.6 CPBL Predicted Cloud Fraction	32
2.3.7 Surface wind speed	34
2.4 Climate Sensitivities to Doubled Carbon Dioxide	36
2.5 Summary and Conclusions	38
Chapter 3: Uniform SSTs	42
3.1 Introduction	42
3.2 Model Description	45
3.2.1 Dynamics	45
3.2.2 Boundaries	45
3.2.3 Physics	46
3.2.4 Radiation	47
3.2.5 Experiments	49
3.3 Atmospheric Sensitivities to SST	49
3.3.1 Temperature and Humidity	50
3.3.2 Convective Area Fraction	58

3.4 Comparison with Observed Sensitivities of Energy Budget to SST	64
3.4.1 Accounting for Diurnal Variations	66
3.4.2 Comparison to Observations.	68
3.5 Cloud, Water Vapor and Lapse Rate Feedbacks	70
3.6 Summary and Conclusions	76
Chapter 4: SST Gradients	79
4.1 Introduction	79
4.2 Model Description and Validation	81
4.3 Large-Scale Circulation, Maximum SST, and SST Gradients	91
4.4 Rain and Clouds	99
4.5 Radiation	101
4.6 Conclusions	103
Chapter 5: Conclusions	106
Bibliography	109

List of Figures

Figure 2.1 Schematic of model..5

Figure 2.2 Vertical profiles from control case with the relative area of the warm pool equal to 0.3333 a) Temperature and relative humidity vertical profiles in the warm pool. b) Temperature and relative humidity vertical profiles in the cold pool..8

Figure 2.3 SST versus relative warm pool area..23

Figure 2.4 Variable sensitivities as the relative area of the warm pool increases a) Subsidence, strength of the circulation b) Specific humidity above the trade inversion in the cold pool. Solid line is for predicted moisture and dashed line is for fixed humidity..25

Figure 2.5 Comparison of equilibrium solutions for experiments using the moisture budget (solid) and for experiments when the humidity is specified as a constant (dashed)..26

Figure 2.6 SST in the warm and cold pools versus specific humidity above the inversion..27

Figure 2.7 Height of the inversion verses the specific humidity above the inversion..28

Figure 2.8 SST versus warm pool cloud fraction..30

Figure 2.9 SST versus varying cold pool cloud fraction..32

Figure 2.10 Low cloud fraction and SST versus warm pool area fraction..33

Figure 2.11 SST versus surface wind speed..34

Figure 2.12 a) Profiles of equivalent potential temperature for different surface wind speeds: 5.2 m s^{-1} in cold pool (dashed) and 8 m s^{-1} surface wind speed in cold pool (solid) b) Height of the cloud layer versus surface wind speed..35

Figure 3.1 Vertical profiles of relative humidity, moist static energy, and saturated moist static energy for the 4 different SSTs, 297 K (thin solid), 299 K (thin dashed), 301 K (thick dashed), and 303 K (thick solid). Average upper tropospheric relative humidity versus SST..	.50
Figure 3.2 Integrated water vapor versus SST for the MM5, CRMs, and observations..	.52
Figure 3.3 Average values of the rain rate and radiative cooling for the 4 different SSTs..	.54
Figure 3.4 Vertical profiles of temperature tendency for the radiation and moist convection and condensation terms of the energy budget for the 4 different SSTs, 297 K (thin solid), 299 K (thin dashed), 301 K (thick dashed), and 303 K (thick solid)..	.55
Figure 3.5 Vertical profiles of cloud water and cloud ice for the 4 different SSTs, 297 K (thin solid), 299 K (thin dashed), 301 K (thick dashed), and 303 K (thick solid)..	.56
Figure 3.6 Average values of the integrated cloud liquid water, and integrated cloud ice and the sum of all cloud water..	.57
Figure 3.7 Clear-sky, high, middle, and low cloud amount for the constant SST experiments. The line type denotes the cloud type..	.58
Figure 3.8 Fraction of the domain above the convective threshold for integrated cloud ice, and rain rate..	.59
Figure 3.9 Relative humidity, upper tropospheric relative humidity and vertical velocity for the convective and non-convective regions for composites based on integrated cloud ice. Four different SSTs and the 95% confidence limits are noted, 297 K (thin solid), 299 K (thin dashed), 301 K (thick dashed), and 303 K (thick solid)..	.62
Figure 3.10 Vertical profiles of relative humidity, cloud water and temperature for the convective and non-convective regions for composites based on integrated cloud ice..	.63
Figure 3.11 OLR, net absorbed shortwave radiation and net incoming radiation at the top of the atmosphere..	.65

Figure 3.12 Cloud top pressure, cloud visible optical depth, longwave cloud forcing and shortwave cloud forcing for the constant SST experiments..	75
Figure 4.1 SST vs. longitude..	83
Figure 4.2 Temperature profiles for the warm and cold pools..	84
Figure 4.3 Relative humidity cross section vs. longitude for ECMWF and NCEP reanalysis and model data..	85
Figure 4.4 Vertical pressure velocity cross section vs. longitude for ECMWF and NCEP reanalysis and model data..	86
Figure 4.5 Zonal mass flux cross section vs. longitude for ECMWF and NCEP reanalysis and model data..	87
Figure 4.6 Percentage of clouds vs. longitude for ISCCP and model data..	88
Figure 4.7 OLR vs. Longitude for ERBE and model data..	89
Figure 4.8 The net absorbed solar radiation vs. longitude for ERBE and model data..	90
Figure 4.9 SST distributions for five different simulations. M300R4 stands for a mean SST of 300 K and a SST range of 4 K, other abbreviations also show the mean and range of the SST distribution..	91
Figure 4.10 Cloud liquid water, and cloud ice for simulations M300R4, M300R6, M300R8. The contours of cloud ice are labeled in g kg^{-1}	92
Figure 4.11 The temperature tendency for the dynamics, moist convection and condensation, and radiation in K day^{-1} for the experiment with a SST mean of 300 K and a range of 4K..	93
Figure 4.12 Zonal mass flux averaged over latitude for 30 days for the realistic simulation with a mean SST of 300 K and a SST range of 8 K..	95
Figure 4.13 The high cloud amount, low cloud amount, average OLR, and clear-sky OLR or each longitudinal grid-point for the third 30 days of the experiment..	100

List of Tables

Table 2.1 External parameter values for two box model base case	19
Table 2.2 Base case solution state variables for the two box model.	21
Table 2.3 Boundary layer results for changing divergence profiles	22
Table 2.4 Change in tropical mean SST with doubled carbon dioxide.	37
Table 2.5 Doubled carbon dioxide and moisture prediction.	37
Table 3.1 The sensitivity of radiative energy balance components to SST.	69
Table 3.2 Clear-sky feedback factors (299 base) obtained from off-line calculations using averaged model results and a radiative transfer model.	72
Table 3.3 Clear-sky feedback factors (301 base) obtained from off-line calculations using averaged model results and a radiative transfer model.	72
Table 3.4 Feedback factors obtained from the TOA fluxes of the 12 uniform SST experiments	74
Table 4.1 The maximum zonal mass flux values in the upper and lower troposphere for 5 experiments with sinusoidal SST gradients.	96
Table 4.2 The rain rate, rain area and high and low cloud cover amounts for 5 experiments with sinusoidal SST gradients..	99
Table 4.3 Radiation quantities at the top of the atmosphere averaged over latitude and for 30 days for 5 experiments with sinusoidal SST gradients.	102

Acknowledgments

This work could not have proceeded without the generous support and guidance of a number of people. Professor Dennis Hartmann has provided guidance and computer resources. Professor Chris Bretherton has given some insightful comments and been a careful reader. Thank you to Professor Conway Leovy for serving on my reading committee. I also thank the other members of the Supervisory Committee, Professors Robert Houze, Luanne Thompson and Richard Stewart, for their assistance.

Between Jim McCaa and Marc Michelsen, my computing and programming questions were always answered in a timely and thorough manner. Valuable advice from Stephen Klein initiated this project. Thank you to students Miriam Zuk, Chris Killingstad and Phil Regulski for working on this project with me.

This work was supported through a NASA Global Change Fellowship.

Finally, I wish to thank my personal friends, family, union members, and co-counselors for their support, including Ken Lang, who belongs in all those categories.

Chapter 1: Introduction

In recent years scientists have expended much effort attempting to better understand the sensitivity of the tropical climate. At temperatures near those of warm waters of the tropical ocean, the absorption of longwave radiation by water vapor increases rapidly with temperature. As a result, longwave cooling of the surface actually decreases with increasing temperature (e. g. Raval and Ramanathan 1989; Hartmann 1994; Inamdar and Ramanathan 1994). The positive feedback on the tropical climate due to water vapor is strong. The lapse rate feedback alters this positive feedback, because the moist adiabatic lapse rate decreases significantly with temperature in the tropics (e.g. Cess 1975; Knutson and Manabe 1995). Convection, clouds and water vapor have the potential to produce large positive or negative feedbacks in the climate system. Thus, it is important to identify mechanisms that regulate the tropical sea surface temperature (SST).

Cloud response to climate change is one of the largest uncertainties in climate prediction (Cess et al. 1996). Deep tropical convective clouds have tops near the tropopause, produce rain and have a radiative forcing at the top of the atmosphere of approximately zero (Harrison et al. 1990). If the albedo of tropical convective clouds is very sensitive to SST in the tropics, then this can produce a strong negative feedback (Ramanathan and Collins 1991). The areal coverage of high clouds in the tropics may change with SST, which could constitute a strong feedback through the radiative effects of clouds or water vapor (Larson et al. 1999; Lindzen et al. 2001). However, cloud models suggest that large-scale convergence is more important than SSTs in generating high cloud albedos (Lau et al. 1994), and observations suggest that cloud radiative forcing is better correlated with large-scale divergence than with SST (e.g.

Hartmann and Michelsen 1993). If the temperature of high cloud tops decreases with increasing SST, it will be a positive feedback on the tropical climate. It is reasonable to expect the cloud tops to increase in height because the strength of convection might increase with increasing equivalent potential temperature at the surface, and the altitude of the freezing level in the atmosphere will increase with increasing SST as the temperature is moist adiabatic where convection is found.

Boundary layer clouds are found in regions of tropical subsidence with low upper tropospheric relative humidity. These clouds have a strong negative radiative forcing at the top of the atmosphere. Changes in the areal coverage of these clouds may provide a strong climate feedback (Miller 1997). Miller (1997) used an empirical relationship between lower tropospheric stability (LTS) and stratus cloud amount from Klein and Hartmann (1993) to predict a negative feedback.

The large-scale circulation drives changes in cloud albedo in regions where SSTs warm during El Niño/Southern Oscillation (ENSO) events and offsetting changes of opposite sign in adjacent regions (Hartmann and Michelsen 1993). Large-scale dynamics cause the atmosphere above the warmest waters to communicate rapidly with the atmosphere above cooler water (e.g. Fu et al. 1992; Wallace 1992). Because of the important role of water vapor, the ratio of the area of the tropics dominated by subsidence compared to the moist, convective region of the tropics is a critical quantity. This is because the tropics cool to space more efficiently in the subsidence regions without thick high clouds and with low upper tropospheric humidities (Pierrehumbert 1995). Changes in the extent of the humid and dry regions with SST could cause a large feedback.

There are many suggested atmospheric physical mechanisms for the apparent stability of tropical SSTs. Ocean dynamics also have been suggested as a mechanism that can moderate tropical SSTs (Clement et al. 1996; Sun and Liu 1996).

Many questions addressed by the previous studies about the tropical climate remain at issue. What effects do the Hadley and Walker circulations have on tropical climate change? How does the amount of convective cloud affect the tropical SST locally and in remote regions? How do stratus cloud decks in the subsidence region of the tropics interact with the highly convective regions? How is the upper tropospheric humidity in subsidence regions affected by changes in SST? What is the fraction of convecting versus subsidence regions in the tropics and how does it change with SST? What implications do these changes have for climate sensitivity? What climate feedbacks are most important in the tropics, and how will they affect the global climate when the amount of carbon dioxide is doubled?

This thesis seeks to answer these questions using models of the tropical climate. Chapter 2 focuses on the results of a two box model of the tropics. Chapters 3 and 4 give results using a mesoscale model with fixed uniform SST and sinusoidal SST gradients. The thesis concludes in chapter 5.

Chapter 2: Two Box Model

2.1 Introduction

Physical mechanisms of the tropical climate are investigated in this chapter using a two box equilibrium energy and moisture balance model. More specifically, the humidity above the inversion in the subsiding regions will be predicted and its role in climate sensitivity addressed. The simple model includes the interaction between a warm SST region where deep convection occurs (referred to as the warm pool) and another tropical region where the SST is slightly lower and convection is suppressed by large-scale subsidence (the cold pool). These regions are connected by heat and water vapor budgets, and temperature, humidity and the mass circulation between the regions are predicted. Ocean fluxes, atmospheric heat export to the extratropics, surface wind speed, and cloud optical properties are all external parameters for the present implementation of the model. Unlike previous two box models, (Miller, 1997, Pierrehumbert, 1995, Clement and Seager, 1999) the trade inversion height is determined by the model and the moisture in the upper troposphere of the cold pool is predicted.

The response of the equilibrium model climate to the radiative forcing associated with low and high clouds in the tropics and to changes in the area of the convective region is investigated. The interaction of the convective and subsidence regions of the tropics and related changes in temperature, moisture, and circulation are discussed. In particular, the boundary layer depth interacts strongly with free-troposphere humidity in the subsiding region to produce a negative feedback.

2.2 Model Description

2.2.1 Concept

A two box energy balance model is shown schematically in Figure 2.1. The con-

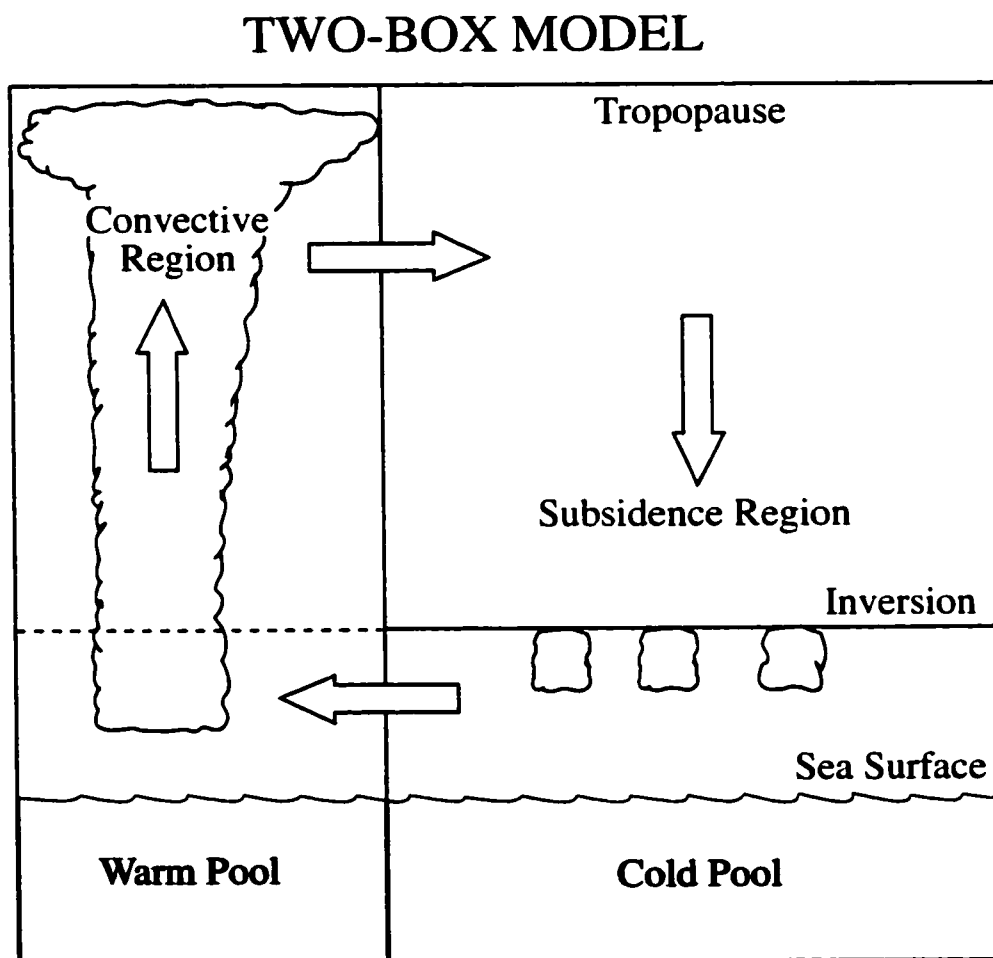


Figure 2.1 Schematic of model. The warm pool has high convective clouds and the cold pool has boundary layer clouds. Air is rising in the warm pool and sinking across the inversion in the cold pool. The top of the energy balance model is at the tropopause.

ective region (warm pool box) refers to the region of the tropics that has deep convection, high humidity throughout the depth of the atmosphere and mean upward motion. In nature the size and location of this region varies with season and on other times-

cales, but the relative area of the convective region is an externally specified parameter in this energy balance model. The subsidence region (cold pool box) is assumed to be that part of the tropics with a trade inversion, descending dry air above the inversion, some low clouds below the inversion, but no deep convection. This two box structure captures a physically important aspect of the tropical climate in a very simple yet informative way.

The convective region atmosphere is assumed to be influenced by the deep convection, so the temperature profile there is fixed to a moist adiabat. Observations show the temperature profile in the tropics closely approximates a moist adiabat (Xu and Emanuel, 1989). The value of the moist adiabat is determined by the equivalent potential temperature of air near the sea surface of the convecting region. Using the small area of convecting clouds, Miller (1997) derived theoretically that in a two box model the warm pool surface and tropopause are linked by a moist adiabat. Other effects of convection are not explicitly treated.

Due to the very large tropical radius of deformation, the horizontal gradients in temperature across the tropics above the boundary layer are small (Schneider, 1977, Held and Hou, 1980). Consequently the free tropospheric temperatures in the warm and cold pool boxes are assumed to be the same at every level above the inversion (Pierrehumbert, 1995). The humidities in the two boxes are predicted from large-scale balance conditions.

The circulation in the model, composed of mean rising motion in the convective region and sinking motion in the subsidence region, approximates the Hadley and Walker circulations in the tropics. For example, the warm pool may represent the region with the warmest water in the Western tropical Pacific and Indian Oceans. One can think of the cold pool as the subsidence regions on all sides of the warm pool. The energy flux between the convective and subsidence regions is equal to the difference in energy between the upper and lower branches of the model circulation times the

strength of the circulation. This large-scale circulation brings water vapor, which is evaporated from the cold pool ocean, to the convective region where it is condensed and rained out. The return flow at upper levels brings much drier air with a higher total energy back to the cold pool. Because the moist static energy of the air exported to the cold pool is necessarily greater than the moist static energy of the air imported from the cold pool, the large-scale circulation removes heat from the convective box. Since the inflow to the warm pool is assumed to occur below the inversion, the strength of the circulation is driven by the subsidence at the top of the trade inversion, which is determined by the balance between radiative cooling and subsidence warming in the atmosphere above the inversion.

The model determines the equilibrium climate by requiring energy balance in both the atmosphere and ocean. Energy balance equations are applied for the boundary layer, the sub-cloud layer, the troposphere and the entire column. Energy exports to the extratropics are prescribed for both the atmosphere and ocean.

One aspect of this model that differs from previous models of this type is that the humidity is predicted from moisture budget equations for each part of the model: the warm pool troposphere, the cold pool free troposphere, and the cloud-topped boundary layer. Although the integrated water is predicted, the humidity profiles in some regions are assumed. In the convective region the relative humidity is assumed constant with height throughout the atmosphere. This profile is in rough agreement with the mean relative humidity profile found during the active phase of the intraseasonal oscillation during the Tropical Ocean Global Atmosphere Coupled Ocean-Atmosphere Experiment (TOGA COARE) field project (Brown and Zhang, 1997). The specific value of relative humidity in the warm pool is predicted by the moisture budget. In the subsidence region the humidity above the inversion is predicted from the moisture budget above the level of the inversion, but the profile is assumed, for simplicity, to be that specified by Manabe and Wetherald (1967). In principle, the humidity profile can be

determined at every level above the inversion from our equations, but that feature is not implemented. Figure 2.2 shows the temperature and relative humidity profiles for the base case in the convective and subsidence regions.

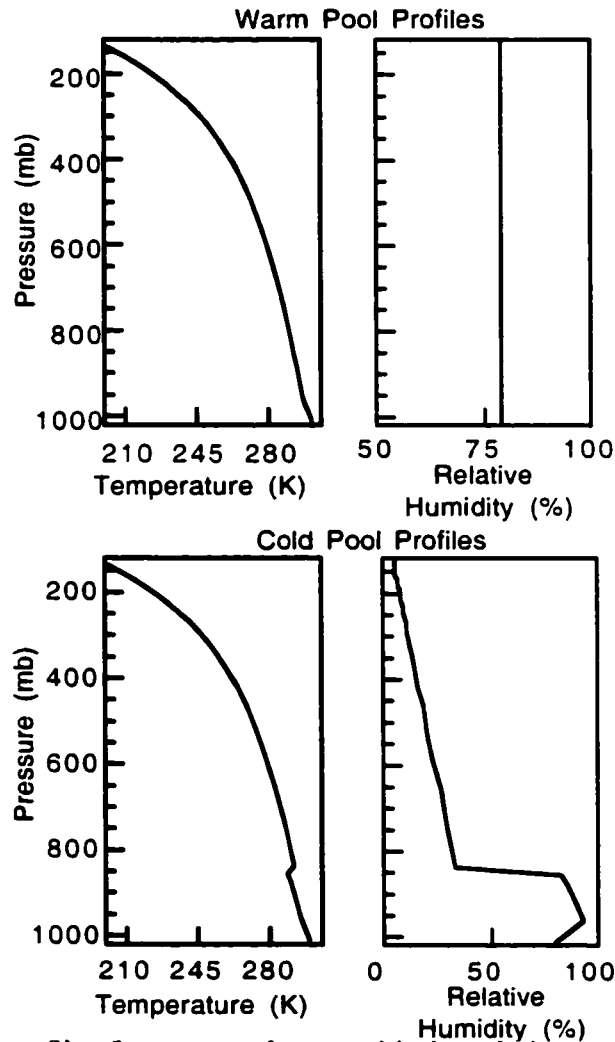


Figure 2.2 Vertical profiles from control case with the relative area of the warm pool equal to 0.3333 a) Temperature and relative humidity vertical profiles in the warm pool. b) Temperature and relative humidity vertical profiles in the cold pool.

To simulate the impact of clouds on this tropical equilibrium climate the radiative properties of the anvils in the deep convective box and the boundary layer clouds in the subsidence region are specified. High clouds with an optical depth of 6.5 cover 60% of the convective region in the base equilibrium climate. The properties are chosen to

give approximately zero net cloud forcing at the top of the atmosphere (TOA), as observed (e.g. Harrison et al. 1990, Hartmann et al. 1993). In the cold pool boundary layer (CPBL) a surface mixed layer is topped by a cloud layer with a fixed 30% cloud fraction and a fixed optical cloud depth of 5.0, giving a net cloud forcing at the TOA of -21 W m^{-2} . The top of the clouds is just below the trade inversion. These cloud properties and cloud radiative effects are in general agreement with International Satellite Cloud Climatology Project (ISCCP) and Earth Radiation Budget Experiment (ERBE) observations (Ockert-Bell and Hartmann 1992).

The amount of cloud cover in the subsidence region can be predicted by a diagnostic relationship. Klein and Hartmann (1993) developed a relationship between the low cloud cover and the lower tropospheric stability (LTS) in stratus regions. LTS is defined as the potential temperature at 700 mb minus the potential temperature at the surface. The relationship, $c' = 5.70LTS'$, is used in this model. c is the cold pool boundary layer cloud cover in percent and the primes refer to anomalies from the average (base case) value. Miller (1997) also used this relationship to predict low cloud amount in a two box model. Miller found that this relationship leads to a negative feedback associated with the low clouds.

The model uses two boxes in the tropics as in Pierrehumbert (1995), though it includes more realistic radiation fluxes and a boundary layer in the cold pool. The boundary layer uses a mixing line model based on Betts and Ridgway (1988, 1989, hereafter BR89). Unlike the two box model in Miller (1997), this model predicts the height of the boundary layer and the amount of water vapor above the cold pool inversion. The two box model of Clement and Seager (1999) differs from this model because it has a fixed ratio of warm pool to cold pool area and interactive ocean heat transports.

Requiring energy and moisture balances in the atmosphere and the ocean determines solutions for the dependent variables of the model: the sea surface temperatures

in the cold and warm pools, the strength of the circulation, the temperatures and humidities in the atmosphere, and the height of the trade inversion. This equilibrium climate is a function of the independent variables in the model which include the relative size of the warm and cold pools, the surface wind speed, the cloud fractions, and others. The sensitivity of the model climate to these parameters is tested. Specific model details are given in the following sections.

2.2.2 Cold Pool Boundary Layer (CPBL) Equations

This section describes the heat and moisture balances used below the trade inversion in the subsidence region. In the mixing line model, a mixed layer extends from the surface to the lifting condensation level of surface air, and above that a cloud layer extends to the trade inversion. The air properties in the cloud layer are determined by conservative mixing of air from above the inversion with surface air (BR89).

The moisture balance states that the drying of the CPBL due to the entrance of dry subsiding air into the CPBL is balanced by evaporation at the ocean surface. The energy balance of the CPBL, where no precipitation is assumed to occur, requires that the radiative cooling of the CPBL is balanced by the warming due to subsidence of air through the trade inversion plus the small surface sensible heat flux. For the CPBL, the moist and dry static energy balances are:

$$Lm_c(\bar{q} - q_{invp}) = F_{evap}^c, \quad (2.1)$$

$$c_p m_c (\theta_{invp} - \bar{\theta}) + F_s^c = \Delta R_{inv}. \quad (2.2)$$

θ is the dry potential temperature and q represents the specific humidity. The variables representing properties of air above the inversion have the subscript *invp* (inversion plus). c_p is the specific heat of air and L is the latent heat of vaporization of water. m_c

refers to the strength of the subsidence at the top of the inversion, and by continuity it equals the mass flow from the cold pool to the warm pool below the inversion, assuming no net exchange of mass from the extratropics. The overbar symbol indicates the pressure weighted mean in the CPBL; for example,

$$\bar{q} = \frac{1}{(p_{sfc} - p_{inv})} \int_{p_{inv}}^{p_{sfc}} q dp. \quad (2.3)$$

In (2.2), ΔR_{inv} refers to the net radiative flux divergence in W m^{-2} between the surface and the inversion with positive values indicating radiative cooling. F_{evap}^c is the evaporation (latent heat flux) at the surface and F_s^c is the surface sensible heat flux. These quantities are defined using the bulk aerodynamic formulas:

$$F_{evap}^c = L m_o (q_{sat} - q_{sfc}), \quad (2.4)$$

$$F_s^c = c_p m_o (\theta_{SST} - \theta_{sfc}), \quad (2.5)$$

$$m_o = \rho C_d V_{surf}. \quad (2.6)$$

q_{sat} is the saturation vapor pressure at the sea surface and θ_{SST} is the potential temperature at the sea surface. m_o refers to the mass flux at the surface, it is proportional to the surface wind speed, V_{surf} and density, ρ , with $C_d = 0.0013$. At the surface the variables are specified by subscripts *sfc*.

To determine the vertical profile of specific humidity and temperature in the boundary layer, two mixing line model parameters are needed. β (dp^*/dp) is the change in lifting condensation level (p^*) with pressure and it is set to 1.2 for the

marine stratocumulus clouds. α is the change in virtual potential temperature with height and is set to -2.832 K per 100mb (Betts, 1985).

In the subcloud layer, the radiative cooling, sensible heat flux at the surface, advection into the layer, and the buoyancy flux must balance. Here the advection term is neglected, since it is an order of magnitude smaller than the other terms. The buoyancy flux at the top of the well mixed subcloud layer is scaled to be proportional to the surface sensible heat flux. Thus the surface heat flux is directly coupled to the radiative cooling in the subcloud layer:

$$(1 + K)c_p m_o (\theta_{SST} - \theta_{sfc}) = \Delta R_{sc}. \quad (2.7)$$

The constant K is set to 0.25. ΔR_{sc} refers to the net radiative flux divergence in W m^{-2} between the surface and the lifting condensation layer with positive values indicating radiative cooling. This equation closes the system and the surface air temperature, humidity and inversion height can all be predicted in the CPBL.

These mixing line model equations equilibrate on the time scale of approximately one day. Some of the quantities that must be specified to solve the mixing line equations are: the moist adiabat that the temperature profile adheres to above the inversion, the subsidence strength, the SST, and the profile of upper tropospheric humidity. The sensitivity of the mixing line model to these parameters is important in interpreting the coupled model behavior. For example, increasing the SST increases the sensible and latent heat fluxes and increases the height of the trade inversion. Increasing the surface wind speed increases the height of the trade inversion, the specific humidity near the surface, and the latent heat flux. Using a warmer upper tropospheric moist adiabat lowers the inversion height. Increasing the specific humidity above the inversion affects equation (2.1); as q_{invp} increases, \bar{q} also increases by lowering cloud top, since specific humidity is higher near the surface. Also the latent heat flux decreases and the

humidity at the surface increases for this case. Increasing the subsidence rate lowers the inversion height and increases the sensible and latent heat fluxes.

2.2.3 Tropospheric Energy Balance Equations

The energy balance for the troposphere is used to constrain the values of the moist adiabat and subsidence strength. For the sum of the subsidence region and convection region troposphere, the net radiative cooling of the atmosphere and export of heat to the extratropics balances the latent plus the sensible heat fluxes at the sea surface:

$$a_c F_{evap}^c + a_w F_{evap}^w + a_c F_s^c + a_w F_s^w = a_c \Delta R_{trop}^c + a_w \Delta R_{trop}^w + F_{aex} \quad (2.8)$$

The equation includes contributions from the fluxes in both the warm (with a superscript w) and cold (superscript c) pool boxes. ΔR_{trop} is the net radiative flux divergence in the atmosphere between the tropopause and the sea surface. a_c is the fractional area of the cold pool box and a_w is the fractional area of the warm pool box ($a_c + a_w = 1$). F_{aex} is the atmospheric export to midlatitudes (-19.5 W m^{-2}). As in BR89, the tropopause is approximated by the level where the moist adiabat intersects the 195 K isotherm.

The atmospheric energy flux (*Flux*) between the two boxes is proportional to the strength of the circulation times the difference in equivalent potential temperature between the CPBL mean and the warm pool mean above the height of the cold pool inversion:

$$Flux = c_p \left(a_w \overline{m_w \theta_e^w} - a_c \overline{m_c \theta_e^c} \right), \quad (2.9)$$

$$\overline{m_w \theta_e^w} = \int_{p_{inv}}^{p_{trop}} \frac{\partial m_w}{\partial p} \theta_e^w dp \quad \overline{m_c \theta_e^c} = \int_{p_{sfc}}^{p_{inv}} \frac{\partial m_c}{\partial p} \theta_e^c dp. \quad (2.10)$$

The energy and moisture fluxes between the boxes can depend on the divergence profile ($\frac{\partial m}{\partial p}$). In the CPBL, the divergence is assumed to be independent of pressure. In the base case, the divergence above the inversion also is assumed to be independent of pressure. Other divergence profiles for the warm pool are explored in the moisture budget section below.

The tropospheric energy balance equation in the subsidence region is:

$$F_{evap}^c + F_s^c + \frac{Flux}{a_c} = \Delta R_{trop}^c + \frac{F_{aex}}{a_c}. \quad (2.11)$$

F_{evap}^c is the surface latent heat flux and F_s^c the sensible heat flux in the subsidence region. ΔR_{trop}^c is the net radiative flux divergence in the cold pool troposphere.

The warm pool heat balance is similar to (2.8)

$$F_{evap}^w + F_s^w - \frac{Flux}{a_w} = \Delta R_{trop}^w. \quad (2.12)$$

2.2.4 Ocean Energy Balance Equations

The oceanic energy balance is straightforward:

$$a_c F_{evap}^c + a_w F_{evap}^w + a_c F_s^c + a_w F_s^w = a_c R_{sfc}^c + a_w R_{sfc}^w - F_{oh}. \quad (2.13)$$

where R_{sfc} refers to the net downward radiation at the surface, and F_{oh} is the energy

export from the tropical ocean into the mid latitude ocean. The energy balance for the entire system can be obtained by combining (2.11), (2.12) and (2.13),

$$a_c R_{TOA}^c + a_w R_{TOA}^w = F_{aex} + F_{oh}. \quad (2.14)$$

R_{TOA} represents the net shortwave plus longwave radiation entering the top of the atmosphere. By incorporating the atmospheric flux term, the SSTs in the convective and subsidence regions are constrained separately:

$$R_{TOA}^c + \frac{Flux}{a_c} = \frac{F_{aex}}{a_c} + F_{oh}^c, \quad (2.15)$$

$$R_{TOA}^w + \frac{Flux}{a_w} = F_{oh}^w. \quad (2.16)$$

The oceanic export to midlatitudes is split up to the warm pool and cold pool components, with superscripts w and c respectively, and they are related by:

$$a_c F_{oh}^c + a_w F_{oh}^w = F_{oh}. \quad (2.17)$$

2.2.5 Moisture Budget Equations

This moisture budget differs from those found in previous two box models (Pierrehumbert 1996, Miller 1997). Specifically, here the water vapor in the upper troposphere of the cold pool is predicted. The moisture budget is formulated for five regions: the sea surface, above the inversion in the cold pool, the cold pool boundary layer (CPBL), the warm pool above the level of the cold pool inversion, and the warm

pool below that level. The moisture balance in the CPBL was already described in section 2c.

At the sea surface total evaporation is equal to the precipitation in the warm pool:

$$a_c E^c + a_w E^w = a_w P. \quad (2.18)$$

The precipitation rate in the warm pool is 14 mm day^{-1} for the base case. This corresponds to an average precipitation rate of about 1.7 m year^{-1} over the model domain.

In the warm pool below the level of the cold pool inversion, moisture is imported from the cold pool ($F_q^{BL} = L\bar{q}a_c m_c$) and through evaporation from the sea surface, and moisture is exported by ascent across the inversion (F_{inv}^w), so that in equilibrium,

$$F_q^{BL} + a_w E^w - F_{inv}^w = 0. \quad (2.19)$$

The moisture imported from the CPBL is the same amount exported from the CPBL, as seen in equation (2.1).

Above the level of the cold pool inversion in the warm pool, the precipitation plus the amount of moisture exported to the cold pool (F_q^{trp}), equals the moisture flux ascending in the warm pool at the level of the cold pool inversion (F_{inv}^w),

$$F_{inv}^w - F_q^{trp} - a_w P = 0. \quad (2.20)$$

The upward flux of moisture in the warm pool is assumed to be proportional to the large-scale mass flux:

$$F_{inv}^w = a_w m_w Lq_{inv}^w (1 + \gamma). \quad (2.21)$$

q_{inv}^w is the specific humidity in the warm pool at the level of the cold pool trade inversion. The parameter γ represents the fraction by which eddy fluxes augment the large-scale flux. A reasonable climate is obtained if the value of γ is set to 0.44. The relative humidity in the warm pool is determined from (2.21). The constant γ is a key closure parameter for the moisture budget and is a great simplification over more detailed physical models that parameterize detrainment, between-cloud subsidence, and precipitation efficiency within the warm pool.

In the atmosphere above the inversion in the cold pool, all the moisture is assumed to come from the warm pool and descend across the inversion. Salathe and Hartmann (1998) have shown with observations that the upper tropospheric water vapor is well predicted by the large-scale advection of water vapor from convective regions. Liquid water and ice advection do not appear to be important. Moisture exchange with the extratropics is neglected. So the vapor leaving the warm pool (F_q^{trp}) must equal the vapor crossing the inversion in the cold pool (F_{inv}^c):

$$F_{inv}^c = F_q^{trp}, \quad (2.22)$$

$$a_c m_c L q_{invp} = a_w L \int_{p_{inv}}^{p_{trp}} \frac{\partial m_w(p)}{\partial p} q_w(p) dp. \quad (2.23)$$

q_{invp} is the specific humidity immediately above the cold pool inversion. m_c is the subsidence in the cold pool at the level of the trade inversion, m_w is the rising motion in the warm pool. q_w is the amount of water vapor in the warm pool for each pressure level. The mass of air subsiding at the inversion of the cold pool is equal to the air rising in the warm pool at the same level:

$$a_w m_w = a_c m_c \quad (2.24)$$

Assuming constant divergence of warm pool air between the trade inversion and the tropopause, (23) becomes:

$$q_{invp} = \overline{q_w} = \frac{1}{p_{inv} - p_{trp}} \int_{p_{inv}}^{p_{trp}} q_w(p) dp . \quad (2.25)$$

For constant divergence, the amount of moisture immediately above the trade inversion is equal to the pressure weighted mean moisture in the warm pool above the inversion. Note that the moisture in the cold pool does not depend directly on the strength of the circulation or the ratio of the areas of the cold pool to warm pool. It is the humidity of the warm pool that is important. Equation (2.23) can be solved for any pressure below the tropopause and above the inversion in the cold pool, giving the humidity profile above the trade inversion in the cold pool. For simplicity, the equation is solved only at the inversion and the relative humidity profile of Manabe and Wetherald (1967) is used above that level. This moisture budget is in contrast to Sun and Lindzen (1993) who proposed that hydrometeors from the convective region are the strongest contributors to the upper tropospheric humidity in subsidence regions.

Reasonable humidities in the cold pool troposphere are obtained by assuming a large-scale divergence profile that is independent of pressure. With our assumption of constant divergence from inversion to tropopause, a humidity of 5.3 g kg^{-1} above an inversion at 850 mb is obtained in the cold pool, which compares well with data in Betts and Albrecht (1987). The observed divergence profile, on the other hand, is strongly peaked in the upper troposphere (Mapes and Houze, 1995). The divergence profile is approximated by a maximum at the tropopause and a linear decrease to zero at 400 mb, a specific humidity of 0.2 g kg^{-1} is obtained above an inversion at 750 mb (Table 2.1). In this case the cold pool is unrealistically dry and the inversion is high. Other profiles of divergence are included in Table 2.1.

Table 2.1 External parameter values for two box model base case

Parameter	Value in base case
Cold pool surface wind speed	6.7 m s ⁻¹
Warm pool surface wind speed	4.2 m s ⁻¹
Atmospheric export to extratropics	-19.5 W m ⁻²
Ocean export to extratropics	-42.5 W m ⁻²
Relative area of warm pool	0.3333
Relative area of cold pool	0.6667
High cloud cover in warm pool	60%
BL cloud cover in cold pool	30%

In reality, the exchange of moisture between the warm pool and the cold pool is not determined by the mean divergent circulation alone. Mixing by transient and non divergent motion is also important (Yang and Pierrehumbert, 1994). The successful simulation given by the constant divergence profile assumes that water vapor is mixed into the subsiding regions from all levels of the convective region. A constant divergence is equivalent to letting all levels contribute water vapor in proportion to their mass, and this is in many ways the simplest assumption. Our constant divergence profile is a simple way of producing realistic values of cold pool humidity.

2.2.6 Solution Procedure

Model solutions are obtained by an iteration procedure. Initially a solution to the model is guessed, then the terms of the equations are computed and checked. The equations are checked in a specific order and the first variables are changed until the first equation balances, before the next equation is evaluated. Every time a variable is changed, the model solution is checked again from the beginning. The surface specific humidity and surface air temperature in the cold pool and the trade inversion height are adjusted until equations (2.1), (2.2), and (2.7) are satisfied. Equations (2.21) and (2.23)

constrain the humidities in both pools. The ocean energy balance in the warm pool and equations (2.8), (2.11), and (2.14) are iterated towards equilibrium by adjusting the SST in the warm and cold pools, the strength of the subsidence, and the value of the moist adiabat. Convergence is assumed when the energy and moisture balances are all within one percent of the largest energy term in the equation. The uncertainty in the SST with this constraint is 0.5 K. The radiation code STREAMER (Key, 1996 and references therein) is used to determine the radiative fluxes. The two stream radiative approximation is used and the radiative effects of principle gases, carbon dioxide, ozone, water vapor, and the specified clouds are included.

2.3 Model Sensitivities

In this section the base model and its sensitivities to some of the parameters will be described and explored. The area ratio, surface wind speed, and cloud cover are changed in small increments and the subsequent changes in the model equilibrium are described. In addition the role of humidity above the boundary layer in the cold pool and the role of the moisture prediction equations is investigated as the area ratio is changed. The response of two box models to clouds and area ratios has been previously studied (Miller, 1997, Pierrehumbert, 1995). Here the response of the circulation strength, as given by the subsidence strength at the height of the variable trade inversion, is also noted.

2.3.1 Base Climate

For the base case, the parameters are chosen to approximate the Walker circulation in the Pacific (Table 2.2). This system is now relatively well observed, especially from the TOGA Tropical Ocean Atmosphere (TAO) buoy array. The base case parameters are evaluated by supposing the model covers the area in the Pacific observed by the TAO buoys, 135 °E to 95 °W and 10 °N to 10 °S. The warmest waters, high humidi-

Table 2.2 Base case solution state variables for the two box model

Variable	Value in base case
SST warm pool	302.9 K
SAT warm pool	300.8 K
SST cold pool	300.0 K
SAT cold pool	299.0 K
inversion pressure	850 mb
specific humidity above inversion	5.3 g kg ⁻¹
relative humidity in warm pool	78%
subsidence at inversion	52 mb day ⁻¹
value of moist adiabat	354 K
mean precipitation rate in tropics	4.6 mm day ⁻¹
latent heat flux in warm pool	124 W m ⁻²
latent heat flux in cold pool	133 W m ⁻²

ties and upper level cloudiness, cover the western third of the region, so the relative area of the warm pool in the base case is 0.33 and cold pool relative area is 0.67.

Values for the ocean and atmospheric exports across 10 °N and 10 °S are 42.5 W m⁻² and 19.5 W m⁻² respectively (Peixoto and Oort, 1993). The surface wind speed in the warm pool is set to 4.2 m s⁻¹ and in the cold pool to 6.7 m s⁻¹. The surface wind speeds are consistent with data from the Comprehensive Ocean-Atmosphere Data Set (COADS), where the wind speeds in the warm pool are less than in the cold pool. Higher cold pool surface winds speeds are also found by the TOGA TAO buoys from July 1991 to June 1993 (Zhang and McPhaden, 1995). Convective cloud cover is chosen to be 60% in the warm pool and boundary layer cloud cover is 30% in the cold pool, in agreement with ISCCP estimates.

The ocean heat transport divergence is taken from Hartmann (1994, Fig. 4.18). The cold pool region is influenced by larger oceanic cooling from the upwelling that occurs in the eastern Pacific ocean. The oceanic export was distributed between the warm and cold pools as consistent with Hartmann (1994); 5 W m^{-2} is exported from the warm pool ocean and 61.25 W m^{-2} is exported from the cold pool ocean. The tropical Western Pacific is surrounded by subsidence regions so atmospheric export to the extratropics is applied only to the cold pool region. The subsidence region exports $19.5/0.67 = -29.25 \text{ W m}^{-2}$ to the extratropics in the base case.

The model equilibrium values for the base case are given in Table 2.3. The

Table 2.3 Boundary layer results for changing divergence profiles

divergence profile	warm pool SST (K)	cold pool SST (K)	pressure at the inversion (mb)	specific humidity above inversion (g kg^{-1})	strength of subsidence at inversion (mb day^{-1})
constant	302.9	300	850	5.3	52.4
linearly decreasing from tropopause to 700 mb	298	292.4	875	0.83	55.8
linearly decreasing from tropopause to 400 mb	299.3	295.0	750	0.20	52.2
linearly decreasing from tropopause to 300 mb	300.1	296.1	690	0.07	49.7

observed annually averaged SST in the western Pacific is 303.1 K and in the east is 299.2 K (Reynolds and Smith 1995). The model temperatures are 302.9 K and 300 K, respectively. The inversion is usually found around 800 mb in the trade wind regime of the Pacific and it is at 850 mb in this model. The relative humidity in the warm pool is expected to be around 75% from the warm pool observations in Brown and Zhang (1997) and here it is 78%. A reasonable observed value of the specific humidity above

the inversion is 4 or 5 g kg⁻¹, and it is 5.3 g kg⁻¹ in this model. The subsidence rate at the inversion should be about 40 mb day⁻¹ (Betts and Ridgway, 1988) and it is 52 mb day⁻¹ here. The TOGA TAO buoys show latent heat flux in the warm pool of 93 W m⁻² and cold pool latent heat flux of 98 W m⁻² when averaged from July 1991 to June 1993 (Zhang and McPhaden, 1995). This model gives slightly higher latent heat fluxes of 124 W m⁻² in the warm pool and 133 W m⁻² in the cold pool. The mean tropical precipitation in the model is 4.6 mm day⁻¹ which is approximately the tropical average annual mean precipitation between 10 °N and 10 °S (Piexoto and Oort, 1992). Also BR89 give a value of 348.6 K for the tropical moist adiabat which is close to the 354 K in the base case equilibrium.

2.3.2 Area Ratio and Moisture Budget

How would the tropical SSTs evolve if the area of the deep-convective portion of the tropics increased? To investigate this a series of calculations were performed in which the area of the warm pool was varied (Figure 2.3). The cloud cover in each box

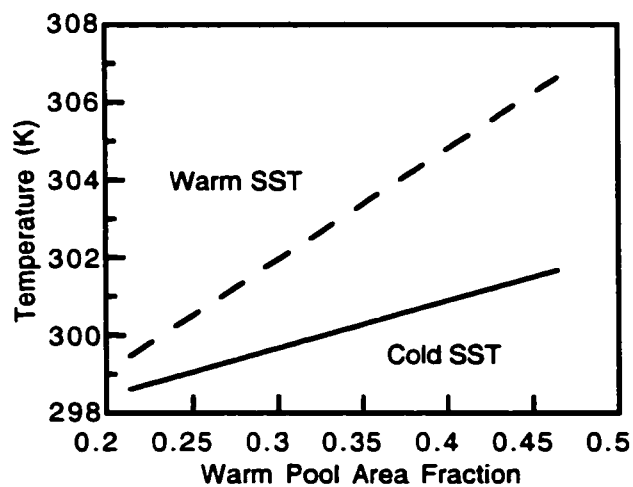


Figure 2.3 SST versus relative warm pool area. Warm pool SST is dashed and the cold pool SST is solid.

was adjusted to keep the total tropical amount of high and low clouds constant as the relative areas changed. Tropical cloud forcing at the TOA stays constant when the

tropical cloud amount is constant. As the convecting region increases in area, the SSTs in both regions increase. The temperatures increase because the low humidity of the upper troposphere in the subsidence region is replaced with the high humidity of the convecting region. As the humid convective region occupies a larger fraction of the tropics, warmer temperatures are needed to emit the same amount of energy to space. This same effect is described in Pierrehumbert (1995).

The area ratio was varied with two different moisture schemes. For the fixed humidity experiment the relative humidity in the warm pool and the specific humidity above the inversion of the cold pool were both held constant at their values for the base case. Equations (2.21) and (2.25) were not used for the fixed humidity experiment. In the moisture budget experiment the warm pool relative humidity increases from 72% to 86% and the specific humidity above the cold pool inversion changes by 4 g kg^{-1} which corresponds to an increase in the relative humidity above the inversion from 30% to 39% (Figure 2.4).

The cold pool subsidence rate decreases with its relative area using both fixed and predicted moisture (Figure 2.4). The subsidence in the cold pool is equal to the radiative cooling of the atmosphere divided by the dry static stability for that region. The dry static stability is related to the lapse rate of the moist adiabat. Because the moist adiabatic lapse rate strongly decreases with increasing temperature, the dry static stability of the troposphere rises dramatically in a warmer climate. The dry static stability increase dominates the change in radiative cooling, leading to a decrease in the strength of the subsidence. Knutson and Manabe (1995) also found a decrease in the tropical circulation and an increase in static stability when the climate in their coupled GCM was warmed by doubling CO_2 . Both the subsidence and the cold pool area decrease as the relative area of the warm pool increases, so the large-scale mass flux decreases with increasing warm pool area. In a fully coupled model in which the convective area is predicted, these effects may lead to a negative feedback that constrains

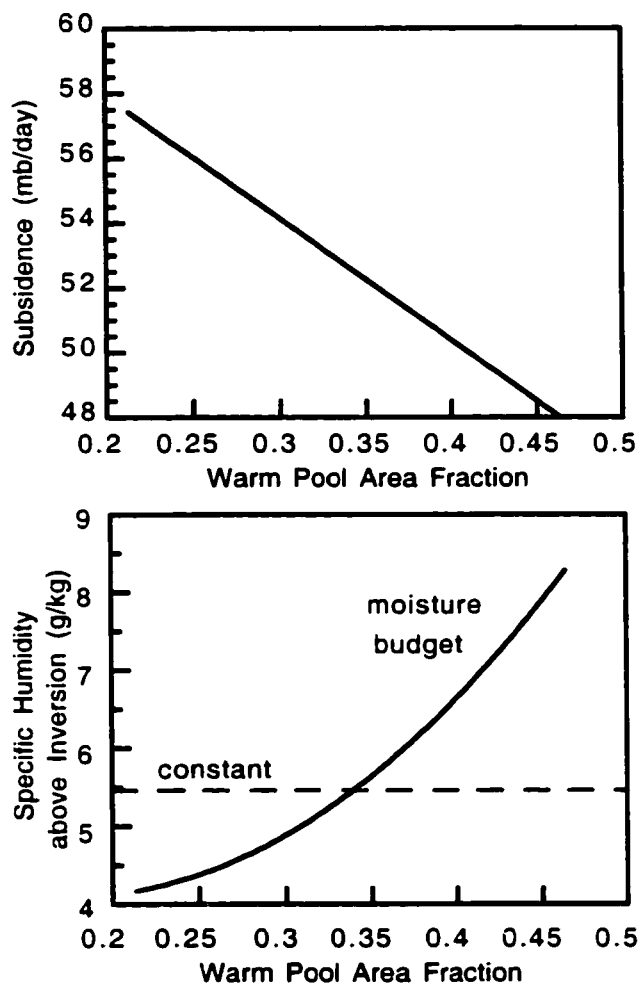


Figure 2.4 Variable sensitivities as the relative area of the warm pool increases a) Subsidence, strength of the circulation b) Specific humidity above the trade inversion in the cold pool. Solid line is for predicted moisture and dashed line is for fixed humidity. the size of the convective area. In this experiment the SST difference increases as the circulation and associated large-scale heat flux decrease. This is logical from a thermodynamic perspective, but a different result might be obtained in a model with a momentum budget. The increasing difference between the cold pool and warm pool SSTs is also found in Pierrehumbert (1995).

The large-scale energy flux between the boxes is proportional to the strength of the circulation times the difference in mean equivalent potential temperature between the CPBL and the warm pool troposphere. The strength of the circulation decreases as the

warm pool area is made bigger, and the difference in mean equivalent potential temperature increases somewhat to maintain the energy exchange rate (Figure 2.4). The mean equivalent temperature in the CPBL increases more than the SST indicates because the height of the inversion decreases 60 mb, and equivalent potential temperature decreases with height in the mixing line boundary layer in the moisture budget case. The warm pool tropospheric equivalent potential temperature rises because the relative humidity in the warm pool increases 15%. These factors increase the energy transport per unit of large-scale mass flux, and the amount of large-scale mass flux decreases strongly with the increase in warm pool relative area. In the constant moisture case, the inversion height remains constant and the SST difference between the two pools is more sensitive to changes in area ratio than in the moisture budget case. Since the CPBL height is less sensitive with fixed humidity and the warm pool relative humidity is fixed, the SST difference increases to create the same mean equivalent potential temperature difference as in the moisture budget case.

Using a moisture budget causes a positive feedback, when compared with a fixed humidity experiment (Figure 2.5). In the moisture budget experiment the increase in

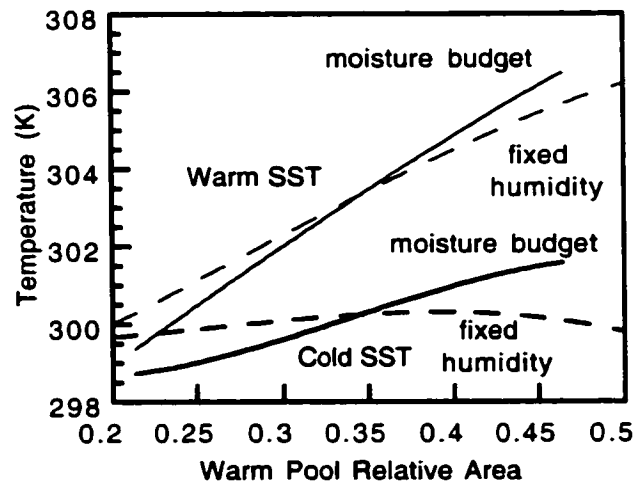


Figure 2.5 Comparison of equilibrium solutions for experiments using the moisture budget (solid) and for experiments when the humidity is specified as a constant (dashed). The warm pool SST (thin) and cold pool SST (thick) are shown.

temperature of the moist adiabat leads to an increase in the cold pool specific humidity above the inversion. The moist adiabat requires that a small warming at the surface is magnified in the upper troposphere. The warmer temperatures in the warm pool upper troposphere require more specific humidity to maintain similar warm pool relative humidities. The humidity above the inversion in the cold pool is a slave to the warm pool specific humidity, so the cold pool humidity increases with temperature.

2.3.3 Moisture Budget: Cold Pool Humidity

The sensitivity of the model to the specific humidity above the inversion is very interesting. The moisture budget is suppressed in the following experiment by keeping the relative humidity in the warm pool constant. Equations (2.21) and (2.25) are disabled and the specific humidity above the inversion is fixed at values varying from 2 g kg^{-1} to 8 g kg^{-1} . Surprisingly, the SSTs in the model stay nearly constant as the moisture is varied (Figure 2.6). In a sequence of equilibrium calculations, the OLR above

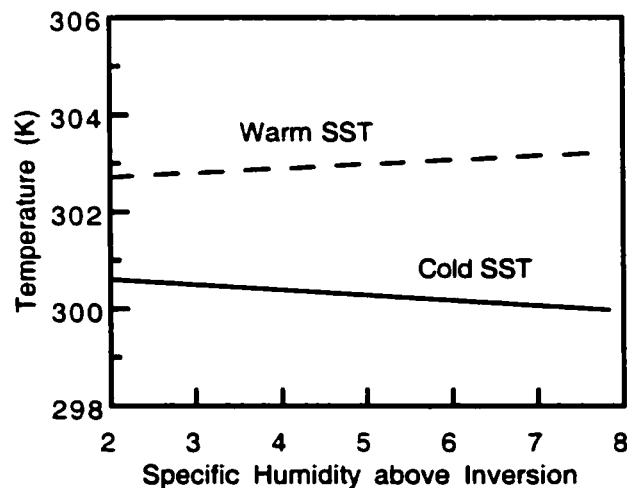


Figure 2.6 SST in the warm and cold pools versus specific humidity above the inversion. Warm pool SST is dashed and the cold pool SST is solid.

the cold pool is surprisingly insensitive to the humidity above the inversion. The reason for this is the response of the mixing line model to the increased humidity. As the humidity above the inversion increases, the CPBL thins significantly (Figure 2.7). The

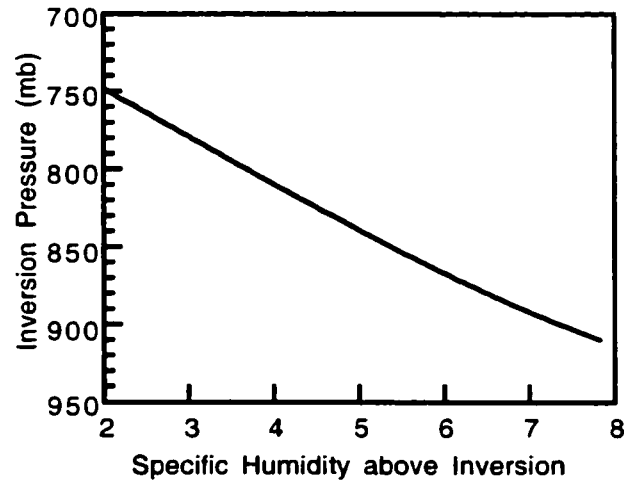


Figure 2.7 Height of the inversion versus the specific humidity above the inversion. expected decrease in OLR due to enhanced upper tropospheric water vapor is almost cancelled by two factors. The factors are the decrease in the amount of boundary layer water vapor and the increase of the average temperature of the water vapor content of the boundary layer. The greenhouse effect of water vapor in the tropics is largely contributed by lower tropospheric water vapor (Shine and Sinha, 1991). If this compensation between humidity above the inversion and thickness of the boundary layer actually operates in nature, it could constitute an important negative feedback for the climate system, and it might make upper tropospheric humidity in subsidence regions of the tropics a less critical issue.

The compensation arises from the energy and moisture budget equations for the boundary layer. If the humidity above the inversion is increased, it causes the radiative cooling of the boundary layer to decrease. From equation (2.2), a new equilibrium can be achieved for fixed mass flux by decreasing the difference between potential temperature above the inversion and the mean potential temperature in the mixed layer. The difference is decreased by lowering the trade inversion. From equation (2.1), if the humidity above the inversion is increased, the moisture balance can be restored by increasing the mean humidity of the boundary layer. This is also achieved by moving the CPBL top down.

There are limitations of this model that may change this interesting behavior. In addition to the approximate nature of the mixing line model, constant boundary layer cloud properties are assumed in these tests. The boundary layer cloud properties may change in a way that alters the negative feedback mechanism described here. Precipitation in the boundary layer could also affect the equations in such a way as to reduce changes in inversion height. To see how precipitation in the CPBL could alter the sensitivity of inversion height to humidity above the inversion, rewrite (2.1) and (2.2) with a precipitation term included:

$$Lm_c(\bar{q} - q_{invp}) = F_{evap}^c - LP, \quad (2.26)$$

$$c_p m_c (\theta_{invp} - \bar{\theta}) + F_s^c = \Delta R_{inv} - LP. \quad (2.27)$$

Now begin as before with the fact that increases humidity above the inversion will decrease the radiative cooling of the boundary layer, and consider the implication of this for the energy budget in (2.27). Now the system can respond by either thinning the boundary layer to decrease the entrainment heating or by decreasing the precipitation rate, or both. Similarly, in the humidity equation (2.26), when the entrainment drying decreases with increased humidity above the inversion, the system can also achieve balance by decreasing the precipitation rate, lowering the inversion, or both. If precipitation in the boundary layer below the subsidence region is an important term in the heat and moisture budgets, then the sensitivity of the inversion height to moisture above the inversion might be less than in our model. The extent of the compensation provided by precipitation variations would need to be investigated with a model that captures the physics of precipitation in the boundary layer. The inclusion of precipitation has been explored by R. Seager and A. Clement (personal communication).

2.3.4 Warm pool cloud sensitivity

The cloud cover in the convective region of the model is approximated by a high ice cloud of optical depth 6.5 covering 60% of the box with the cloud top at the tropopause. The amount of deep convection could change in a future climate regime and it has been hypothesized that the radiative effect of clouds in convective regions could constitute a strong negative feedback on tropical SST (Ramanathan and Collins, 1991). In this set of experiments the fractional area of clouds in the warm pool is changed from 25% to 100%, while keeping the other cloud properties fixed. Only the radiative effect of the clouds is considered. The warm pool SST shows a 1.7 K decrease in response to increasing the area coverage of convective clouds by 50% (Figure 2.8).

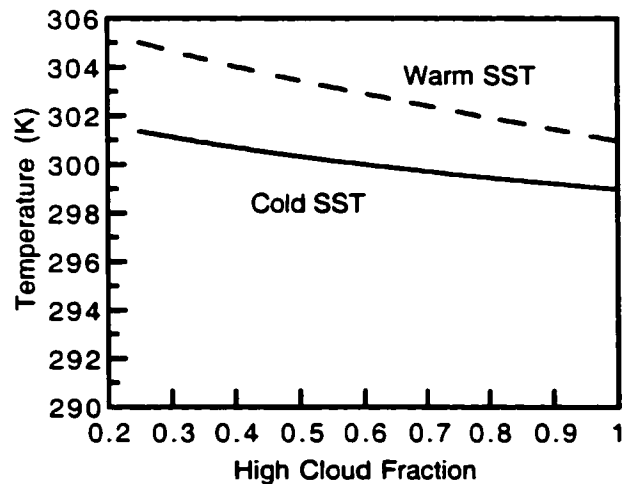


Figure 2.8 SST versus warm pool cloud fraction. Warm pool SST is dashed and the cold pool SST is solid.

The model shows little response to the radiative forcing of convective clouds because they do not significantly perturb the radiation balance at the top of the atmosphere (TOA), where the shortwave and longwave effects (-94 W m^{-2} and $+92 \text{ W m}^{-2}$ respectively, for the for the base case of 60% high cloud fraction) nearly cancel each other. This insensitivity is also found in the two box models of Pierrehumbert (1995) and Miller (1997). The radiation balance at the surface of the warm pool is affected by

the convective cloud amount because the convective clouds reduce insolation at the surface. The surface forcing affects the evaporation and sensible heat fluxes in the warm pool. As the convective cloud amount increases, the radiative heating of the surface decreases. Decreased radiative heating of the surface can be balanced by decreased evaporation, from the warm pool part of equation (2.13). In the troposphere (2.11) decreased total latent heat release is balanced by decreased longwave cooling of the atmosphere that is also produced by the convective clouds. When the cloud cover in the warm pool is increased from 25% to 90% the relative humidity in the warm pool decreases from 84% to 73%, the SST decreases by 3.7 K in the warm pool, and the difference between SST and SAT decreases from 4.2 K to 0 K. The temperature changes offset the humidity changes and produce a 50 W m^{-2} decrease of latent heat flux. Thus the radiative effects of the high clouds within the system are almost completely cancelled by changes in the hydrologic balances, and these changes are accompanied by little change in SST. Because the radiative effects reduce evaporation and precipitation, the radiative changes seem to more strongly limit convection itself than SST. In this solution, the high cloud fraction increases as the total precipitation decreases. These trends are physically inconsistent and point to the need to determine the high cloud fraction with model variables. In a fully coupled model, the radiative effects of clouds reduce the generation of convective instability and help establish a stable balance point in which convective clouds are limited in extent.

2.3.5 Cold pool boundary layer cloud sensitivity

The SST is much more sensitive to the amount of boundary layer cloud in the cold pool than to the amount of convective cloud in the warm pool, because the boundary layer clouds have a strong effect on the TOA energy balance. When the cold pool cloud fraction is varied from 20% to 90%, the cold pool SST decreases 12 K, the warm pool SST decreases 11 K, and the specific humidity at the top of the inversion decreases from 6.4 to 2.0 g kg^{-1} (Figure 2.9). Contrasting figures 2.8 and 2.9 shows the

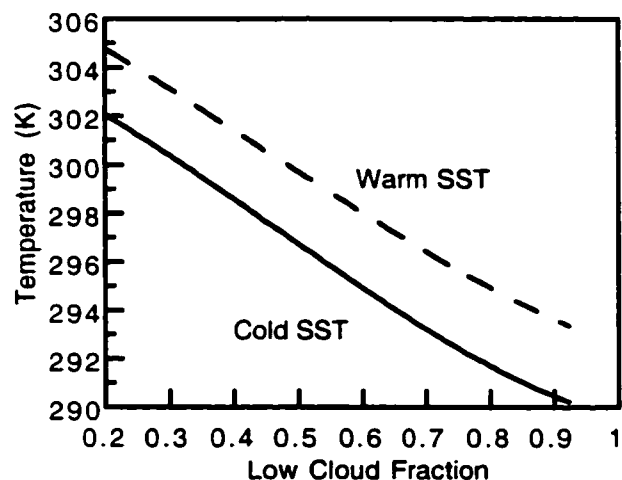


Figure 2.9 SST versus varying cold pool cloud fraction. Warm pool SST is dashed and the cold pool SST is solid.

insignificance of high warm pool clouds when compared to CPBL clouds. The increased CPBL cloud cover provides a strong cooling effect to the cold pool and this is quickly transmitted to the warm pool by the large-scale circulation. The cooling effect of low clouds was explored previously in a general circulation model (Philander et al., 1996) and a two box model (Miller, 1997).

The decreasing temperatures also imply a decreasing static stability in the cold pool free troposphere which is stronger than the decrease in radiative cooling above the cold pool inversion and produces an increase in the model circulation. The subsidence rate increases from 49 to 83 mb day^{-1} with increasing low cloud fraction because of the decreasing stability as the temperature of the moist adiabat decreases. The warm pool area and BL cloud sensitivities both show that the static stability change is more important than the change in radiative cooling above the cold pool inversion.

2.3.6 CPBL Predicted Cloud Fraction

When the CPBL cloud fraction is predicted from the lower tropospheric stability (LTS) the model sensitivity is less than when the tropical average cloud fraction is kept constant (Figure 2.10). Because the product of the area of the cloud cover and the rela-

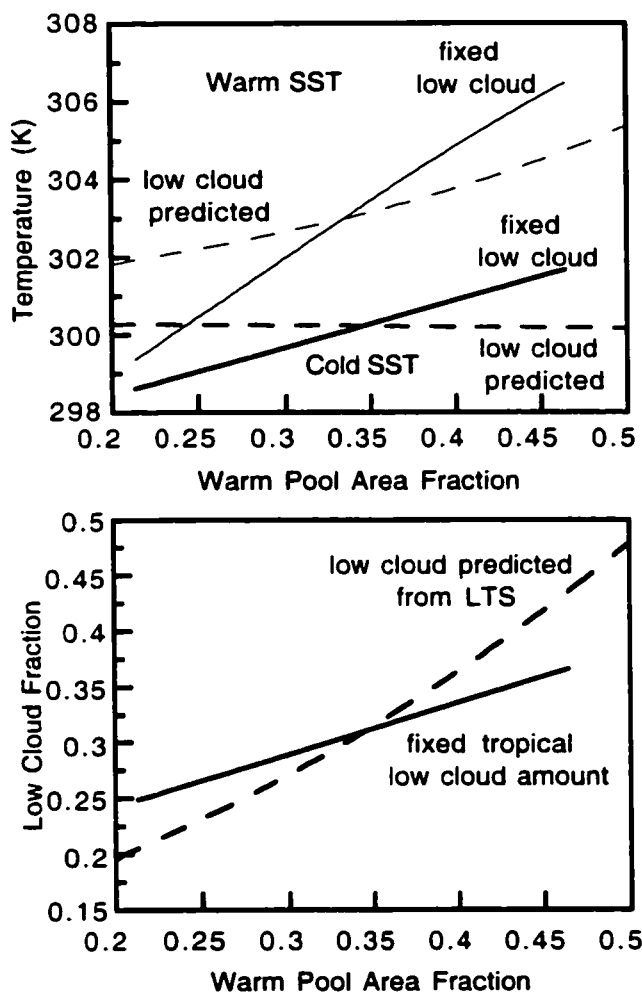


Figure 2.10 Low cloud fraction and SST versus warm pool area fraction. a) SST as a function of warm pool area for the warm pool (thin lines) and cold pool (heavy lines) for the cases in which tropical average low clouds in the cold pool are fixed (solid) and when the low clouds are predicted from lower tropospheric stability (dashed). The tropical average low cloud amount is the area coverage of the low clouds in the cold pool times the relative area of the cold pool. b) Warm pool area fraction versus CPBL cloud fraction while the BL cloud fraction is predicted using the LTS (dashed) and while the tropical average low cloud amount is held constant at 20% (solid).

tive area of each region are set to a constant means that the tropical average TOA cloud forcing is constant. LTS in the cold pool increases as the climate is warmed, because the temperature is assumed to follow a moist adiabat above the inversion. In the case where the climate is warmed by increasing the convective area, the SST difference between the two pools also increases slightly with temperature, and this also contrib-

utes to the LTS increase in the cold pool (Figure 2.10a). Since the low cloud fraction is assumed to be proportional to LTS and the low clouds produce a cooling, the low cloud feedback will be strongly negative. When the cloud fraction is predicted from LTS, the temperatures are not as sensitive to the relative areas of the boxes (Figure 2.10a). The cold pool SST increases for the constant tropical cloud fraction case, but decreases slightly for the predicted BL cloud fraction case. This negative feedback, also described in Miller (1997), could stabilize the tropical SSTs.

2.3.7 Surface wind speed

In this model, the surface wind speed only affects the efficiency of the latent and sensible heat fluxes at the ocean surface. The surface wind speed is not coupled to the circulation in the model. In a set of experiments to test the sensitivity to wind speed, the surface wind speed is increased the same amount in both regions (the cold pool wind speed is shown in the figures and the warm pool wind speed is always 2.5 m s^{-1} less). The SSTs decrease as surface wind is increased, with the warm pool SST decreasing by a larger amount (Figure 2.11). In the warm pool, the increased surface

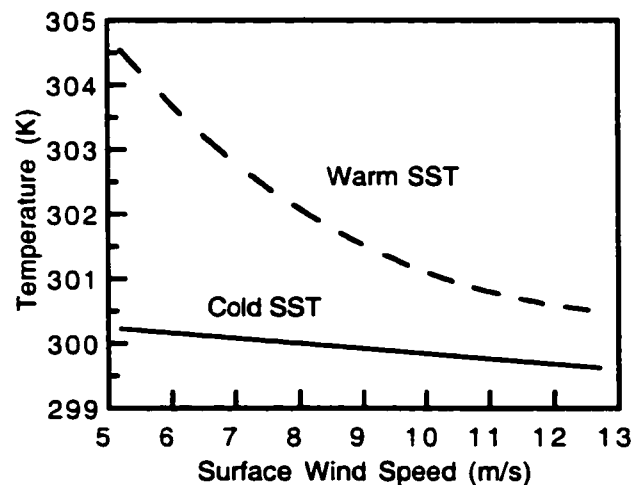


Figure 2.11 SST versus surface wind speed. Warm pool SST is dashed and the cold pool SST is solid.

flux efficiency decreases the SST and decreases the relative humidity. BR89 also found

that increasing the wind speed decreased the SST, though the depth of the BL was constant in BR89 and in this experiment the CPBL depth increases with wind speed (Figure 2.12b). The more efficient surface heat fluxes pump heat into the atmosphere. In

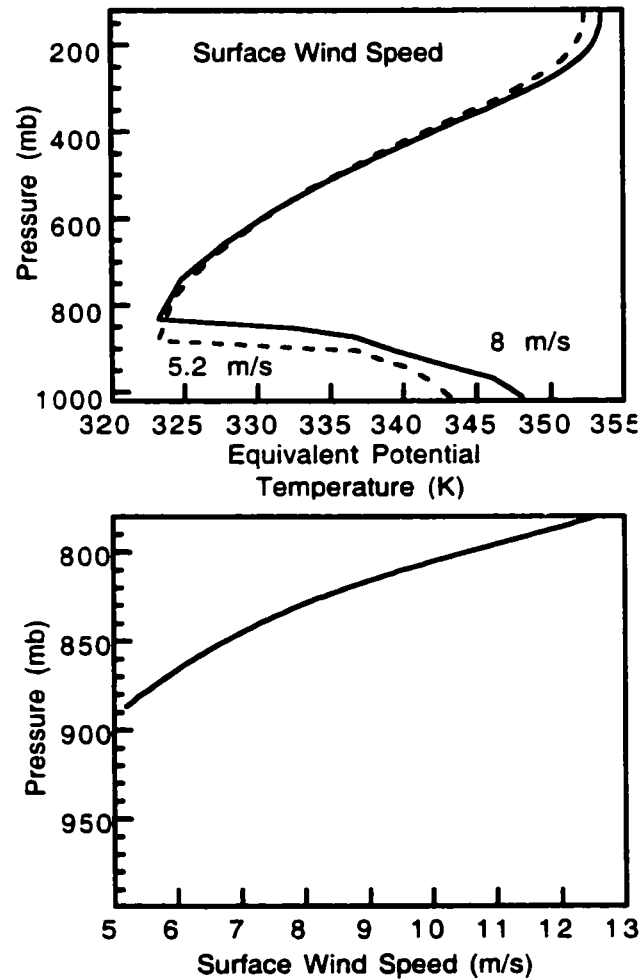


Figure 2.12 a) Profiles of equivalent potential temperature for different surface wind speeds: 5.2 m s^{-1} in cold pool (dashed) and 8 m s^{-1} surface wind speed in cold pool (solid) b) Height of the cloud layer versus surface wind speed.

the cold pool this energy flux can be balanced by decreasing the input of energy from the warm pool. The depth of the CPBL increases and the subsidence rate decreases, but the cold pool SST stays nearly constant as the wind speed is increased (Figure 2.12a). A weaker circulation and smaller difference between cold and warm pool SSTs

both decrease the energy flux to the cold pool from the warm pool. It is interesting to note that the large-scale energy flux makes it possible to increase the surface wind speed without decreasing the cold pool SST. This effect is not found in the one box model of BR89.

As the wind speed is increased, the subsidence and the difference between the warm pool and cold pool SSTs both decrease. In this model the surface wind is not coupled to the circulation strength or the SST gradient. The sensitivities of the circulation and SST gradient to the surface wind speed suggest that a stable balance point would exist if the surface wind speed were coupled to the circulation strength and SST gradient. In such a coupled model, increased SST gradients would lead to increased circulation which might lead to increased surface wind speed. According to the current model, the increased wind speed would act to decrease both the SST gradient and the circulation strength, leading to equilibrium. This behavior is similar to the mechanism described in Hartmann and Michelson (1993).

In one experiment the surface wind speed was made proportional to the strength of the circulation divided by the depth of the boundary layer. As the high cloud amount was changed, the SSTs and humidities in the model responded as if the wind speed was fixed. The circulation strength and inversion height did not vary as much with the predicted wind speed, and the predicted wind speed varied 0.5 m s^{-1} for the entire range of high cloud amounts. Predicting the surface wind speed, based on the divergent circulation, does not lead to significant changes in the sensitivity of the model to the high cloud amount, because the fractional change in the circulation strength is small.

2.4 Climate Sensitivities to Doubled Carbon Dioxide

To further investigate the sensitivity of the model, its response to doubled carbon dioxide (CO_2) is investigated. The effects of the moisture budget and the prediction of

the CPBL cloud fraction are investigated by comparing with experiments in which the humidity and the low cloud fraction are fixed. To investigate these sensitivities, three pairs of doubled CO₂ experiments were conducted, as shown in Table 2.4. The first is a

Table 2.4 Change in tropical mean SST with doubled carbon dioxide

Base Case tropical mean SST	301 K
Doubled CO ₂ and fixed humidity	+2.6 K
Doubled CO ₂ with predicted humidity	+2.5 K
Doubled CO ₂ with predicted humidity and low cloud feedback	+1.7 K

base case in which the relative humidity in the warm pool and the specific humidity in the cold pool and the low cloud fraction are fixed at base values. In this case the model warms by 2.6 K. If the moisture prediction scheme is turned on, the warming is 2.5 K. Including the moisture budget does not have a significant effect on SST. Including the moisture budget does not change the relative humidity in the warm pool, but the specific humidity above the inversion in the cold pool is increased 1 g kg⁻¹ (Table 2.5).

Table 2.5 Doubled carbon dioxide and moisture prediction

variable	base case	doubled CO ₂ moisture budget	doubled CO ₂ fixed humidity
tropical mean SST (K)	301	303.5	303.6
inversion height (mb)	854	846	808
specific humidity above inversion (g kg ⁻¹)	5.4	6.6	5.4
subsidence rate (mb day ⁻¹)	52.4	48.8	45.3
warm pool relative humidity (%)	79	79	79

From the moisture budget sensitivity experiment, an increase in specific humidity should thin the CPBL. The inversion is 37 mb lower in height in the doubled CO₂

moisture budget case than in the doubled CO₂ fixed humidity case. The inversion height is the same between the moisture budget cases with and without doubled CO₂, however, even though the specific humidity above the inversion is 1 g kg⁻¹ higher in the doubled CO₂ case. The reason the mixed layer depth does not respond to the humidity as expected is because the subsidence rate also changes. The subsidence rate has a strong influence on the height of the BL with less subsidence implying a thicker BL. The strength of the subsidence above the cold pool inversion decreases 7 mb day⁻¹ when CO₂ doubles and moisture is predicted. This decrease occurs because the warmer moist adiabat increases the static stability in the upper troposphere of the cold pool more than the radiative cooling increases.

If the low cloud prediction scheme is turned on, the warming in response to doubled CO₂ is only 1.7 K. The low cloud fraction increases 3% in the cold pool as the carbon dioxide doubles, and this is enough to reduce the warming 0.8 K when compared to the case without low cloud feedback. This result is similar to that found by Miller(1997). As a 3% uncertainty in the percentage of low clouds is possible in current measurements, and 3% is enough to cause a half degree negative feedback, the possibility of the low clouds affecting the climate of the tropics is significant. It is uncertain to what extent the empirical correlation applies to the entire tropics, since it was developed for stratus regions and a good fraction of the tropics is in the trade cumulus regime rather than the stratus regime. It is interesting, however, that the relative humidity below the inversion in the CPBL increases with static stability, which is consistent with more cloud (Albrecht 1981; Bretherton et al. 1995).

2.5 Summary and Conclusions

A simple two box energy and moisture equilibrium model of the tropics is used to investigate the physical mechanisms that control the climate of the tropics. One box represents the convective region of the tropics and the other box represents the subsiding regions in the tropics. A large-scale circulation connects the heat and moisture

budgets in the two boxes. The ratio of the areas of these two boxes must be specified, but the temperature and moisture are predicted. The temperature profile is assumed to follow a moist adiabat in the free atmosphere and the shape of the moisture profile is also prescribed, but the depth and properties of the boundary layer in the subsiding region are predicted with a mixing line model. Full radiative effects are included, but cloud optical properties are prescribed. A reasonable moisture prediction in the subsiding region is obtained if the convective region is assumed to detrain mass to the subsiding region in proportion to the vapor pressure at all levels.

If the fractional area of the convective region is increased, the climate warms, mostly as a result of the higher tropospheric humidity in the convective region.

The humidity in the subsiding region above the inversion increases rapidly with temperature because it is slave to the humidity in the convective region, but the positive feedback from this is weaker than expected because the depth of the CPBL decreases significantly as the humidity above the inversion is increased. Much of the water vapor greenhouse effect comes from the boundary layer humidity, so it is quite sensitive to the inversion height.

The mass flux between the two regions decreases with increasing temperature because changes in the radiative cooling rate in the subsiding region are overwhelmed by changes in dry static stability associated with the assumed moist adiabatic lapse rate. The SSTs in the convective and subsiding regions are held close together by the strong sensitivity of the large-scale energy flux to the difference between the moist static energy of the air in the convective region and the moist static energy in the boundary layer of the subsiding region.

The radiative effects of convective clouds and boundary layer clouds produce very different responses in the model. Convective clouds have a small net radiative effect at the top of the atmosphere, but cause a large redistribution of energy between the sur-

face and the atmosphere. Because convection rapidly exchanges energy between the surface and the atmosphere in the convective region, the importance of the convective cloud is dependent on its radiative forcing at the top of the atmosphere, which is small. So changing the area fraction of convective clouds has only a weak effect on equilibrium SST. The vertical redistribution of energy by convective clouds does have a significant influence on the hydrologic balances, since evaporation is reduced to compensate the reduction in solar heating of the ocean surface. This would have the effect of reducing the source of energy for convection. Thus, to first order, the radiative effects of convective clouds in the tropics is to reduce the intensity of tropical convection, not to reduce the SST.

On the other hand, boundary layer clouds in the subsiding region are very important for SST because they have a strong influence on the net radiation at the top of the atmosphere. Increasing their fractional coverage strongly cools the climate. The change in static stability, driven by the decreasing moist adiabat, increases the strength of the circulation as the BL cloud cover increases, even though the net radiative cooling above the inversion in the subsiding region decreases.

If the cloud properties are fixed, the sensitivity of the model is close to that of a 1-D model with fixed relative humidity. Doubled CO_2 increases the SSTs 2.6 K. If the boundary layer cloud in the subsiding region is predicted from an empirical relationship with lower tropospheric static stability, a strong negative feedback is produced which cuts the sensitivity to doubled CO_2 by a third.

While this simple model is efficient and illustrates some important connections in the tropical climate, it is highly simplified and could be made more realistic in many ways. The model points to a key role for the boundary layer, and a critical question seems to be the ability of the mixing line model to predict changes in the depth of the CPBL in the subsiding region. Although thermodynamic models of the trade inversion height (equation 2.2) do not include dynamic adjustments which horizontally flatten

the trade inversion height (Schubert et al. 1995), they may still be of relevance for predicting climate variations in the mean trade inversion height. In view of the strong role of clouds in the boundary layer of the subsiding region, a boundary layer model that incorporates cloud prediction and explicitly includes precipitation and cloud radiative effects seems to be needed. A more sophisticated parameterization of the effect of convection on the temperature and humidity profiles in the convective region would also be helpful, perhaps coupled with a prediction of the cloud physical properties. Relaxing the assumption of no horizontal temperature variation above the mixed layer and including momentum constraints would also be desirable. Striking an appropriate balance between a model that is easily comprehended and one that is physically realistic is the key issue in mechanistic models of this type.

The next two chapters focus on the Pennsylvania State University (PSU) / National Center for Atmospheric Research (NCAR) mesoscale model, MM5, which is more realistic in several of the ways mentioned above. The research in this chapter has been published (Larson et al. 1999).

Chapter 3: Uniform SSTs

3.1 Introduction

How clouds will respond to and feed back upon climate change is one of the largest uncertainties in climate prediction (Cess et al., 1996). Water vapor feedback is also crucial to climate change (Dickinson et al. 1996). In recent years much effort has been expended in attempts to better understand the role of clouds, water vapor, and large-scale circulation in the sensitivity of the tropical climate. Many different feedback processes have been investigated. It has been suggested that clouds may become brighter as the sea surface temperature (SST) increases and cause a negative feedback on the temperature of the tropics (Ramanathan and Collins 1991). The area coverage of high clouds in the tropics may change with SST, which could constitute a strong feedback through the radiative effects of clouds or water vapor (Larson et al. 1999; Lindzen et al. 2001). The cloud area, cloud properties and water vapor distribution are all strongly coupled to the large-scale circulation (Wallace 1992; Hartmann and Michelsen 1993). Because of the important role of water vapor, the ratio of the area of the tropics dominated by subsidence compared to the moist, convective region of the tropics is a critical quantity. This is because the tropics cool to space more efficiently in the subsidence regions without thick high clouds and with low upper tropospheric humidities (Pierrehumbert 1995). The net radiative forcing of the clouds in the high SST regions of the tropics is near zero at the top of the atmosphere (TOA) in observations (Harrison et al. 1990). So long as high clouds have a small effect on the energy balance, changes in the area coverage by deep convective clouds only affects the TOA radiation balance through their role in increasing upper tropospheric humidity (Larson et al. 1999). The net TOA cloud forcing by low clouds is negative, so that an increase in low cloudiness with increasing SST could produce a strong negative feedback in the

tropics (Miller 1997; Larson et al. 1999). The positive feedback of water vapor may be mitigated if the height of the tropical boundary layer decreases as the SST increases (Larson et al. 1999).

Cloud resolving models (CRMs) can simulate radiative convective equilibrium in the tropics. CRMs with horizontal resolution of about 1 km can explicitly resolve convective organization which is important for understanding clouds in the tropical climate. Tropical convection occurs at scales from meters to hundreds of kilometers and CRMs have been shown to compare well with observations for tropical convective regions (e. g. Xu and Randall 1997; Wu et al. 1998). The results of CRMs show the cloud mass flux, updrafts, downdrafts, and mesoscale organization associated with convection. Those quantities are assumed by convective parameterizations in coarser resolution models. CRM investigations help develop and test the assumptions made in cumulus parameterizations (e. g. Xu et al. 1992). Also CRMs have been used to study cloud-radiative interaction (e. g. Li et al. 1999; Fu et al. 1995), the diurnal cycle (e. g. Liu and Moncrieff 1998), tropical convection with large-scale forcing prescribed by observations (e. g. Sui et al. 1994; Grabowski et al. 1996), theoretical studies of convection (e. g. Robe and Emanuel 1996), and climate sensitivity studies to SST (Tompkins and Craig 1999; Lau et al. 1994).

With CRM simulations, Lau et al. (1994) concluded that cloud radiative forcing is more sensitive to imposed vertical velocity forcing than to the SST. Tompkins and Craig (1999, hereafter TC99) studied the response of a three-dimensional CRM on a 60 km square domain with 2 km resolution to imposed SST. They found a very small cloud feedback and that the microphysical processes exhibit no significant sensitivities to temperature, except that the cloud altitude is shifted upward by a surface temperature increase. The atmospheric temperature profile tends to follow a moist adiabat corresponding to the SST, so that the lapse rate decreases with increasing SST. The relative humidity profile did not change in their experiments. TC99 also found that the altitude at which cloud ice occurred increased with increasing SST.

CRM's must have fine grid spacing to resolve mesoscale aspects of convection.

It is computationally very expensive to run a CRM for a large domain in three dimensions. The domain of TC99 is too small to realistically represent the two-way interaction between convection and large-scale circulations. In this study, the nonhydrostatic version of the Pennsylvania State University (PSU) / National Center for Atmospheric Research (NCAR) mesoscale model, MM5, including representations of convection and clouds that interact with radiation, will be used to study interactions among clouds, large-scale circulation, and SST in the tropics. Using this model includes more cloud physics than a two column box model or general circulation model (GCM) and it is computationally faster than a GCM or CRM. An intercomparison of models for convection during the TOGA COARE (Tropical Ocean Global Atmosphere Coupled Ocean-Atmosphere Response Experiment) over the tropical pacific shows that the MM5 with doubly periodic boundary conditions compares favorably to CRMs (Su et al. 1999; Krueger and Lazarus 1999; Krueger and Lazarus 1998). A doubly periodic version of the MM5 will be used to study tropical processes in isolation from the effects of the extratropics or land masses. The primary advantage of this approach is to allow the study of large-scale interactions between regions with convection and regions with mean subsiding motion in a model framework with realistic cloud-radiative interactions.

In this chapter the sensitivities of the model are investigated when the model is forced by a uniform constant SST. The response of the model to constant SST is related to observations and previous detailed CRM studies to test some sensitivities of the clouds in the MM5 to uniform SST before SST gradients are applied. In chapter 4, SST gradients are imposed.

The horizontal and vertical distributions of total water will be solved for using prognostic cloud water equations. The model resolution will be moderately coarse (120 and 60 km), so that convective clouds will still be parameterized, but the interaction of the parameterized convection with radiation and the large-scale circulation will be explicitly included. This model can be used to investigate how the cloud and water vapor distributions interact with the large-scale circulations within the domain of the

model, and how these interactions depend on SST. In the experiments described here in part one, the entire domain will be given a single uniform SST, which will remain fixed for the entire integration. The following questions will be of interest: What fraction of the grid domain will contain convection and what fraction will be subsiding and dry, and how does this depend on the SST? As the fixed SST is changed within the range of 297 to 303K, how do the fraction covered by cloud, the optical properties of the clouds, and the water vapor distribution change? Do these changes depend on the uncertain details of the model or do they result from more basic physical considerations? What implications do these changes have for climate sensitivity?

In the next section the model is described in detail. Sections 3 and 4 describe the atmospheric and energy budget sensitivities to SST. The model TOA energy budgets show sensitivities to SST that are similar to the observed sensitivities. Finally, the water vapor and cloud feedbacks are described, followed by the conclusions. The research will be submitted to the *Journal of Climate* (Larson and Hartmann 2002a).

3.2 Model Description

The essential physical processes of dynamics, cloud processes, convection, radiation, and moisture advection will be allowed to interact in the model. Descriptions of these processes as implemented in the MM5 follow in the next subsections. The last subsection describes the experiments that were conducted to address the questions of interest here.

3.2.1 Dynamics

The nonhydrostatic version of the MM5 version 2 is used in this study. A general description of the MM5 can be found in Dudhia (1993) and Grell et al. (1994). Twenty-four vertical sigma levels are used, spaced at intervals of 0.01 (about 10 hPa) near the surface to 0.05 (about 50 hPa) above 900 hPa.

3.2.2 Boundaries

The MM5 was modified to run with periodic boundary conditions at both

north-south and east-west boundaries. To satisfy a periodic north-south boundary condition, the Coriolis parameter must be constant over the domain. In our experiments, the Coriolis force is set to zero because the Coriolis force is zero near the equator in the tropics. Geographical dependence of solar zenith angle is removed by using the solar zenith angle at the domain center to calculate incoming solar radiation at every grid point. The diurnal cycle of insolation is retained.

An upper radiative boundary condition (Klemp and Durran 1983) is employed to allow wave energy to pass through the upper boundary without being reflected. It has been re-programmed to apply to a doubly periodic domain and the 'Fastest Fourier Transform in the West' has been utilized in its implementation (Frigo and Johnson 1999).

The diffusion routines have been re-programmed for the double periodicity and the diffusion is fourth order at all grid-points. The periodic boundaries eliminate the need for second order diffusion at the boundaries.

3.2.3 Physics

The physics parameterizations used for these experiments include new parameterizations for the planetary boundary layer (PBL) and shallow cumulus convection developed at the University of Washington and the Kain-Fritsch cumulus parameterization (Kain and Fritsch 1990). The threshold value of boundary layer convergence in the trigger function in the Kain-Fritsch parameterization scheme was increased by a factor of 5 to force the convection to be more closely associated with resolved-scale upward motion. This modification was also made by Su et. al (1999) in their successful simulation of five days during TOGA COARE. The cloud and rainfall amount and fractional coverage resemble the observations in magnitude and time variation in that simulation.

The PBL and shallow convection scheme are described in Grenier and Bretherton (2001), McCaa (2001), McCaa et al. (2001, manuscript submitted to *Mon. Wea. Rev.*), and McCaa and Bretherton (2001, manuscript submitted to *Mon. Wea. Rev.*).

The planetary boundary layer scheme is based on Grenier and Bretherton (2001), and modified as described in McCaa (2001). Within the boundary layer, this parameterization predicts the time evolution of the turbulent kinetic energy using a 1.5 order turbulence closure model. The depth of the boundary layer evolves based on an entrainment closure described in Grenier and Bretherton (2001). The boundary layer scheme computes the surface fluxes according to the TOGA COARE algorithm (Fairall et al., 1996). The shallow cumulus scheme is activated for clouds of depths less than 4 km. The cloud mass flux is determined by a closure based on the turbulent kinetic energy and the convective inhibition (McCaa et al. 2002). The PBL and shallow convection schemes simulate the surface fluxes in the trade wind regime between California and Hawaii very well (McCaa and Bretherton 2002).

The grid-scale microphysical parameterization used in the model simulations is described in Reisner et al. (1998) and is based on Lin et al. (1983), Rutledge and Hobbs (1983) and Ikawa and Saito (1991). Cloud water, cloud ice, rain water and snow are all explicitly treated using this scheme. Prognostic equations of these variables include the effect of grid-scale advection of water species, phase changes such as condensation and evaporation, freezing and melting as well as sublimation and deposition. The number concentrations of cloud ice and snow are not predicted, which saves computing time. The microphysics scheme is used without modification for these tropical experiments.

3.2.4 Radiation

The Column Radiation Model, a stand-alone version of the column radiation code employed by the NCAR Community Climate Model (CCM3) is implemented in the MM5. The radiation code uses the δ -Eddington approximation for the shortwave radiation, and the longwave radiative transfer is implemented based on an absorbtivity/emissivity formulation. The effects of trace gases are included (Kiehl et al. 1996). The radiation scheme is important for these experiments since they are run for more than 30 days and the dominant balance in descending regions depends strongly on the radi-

ation over that time scale. The random overlap assumption in the CCM3 radiation scheme and the computation of cloud fraction and cloud liquid water path were modified as noted in Appendix B of McCaa (2001).

The random cloud overlap assumption used by the CCM3 radiation code leads to a great overestimation of total cloud fraction for multi-level clouds. The random overlap assumption is tolerated for shortwave radiative transfer, which features considerably more scattering and less absorption, but for longwave transfer, where even a single layer of cloud can have an optical depth much greater than one, a maximum random overlap assumption is implemented. Adjacent cloudy layers are assumed to have maximum overlap, while cloudy layers separated by one or more clear layers are assumed to overlap randomly.

Cumulus cloud fraction and cloud ice and water mixing ratio are provided from the UW shallow and Kain-Fritsch cumulus parameterizations. These are incorporated with the stratiform cloud amounts diagnosed from the explicit cloud ice and water fields into the cloud fraction used in the radiation code. Stratiform ice clouds are incorporated using the grid mean ice mixing ratio and assuming a cloud fraction of one in the presence of ice. Cloud liquid water and cloud fraction for warm stratiform clouds are diagnosed using the statistical cloud fraction scheme described below.

To provide a smooth transition between cloudy and clear sky, and crudely represent the variability in liquid water path, a statistical cloud fraction scheme for stratiform clouds like that described in McCaa (2001) is used. It is based on an assumed normal distribution of saturation excess about its layer mean value. Assuming the standard deviation of saturation excess is proportional to the saturation mixing ratio, the stratiform cloud fraction and the expected liquid water mixing ratio can be diagnosed.

The model has separate diagnostic values of stratiform and cumulus cloud fractions and liquid water mixing ratios which must be combined to be input into the radiation scheme. Cumulus rising into or through stratiform cloud layers are assumed to be collocated with the stratiform clouds so that the total cloud fraction is just the maximum of the stratiform and cumulus cloud fractions. The effective mean liquid water

mixing ratio of the two types of cloud should avoid smearing the cumulus cloud water throughout the potentially much larger area of the stratiform cloud. It is therefore computed as a log-weighted average, which can be integrated vertically to get the cloud liquid water path.

3.2.5 Experiments

Several experiments were executed at the constant SSTs of 297 K, 299 K, 301 K, 303 K, that represent a range of tropical SSTs. For each SST three different initial conditions are used: an initial wind of 5 m s^{-1} and initial air temperature profiles roughly corresponding to the SST, an initial wind of 3.54 m s^{-1} and a warmer initial temperature profile, a calm initial wind and a colder initial temperature profile. The different initial conditions are used to gain greater sample diversity and statistical significance. In this paper, the experiments with different initial conditions but the same SST are averaged together and 95% confidence limits are computed for the averages. This gives a good sense of whether the model responses to SST changes are robust.

The basic experiments have a domain of 16×16 grid-points with a grid spacing of 120 km. Additional experiments with 60 km resolution in a 32×32 grid-point domain are investigated to explore the sensitivity of the results to horizontal resolution. For most of the tested variables, the response to the horizontal resolution change is no bigger than the sampling uncertainty. The average values for the experiments are computed from data taken every 6 hours for days 60 - 90 of the experiments. After 60 days the experiment has reached a statistical equilibrium and the 30-day average is sufficient to give reliable results.

3.3 Atmospheric Sensitivities to SST

The model atmosphere is sensitive to the imposed SST. The areal coverage of high clouds increases along with the temperature, rain rate, integrated water vapor and cloud ice as the SST increases. The upper tropospheric humidity increases slightly as the SST increases and the amount of integrated cloud water decreases. Composites of the convective and non-convective regions of the experiments give insights about the

temperature profile, inversion height and cloud water amounts. Comparisons of the atmospheric sensitivities to SST are made with CRMs when possible.

3.3.1 Temperature and Humidity

Figure 3.1 shows the moist static energy and the larger saturation moist static energy for the four different SSTs. The saturation moist static energy is almost con-

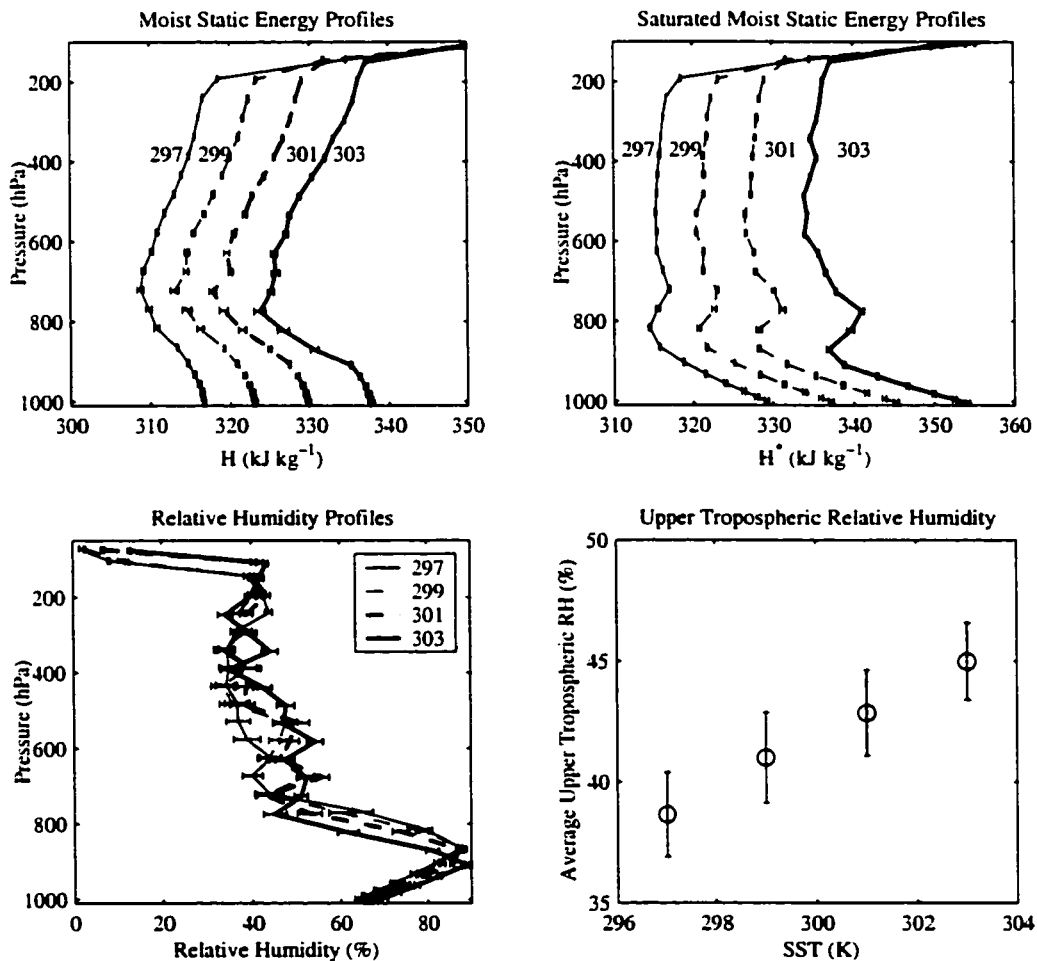


Figure 3.1 Vertical profiles of relative humidity, moist static energy, and saturated moist static energy for the 4 different SSTs, 297 K (thin solid), 299 K (thin dashed), 301 K (thick dashed), and 303 K (thick solid). Average upper tropospheric relative humidity versus SST. The 95% confidence intervals are indicated with error bars.

stant with height above the boundary layer, meaning the atmospheric temperature is following a moist adiabat. The constant saturation moist static energy values for each

SST are evenly spaced about 6 kJ kg^{-1} apart, except the difference between the 301 K and 303 K experiments is about 7 kJ kg^{-1} . One can see that the inversion in saturated moist static energy increases in strength and moves downward with increasing SST. The relative humidity linearly increases from about 65% at the surface to the maximum of about 90% near 875 hPa (Fig. 3.1c). A dry layer occurs above 700 hPa; with relative humidity values between 35% to 55% for every SST. The average relative humidity in the dry layer of the upper troposphere from 250 hPa to 750 hPa is helpful in comparing the experiments (Fig. 3.1d). The upper tropospheric relative humidity increases slightly with increasing SST. High relative humidity above the level of the tropical inversion is associated with convection (Udelhofen and Hartmann 1995). The increase in upper tropospheric relative humidity would be consistent with increased high cloud amount or increasing area of convection. Because the relative humidity values are similar while the temperature increases, the specific humidity increases with increasing SST, giving strong positive water vapor feedback.

Figure 3.2 shows the SST versus the integrated water vapor for these experiments, observations using satellite data, and the CRM experiments of TC99 and Lau et al. (1994) and Sui et al. (1993) (hereafter the combination is referred to as LS93). Two of the LS93 experiments were forced by rising motion and they have the highest water vapor amounts. The TC99 simulations are moister than the observations and these MM5 simulations are drier. The dryness of these experiments is due to the smaller relative humidities at the surface and the upper troposphere when compared to the other simulations and a cold mean mass-weighted temperature in the MM5. The domain for these experiments is $1920 \text{ km} \times 1920 \text{ km}$, much larger than the 3D domain of TC99 ($60 \text{ km} \times 60 \text{ km}$) and still larger than the 2D domain of LS93 (768 km). The large domain contains a several grid-point region with persistent subsidence where no rain or high clouds have occurred in days. This subsidence region persists and migrates across the domain. Deep and shallow convection occur in the rest of the domain. The

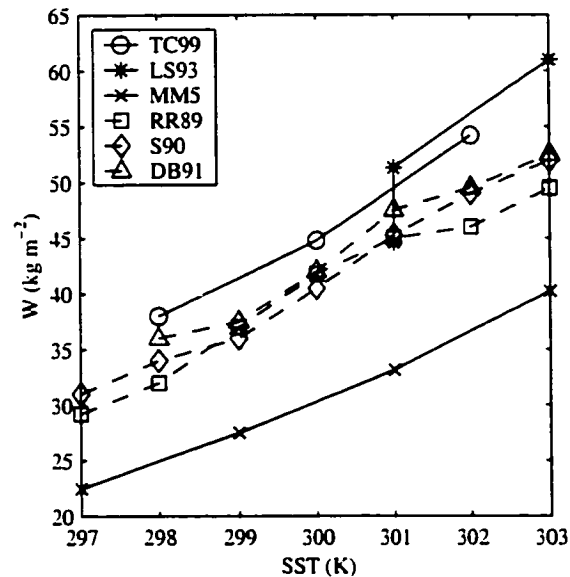


Figure 3.2 Integrated water vapor versus SST for the MM5, CRMs, and observations. The model results are connected by solid lines and the observations by dashed lines. RR89 refers to the paper by Raval and Ramanathan in 1989. S90 is the paper by Stephens in 1990. DB91 is the paper by Duvel and Bréon in 1991.

region of persistent subsidence decreases the average relative humidity in the upper troposphere and is responsible for the dryness of the experiments (Held et al. 1993).

Comparison of the mean temperature among the simulations shows these simulations have colder mean mass-weighted temperatures than TC99 or LS93. A SST of 303 K in the MM5 produces almost the same mean mass-weighted temperature as an SST of 300 K for TC99 and 301 K for LS93. The coldness of the simulations may be related to weaknesses in the MM5. Dry air, from persistent subsidence in the large domain, entrained in the planetary boundary layer (PBL) may contribute to overmixing in the PBL and to a cold bias in the PBL that affects the mean mass-weighted temperature. The PBL was found to have too much mixing, producing a cold bias in the PBL by McCaa (2001). For experiments with similar mean mass-weighted temperatures, the MM5 still is drier than the CRM experiments. However, the moist region of the MM5 has similar integrated water vapor to the CRM experiments with no forced vertical motion. The reason the MM5 is drier for similar mean mass-weighted temperatures is because the large domain allows for regions of persistent subsidence. Salathe

and Hartmann (1997) found air becomes drier the longer it is away from the moistening of deep convection in the tropics. The CRMs do not have as large domains so air parcels are not as dry because they do not spend as much time away from convection as is possible with the large MM5 domain.

One dimensional MM5 simulations were conducted using the same physics as the coarse resolution, uniform SST simulations, except that large-scale advection was eliminated. In the 1-D simulations the cloud ice and water accumulate to much larger values than in the coarse resolution simulations, which cools the mean mass-weighted air temperature and gives higher relative humidities and integrated water vapor amounts. The 1-D simulations point to the importance of the large-scale circulation in warming and drying the atmosphere.

The Clausius-Clapeyron relation suggests that saturation vapor pressure should increase with temperature about 6% per degree (Hartmann, 1994, Appendix B). Comparing the 303 K and 297 K simulations gives an increase in integrated water vapor of about 9% per degree of SST. The model value is larger than expected because the tropospheric air temperature increases more than the SST and the relative humidity increases a little with SST also. The average precipitation rate increases about 0.1 mm day⁻¹ per degree of SST increase, or about 4% per degree (Fig. 3.3). The evaporation rate must increase by the same amount as the precipitation rate in equilibrium to conserve atmospheric water vapor. Lau et al. (1994) found a 13% increase in convective precipitation when they increased the SST from 301 K to 303 K with imposed vertical motion, or about 6.5% per degree. Here and in Lau et al. (1994) the rate of change of precipitation is much less than the rate of increase of saturation vapor pressure. The reason that the precipitation does not increase at the rate of the saturation vapor pressure is that the precipitation rate over the ocean is not constrained by the source of moisture, but rather by the rate at which other processes such as radiative cooling and horizontal transport can remove heat from the atmosphere (e. g. Hartmann 1994, section 6.2). The heating that is provided to the atmosphere by latent heat release and tur-

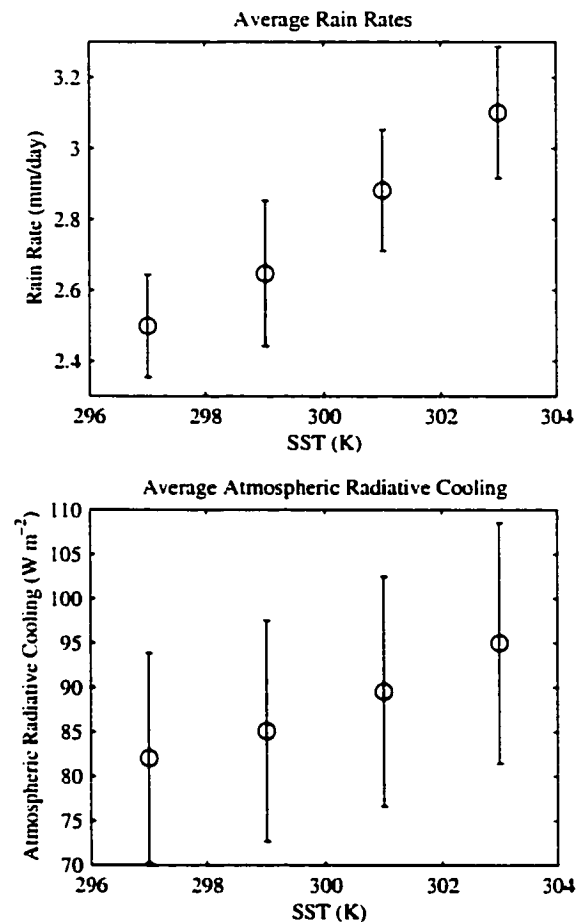


Figure 3.3 Average values of the rain rate and radiative cooling for the 4 different SSTs. The 95% confidence intervals are noted.

bulent sensible heat flux from the surface must be removed by radiation in the present experiments which do not include horizontal transport out of the domain. Lau et al. (1994) imposed a specified vertical motion that can export a variable amount of energy out of the domain, depending on the vertical profile of moist static energy, so that the rate of increase of precipitation with SST could be larger than that found here. The rate at which radiation can cool the atmosphere does not increase with temperature as rapidly as the saturation vapor pressure, and so the precipitation rate is constrained to increase more slowly than the saturation vapor pressure. The radiative cooling rate increases about 3% per degree of SST increase. Within the 95% confidence intervals, the precipitation and the radiative cooling increase at the same rate with SST, and they

do not increase as fast as the integrated water vapor or the saturation vapor pressure (Fig. 3.3).

The energy balance in the tropical atmosphere is between radiative cooling and moist convection and condensation (Fig. 3.4). Close to the surface vertical diffusion is

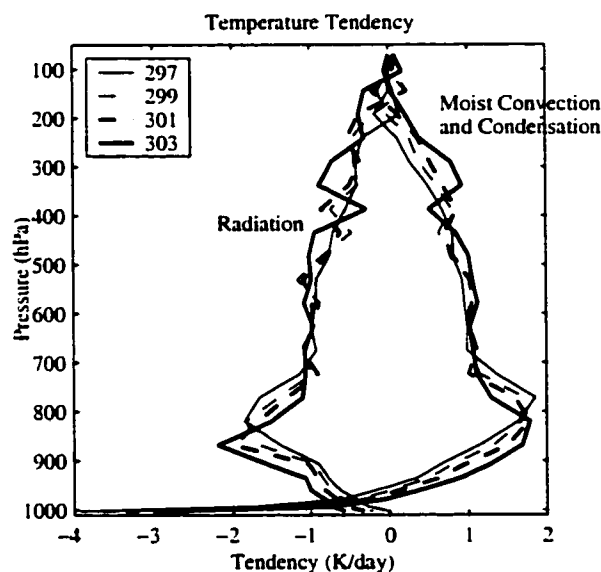


Figure 3.4 Vertical profiles of temperature tendency for the radiation and moist convection and condensation terms of the energy budget for the 4 different SSTs, 297 K (thin solid), 299 K (thin dashed), 301 K (thick dashed), and 303 K (thick solid).

also important, but those terms are not shown in Fig. 3.4. The level of strongest radiative cooling is near the steepest gradient in specific humidity between 800 hPa and 900 hPa. The altitude of this level decreases with increasing SST. The upper tropospheric level where the radiative cooling rate is 0.5 K day^{-1} rises as the SST increases, but the temperature there remains constant at approximately 212 K. Radiative cooling above this level is inefficient because the water vapor amount is so small in the upper troposphere (Hartmann et al. 2001a). The fact that the temperature is nearly constant at the level where the radiative cooling rate reaches 0.5 K day^{-1} has implications for climate sensitivity that are discussed in Hartmann and Larson (2002, manuscript submitted to *Geophys. Res. Lett.*). The emission temperature of anvil clouds may remain constant during climate change, so long as the tropopause is colder than the temperature where

emission from water vapor becomes relatively small.

Figure 3.5 shows the water profiles in the constant SST experiments. The cloud ice

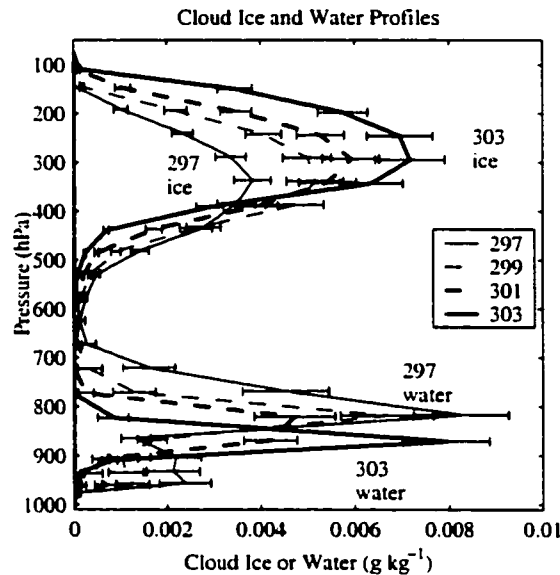


Figure 3.5 Vertical profiles of cloud water and cloud ice for the 4 different SSTs, 297 K (thin solid), 299 K (thin dashed), 301 K (thick dashed), and 303 K (thick solid). The 95% confidence intervals are noted.

profile is peaked in the upper troposphere. The peak values are larger and occur at higher levels as the SST increases. The cloud ice profile peaks at higher levels for warmer SSTs in TC99 and LS93 as well because the freezing level increases with height as the air temperatures increase. The cloud water profiles do not show a discernible trend in magnitude, but the peak values occur at lower levels for higher SSTs, consistent with the lowering of the level of maximum radiative cooling with SST. The average values of the integrated liquid water and ice amounts are shown in Fig. 3.6. The trends of integrated cloud liquid water and ice are consistent with Fig. 3.5. As the SST is increased the liquid water decreases and the ice increases. In the warmer SST cases ice is formed instead of liquid water in the convective region and most of the cloud liquid water is found in regions of subsidence. The sum of the integrated cloud ice and liquid water is approximately constant with SST. Producing more ice and less

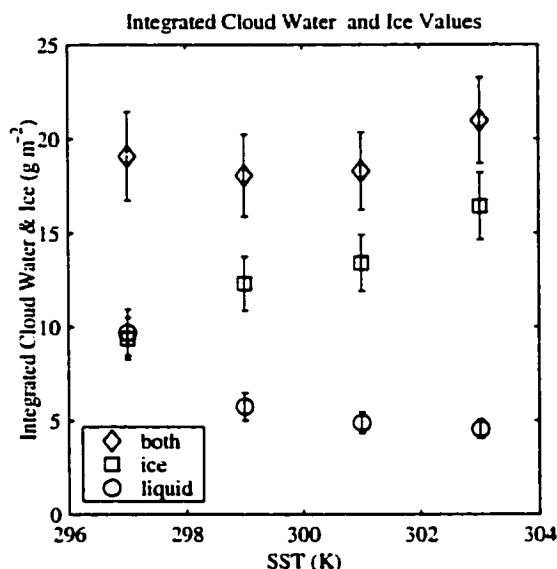


Figure 3.6 Average values of the integrated cloud liquid water, and integrated cloud ice and the sum of all cloud water. The 95% confidence intervals are noted.

liquid water at higher SST is possible if the convection is more energetic and reaches higher in the troposphere for higher surface air temperatures. More energetic convection is consistent with the increase of moist convection and condensation with SST at 300 hPa in Fig. 3.4.

The cloud water and cloud ice values affect the cloud fraction in the experiments. The cloud top pressure is defined here as the level where the visible optical depth reaches 0.1. If the cloud optical depth is less than 0.1 it is grouped in the clear-sky category. Consistent with the International Satellite Cloud Climatology Project (ISCCP) definitions (Schiffer and Rossow 1985; Rossow and Schiffer 1999) high clouds are defined to have tops at or above 440 hPa and the low clouds have tops at or below 680 hPa, while the middle clouds have tops between those values. Figure 3.7 displays the percentage of the area where clear skies, high clouds, middle clouds and low clouds are present, using radiative fluxes output every 30 minutes and averaging over the third 30 days of the experiments. The finer resolution in time makes it possible to identify rapidly changing cloud tops accurately, as the convective time scale can be less than 6 hours. The high cloud cover increases with increasing SST, consistent with the

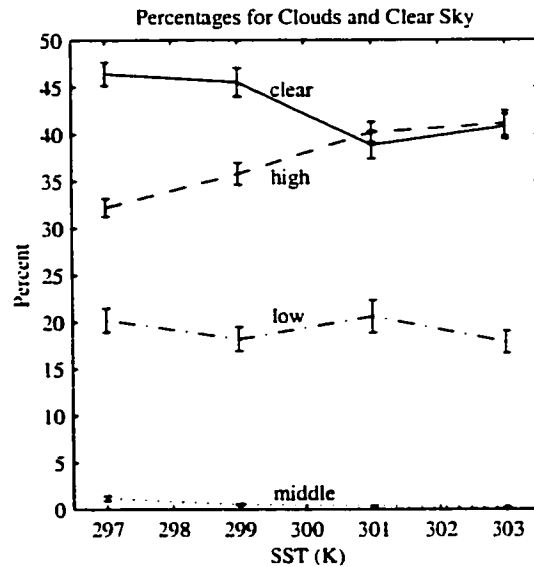


Figure 3.7 Clear-sky, high, middle, and low cloud amount for the constant SST experiments. The line type denotes the cloud type. The 95% confidence intervals are noted. increase of integrated cloud ice. The areas of middle clouds and low clouds decrease less than the area of high clouds increases with increasing SST, so that the clear fraction decreases with SST. The decrease of middle and low clouds may mean that the lower clouds are overlapped by the increasing amounts of high clouds, it does not necessarily mean the amounts of lower clouds are decreasing, because only the highest cloud top is found at each grid-point in agreement with satellite observations. The probability of seeing a middle level cloud in the model is very low.

3.3.2 Convective Area Fraction

The ratio of the convective area to the subsidence area is an important concept in the analysis of climate sensitivity (e.g. Pierrehumbert 1995; Larson et al. 1999; Lindzen et al. 2001). The convective area can be defined as a region of high relative humidity with high clouds and upward motion. The subsidence region is defined by downward vertical velocities, and often contains lower upper tropospheric relative humidity. Low clouds are present, but noticeably absent in this region are optically thick high clouds. The vast majority of the rainfall and the deep, optically thick clouds are expected to occur in the convective region. The definition of convective and non-

convective areas is important and several objective methods of separating these regions have been investigated.

The rain rate, and the integrated cloud ice are variables that can be used as indices to define the convective regions. Because the convective regions move around within the model domain, the average value of these variables in space or time will not describe the convective region accurately. Rather, these variables are used to define the convective area every 6 hours for days 60 to 90 of the experiment. Integrated cloud ice and rain rate are used to define convective areas by choosing a threshold value and finding the percent of the domain that is above that value.

High clouds thicker than 0.1 optical depth can be used to indicate the convective region, which is roughly equivalent to integrated ice water greater than 1 g m^{-2} . The integrated cloud ice threshold of 1 g m^{-2} gives convective area fractions that are within 1% of the high cloud amounts defined with the optical depth criterion (Fig. 3.8). Using

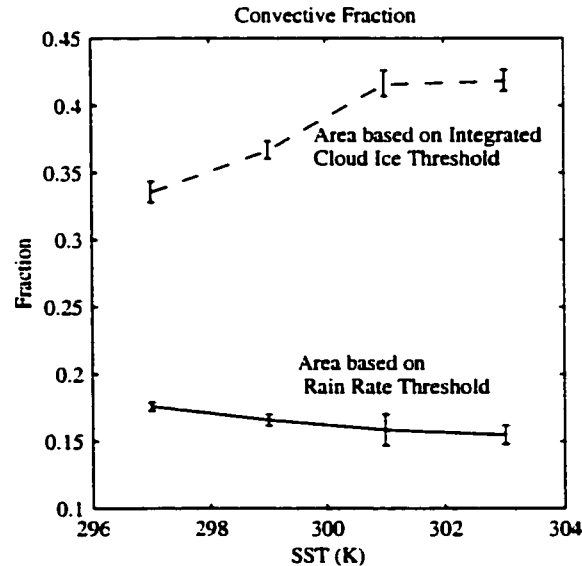


Figure 3.8 Fraction of the domain above the convective threshold for integrated cloud ice, and rain rate. The convective threshold for integrated cloud ice is 1 g m^{-2} . The convective threshold for rain rate is 1 mm day^{-1} . The error bars represent the 95% confidence limits.

these definitions, the convective fraction increases with increasing SST. The convective

tive area increases with SST at a rate of $1.5\% \text{ K}^{-1}$ for the integrated cloud ice. The integrated cloud ice threshold is equivalent to dividing the domain into regions with and without high clouds.

The rain rate for these constant SST cases is mostly associated with deep convection. The drizzle in the subsidence region produces a rain rate that is at least an order of magnitude smaller than the rain rate typically found in the deep convective parts of the domain. If a threshold rain rate of 1 mm day^{-1} is used, then the rain rate indicates deep convection. Because some parts of the domain are in the convective region with high clouds and with high humidity but not rain, the convective area using the rain rate threshold is about 16%, much less than for the integrated cloud ice threshold (Fig. 3.8). The fraction of the domain where it is raining does not change very much with increasing SST, just like the sum of the integrated cloud liquid water and ice. The increasingly energetic convection makes more cloud ice and less cloud water as the SST increases.

The reason why the convective fraction has different slopes with SST for the integrated cloud ice threshold and the rain rate threshold, or why the total integrated cloud and ice water stays approximately constant while the integrated cloud ice amount increases and the integrated cloud liquid water amount decreases is dependent on the representation of convection in the model. Deep convection occurs via the Kain-Fritsch cumulus parameterization which controls the trigger function, cloud updraft and downdraft representations, and the cloud mass flux closure assumptions. LS93 and TC99 describe few changes in convection due to SST changes. In LS93, this is perhaps related to the constant forced vertical motion while the SST is changed. The constant convective area defined by the rain rate threshold suggests that the area with active convection remains constant with increasing SST, consistent with the CRMs. The increase of cloud ice, decrease of cloud water, and stronger inversion are consistent with increasingly deep convection with increasing SST, a physically reasonable result.

Using the thresholds of integrated cloud ice and rain rate, two sets of composites are made of the average values in the convective and non-convective regions. These composites show that the relative humidity is higher in the convective (high cloud, raining) regions than in the non-convective regions (Fig. 3.9a). The upper tropospheric relative humidity is approximately constant with respect to SST in the convective region, and increases in the non-convective region (Fig. 3.9b). The convective fraction also increases with increasing SST, which contributes to the increase in average upper tropospheric relative humidity.

The average vertical velocity is upward in the convective regions and downward in the non-convective regions, as expected (Fig. 3.9c). In the non-convective region, subsidence warming balances radiative cooling. Because the lapse rate decreases with increasing SST and the radiative cooling increases in association with increases of humidity of the atmosphere, these effects offset each other and the non-convective vertical velocity is similar with changing SST. The larger decrease in the vertical velocity profiles of the convective region is due to the increase in convective area with increasing SST. The large-scale circulation in these simulations is constrained by the balance between radiative cooling and subsidence warming in the non-convective region.

Composites for cloud water in the non-convective region defined by the cloud ice threshold are shown in Fig. 3.10a. Results are very similar if the rain rate threshold is used. The non-convective cloud water profiles show a definite downward shift of the layer with maximum cloud water as the SST is increased. This result agrees well with Larson et al. (1999), who predicted the boundary layer height in the subsiding region should decrease with an increasing value of the moist adiabat above the layer. Larson et al. (1999) showed that the lowering of the boundary layer height with increasing SST caused a significant reduction in the greenhouse effect of the atmosphere.

The difference in temperature profile for the convective and non-convective

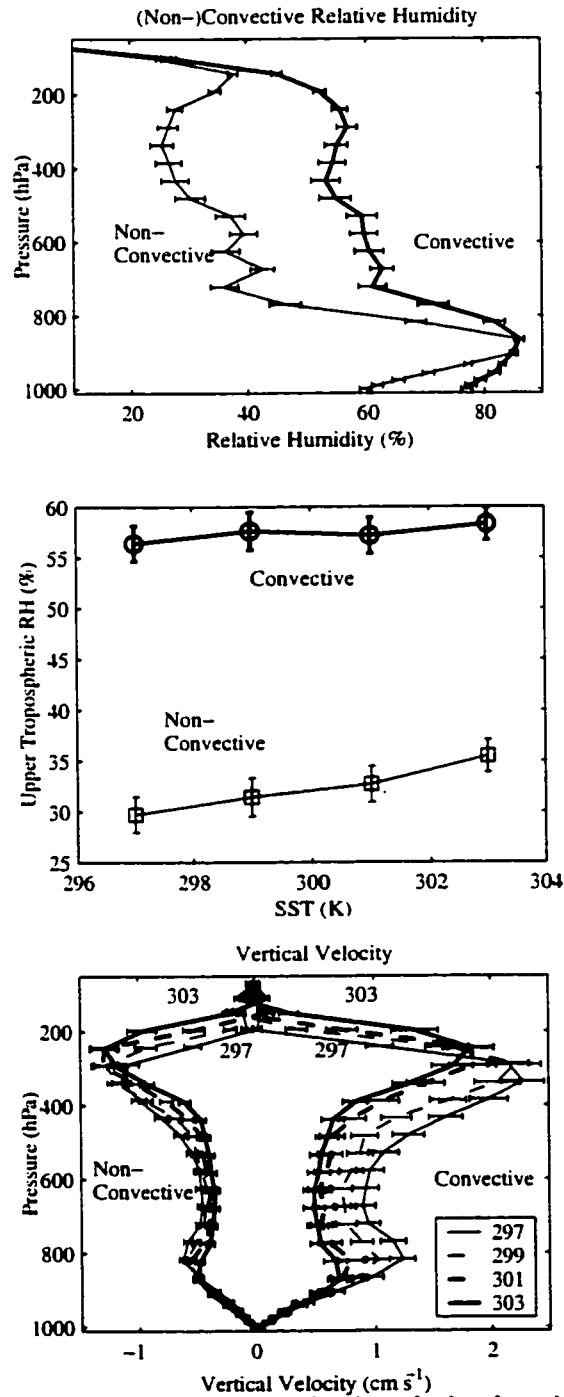


Figure 3.9 Relative humidity, upper tropospheric relative humidity and vertical velocity for the convective and non-convective regions for composites based on integrated cloud ice. Four different SSTs and the 95% confidence limits are noted, 297 K (thin solid), 299 K (thin dashed), 301 K (thick dashed), and 303 K (thick solid).

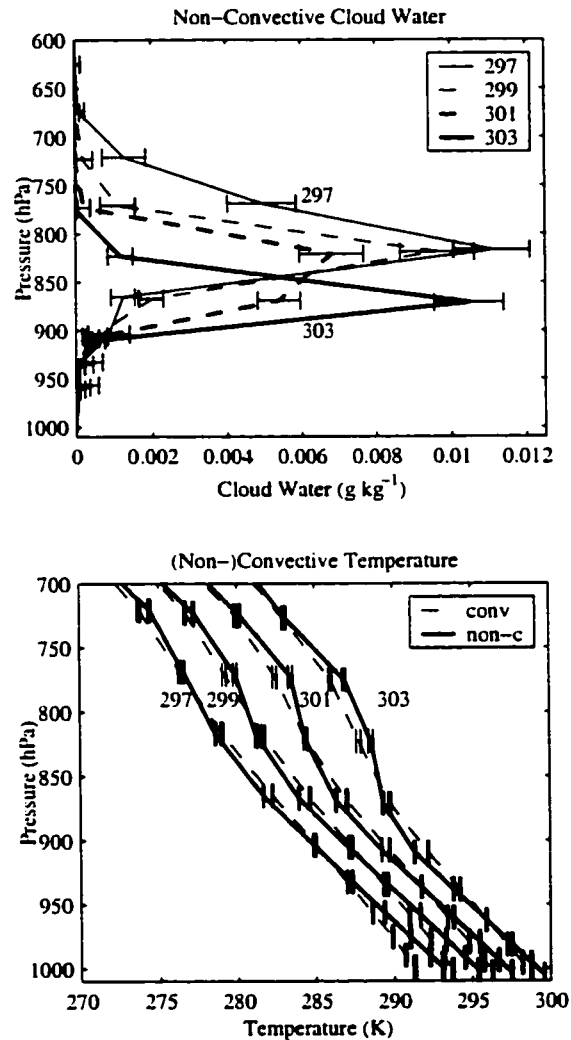


Figure 3.10 Vertical profiles of relative humidity, cloud water and temperature for the convective and non-convective regions for composites based on integrated cloud ice. Four different SSTs and the 95% confidence limits are noted, 297 K (thin solid), 299 K (thin dashed), 301 K (thick dashed), and 303 K (thick solid). For the temperature, the convective profile is dashed and the non-convective profile is solid.

regions can be seen in Fig. 3.10b. Only the lower portion of the atmosphere is shown because the temperature profile is very uniform across the entire domain above 700 hPa. It is a common trait of the tropics that the horizontal temperature gradient is small in the upper troposphere (Sobel et al., 2001). The convective profiles have a colder temperature near the surface and a relatively constant lapse rate in the lower troposphere. The non-convective profiles have a warmer temperature near the surface and a

weaker lapse rate suggestive of an inversion between 800 and 900 hPa. The inversion moves downward and gets stronger with increasing SST, which is consistent with the lowering of the cloud water in the non-convective region.

In summary, the water vapor content of these simulations is less than in satellite observations and other CRMs. The model has a cold bias and a drier atmosphere than CRMs due to the large domain of these simulations and a persistent region of subsidence in the simulation. The temperature profile follows a moist adiabat and the vertical relative humidity profile is not very sensitive to the SST, but the upper tropospheric relative humidity increases slightly as the SST increases. As the SST increases the total integrated liquid and ice water content and convective area based on rain rate threshold stay constant, the average rain rate, integrated cloud ice, and convective area defined by the integrated cloud ice threshold increase, and the integrated cloud liquid water decreases. The basic state of the atmosphere in the constant SST experiments and the changes due to increasing the SST have been described. Further analysis of the radiation quantities and cloud and water vapor feedbacks follows in the next sections.

3.4 Comparison with Observed Sensitivities of Energy Budget to SST

The implications of these simulations for climate sensitivity can be examined by considering the sensitivity of the outgoing longwave radiation (OLR), net absorbed shortwave radiation (SWI) and net radiation to the imposed SST. In addition, the relative roles of different sky types (high clouds, low clouds, clear skies, and the average of all sky types) are considered. Figure 11 shows the OLR, absorbed shortwave, and net incoming radiation for different sky types as functions of SST. The OLR of the high clouds decreases with increasing SST, because the cloud tops become slightly colder and the ice optical depth increases. The high cloud top temperature where the ice optical depth reaches 0.1 is approximately 200 K for all the simulations (Hartmann and Larson 2002). The OLR for clear skies increases because the SST and air temperatures increase. The OLR for low clouds increases because the height of the tempera-

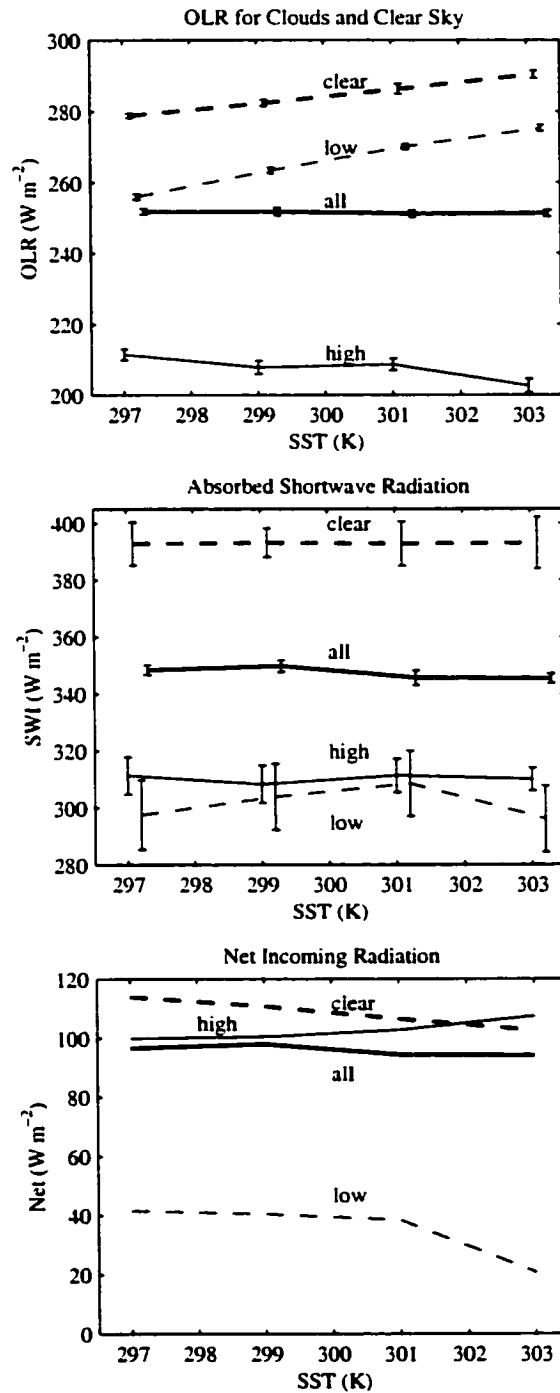


Figure 3.11 OLR, net absorbed shortwave radiation and net incoming radiation at the top of the atmosphere. The 95% confidence intervals are noted. The high cloud top temperature inversion decreases with increasing SST and the low cloud top temperature increases faster than the SST. The high cloud OLR for the high resolution experiments

is lower than for the coarse experiments, because the cloud top temperature is about 1 K colder than for the coarse resolution experiments and the ice optical depth is larger. The upper tropospheric relative humidity increase per degree SST is 2% (compared to 1% in the coarse resolution experiments, not a statistically significant difference), which leads to a smaller increase in clear-sky OLR with SST in the high resolution experiments. The mean OLR decreases slightly with SST because the cloud amount increases and the high cloud OLR decreases with SST for all of the experiments at both resolutions. Earth Radiation Budget Experiment (ERBE) values of OLR for average and clear-sky conditions are 253 W m^{-2} and 288 W m^{-2} , respectively, very comparable to the results of these simulations.

3.4.1 Accounting for Diurnal Variations

In order to properly calculate the effect of cloud types on the solar and net radiation, the diurnal variation of insolation and cloud amount must be handled carefully. The high and low clouds in the model both have a diurnal cycle in their area coverage. The high clouds have a diurnal maximum of area coverage near midnight and a minimum near noon. The diurnal cycle in the area coverage by high clouds has a peak-to-peak amplitude of about 8%, around a mean value of 41% for the 303K SST case. ISCCP data show a high cloud percentage that exceeds 40% in a large area over the west Pacific warm pool (e.g. Hartmann, et al. 2001). Geosynchronous satellite data show a nighttime maximum and daytime minimum of high clouds over the tropical ocean, although the diurnal cycle varies greatly from place to place (e.g. Albright et al. 1985, Hartmann and Recker 1986, Janowiak 1994, Chen and Houze 1997).

The low clouds in the experiments have a maximum area extent just after sunrise, and a minimum in mid-afternoon, with about a 10% peak-to-peak variation in the cloud cover. Observations from ISCCP, assuming random overlap of high clouds over low clouds, show a maximum low cloud area coverage at 3 a.m. local time and a minimum at 3 p.m. local time, with a maximum variance over the Eastern Pacific of 10% (Rozendaal et al. 1995). The model produces a fairly realistic diurnal cycle of low

clouds.

Because the cloud fraction varies during the day, some care must be taken to obtain appropriate sensitivities from the numerical experiments. In order to make the cloud fractions for shortwave radiation consistent with those for longwave, the shortwave radiation values for each sky cover (e.g. high cloud, low cloud and clear sky) have been multiplied by the average sky cover divided by the insolation-weighted sky cover. These values are computed by summing over the 48 half-hour sampling periods during the day. This factor adjusts the values so that the clear sky, high and low cloud values can be linearly combined to make the correct average shortwave flux.

The absorbed shortwave flux does not show significant sensitivity to the SST for any of the sky types or for the sum of all sky types (Fig. 3.11b). The total SWI decreases slightly with increasing SST because the cloud amount increases. ERBE observations show the average SWI is about 325 W m^{-2} and the clear-sky average is 370 W m^{-2} , both values are comparable to the results from these simulations. The net radiation has a weaker dependence on SST than do OLR and SWI (Fig. 3.11c). The clear-sky net radiation decreases slightly with increasing SST because clear-sky OLR increases with SST as the net result of the water vapor, temperature and lapse rate feedback. The high cloud net radiation has a small positive increase with increasing SST and the net radiation for low clouds decreases with increasing SST, both because of the OLR sensitivity. The average net radiation has a very small decrease with increasing SST.

Both the coarse and high resolution experiments show a small change in the net TOA radiation with increasing SST. In the high resolution experiments, the high and low clouds are more reflective than in the coarse resolution simulations. The net absorbed shortwave radiation by high clouds increases slightly with SST, which is larger than the effect of the increasing high cloud coverage, and leads to a slight decrease of the total net absorbed shortwave radiation with SST in the high resolution simulations. The high resolution clear-sky net radiation does not decrease as strongly as the coarse resolution with SST because of the difference in the clear-sky greenhouse

effect. The high resolution net radiation increases slightly with increasing SST, but this is consistent within the sampling uncertainty agreeing with the small decrease in net radiation for the coarse resolution experiments.

3.4.2 Comparison to Observations

The sensitivity of the TOA radiative fluxes to SST was estimated from ERBE observations in HM93 by comparing the changes of radiation quantities and SST between La Niña and El Niño years averaged over large regions of the Pacific Ocean. Table 3.1 compares estimates from HM93 with estimates obtained from least squares fits of the radiation budget values from the model to the imposed SST for the 12 coarse resolution experiments. Values for which the explained variance is less than 0.5 are in italics, this is most common when the slope is close to zero. The table shows these model experiments give similar sensitivities to those obtained by averaging observations from 20 °N - 20 °S or 30 °N - 30 °S in the Pacific Ocean region. It is appropriate to compare observations averaged over the rising and sinking branches of the Hadley and Walker Circulations to averages of the model domain in which the vertical motion averages to zero.

These results can be compared to those of Lau et al. (1994), who calculated sensitivities of the TOA and surface energy budgets from CRM experiments with different SSTs and with and without forced rising motion. Changes of the energy budgets due to SST in these simulations show blackbody radiation and the atmospheric greenhouse effect are more sensitive to SST than the longwave and shortwave cloud forcings (Table 3.1). Lau et al. (1994) found similar sensitivities to SST using CRM simulations with SSTs of 301K and 303 K forced with rising motion. Using uniform SST CRM simulations with and without forced rising motion, Lau et al. (1994) calculated very large sensitivities of the shortwave and longwave cloud forcing to rising motion. These large cloud sensitivities are similar to the large values of cloud sensitivities in Table 3.1 when the observations are averaged from 5 °N - 5 °S or 10 °N - 10

Table 3.1 The sensitivity of radiative energy balance components to SST. The “Pacific” is defined as the ocean areas falling within the longitude range of 120° E to 70° W. The units on all the quantities are $\text{W m}^{-2} \text{K}^{-1}$. Subscript CS indicates a clear-sky value. OLR = outgoing longwave radiation at the top of the atmosphere, G = total greenhouse effect of atmosphere = $\sigma T_S^4 - \text{OLR}$, G_a = clear atmosphere greenhouse effect = $\sigma T_S^4 - \text{OLR}_{CS}$, C_l = longwave forcing by clouds = $\text{OLR}_{CS} - \text{OLR}_{cs}$, SWI = absorbed solar radiation, C_s = shortwave cloud forcing = $\text{SWI}_{CS} - \text{SWI}$, R^∞ = net radiation at the top of the atmosphere.

Variable	5°N - 5°S 180-90 W	10°N-10°S Pacific	20°N-20°S Pacific	30°N-30°S Pacific	Experiment
$4\sigma T_S^3$	6.2	6.2	6.1	6.1	6.1
$\frac{d\text{OLR}}{dT_S}$	-20.5	-12.5	-0.7	2.8	-0.1
$\frac{d\text{OLR}_{CS}}{dT_S}$	-2.6	-1.0	1.6	1.8	1.7
$\frac{dG}{dT_S}$	26.7	18.6	6.9	3.3	6.2
$\frac{dG_a}{dT_S}$	8.7	7.1	4.6	4.3	4.4
$\frac{dC_l}{dT_S}$	18.0	11.5	2.3	-1.0	1.8
$\frac{d\text{SWI}}{dT_S}$	-21.0	-12.1	-0.7	1.9	-0.7
$\frac{d\text{SWI}_{CS}}{dT_S}$	0.6	0.4	0.1	0.4	0.0
$\frac{dC_s}{dT_S}$	-21.6	-12.5	-0.8	1.1	-0.7
$\frac{dR^\infty}{dT_S}$	-0.5	0.3	0.0	-0.9	-0.6
$\frac{dR_{CS}^\infty}{dT_S}$	3.1	1.4	-1.5	-1.4	-1.7
$\frac{dC_s}{dT_S} + \frac{dC_l}{dT_S}$	-3.7	-1.0	1.5	0.6	1.1

°S. The MM5 simulations don't have forced vertical motion, but averages for the

entire simulation can be compared to averages over areas with rising motion in the simulations to assess sensitivities to rising motion similarly to Lau et al. (1994).

Since the convective and non-convective regions defined with the integrated ice amount have mean vertical velocities that are upward and downward, respectively, the convective and non-convective regions can be used to estimate sensitivity to vertical motion. Using this definition, the MM5 also shows shortwave and longwave cloud forcing at the TOA have large sensitivities to vertical motion. At the surface, these simulations and Lau et al. (1994) find the shortwave radiation sensitivity to rising motion is bigger than any other sensitivity. Latent heat flux shows different sensitivities, probably because the latent heat flux in the CRM simulations uses a minimum wind speed of 4 m s^{-1} . For both models, the TOA cloud forcing is much more sensitive to the vertical motion than to the SST.

3.5 Cloud, Water Vapor and Lapse Rate Feedbacks

The model experiments can be used to estimate values of the climate feedback parameter and its dependence on various feedback processes that operate within the model. The feedback parameter measures the ratio of the equilibrium temperature change (dT_s) in response to an imposed climate forcing (dQ) (e.g. Hartmann, 1994 eqn. 9.2),

$$\frac{dT_s}{dQ} = \lambda. \quad (3.1)$$

Since the SST is fixed in these experiments, the feedbacks must be evaluated using the inverse technique as in Cess et al. (1990), Zhang et al. (1994), TC99 and others, where the SST perturbation is imposed and the radiative response at the top of the atmosphere is examined after the atmosphere has reached a new thermodynamic equilibrium. The net radiation at the top of the atmosphere R ,

$$R = \text{SWI} - \text{OLR}, \quad (3.2)$$

is substituted for Q in equation 3.1 and the sensitivity parameter, λ , can be estimated.

As the SST is perturbed, the mean temperature, the lapse rate, the water vapor amount, and the cloud properties of the atmosphere all change. To isolate the effect of each process, the overall atmospheric feedback in the experiments is partitioned linearly (assuming no interaction between the feedback effects) as follows:

$$\lambda = \frac{dT_s}{dR} = \left(\left(\frac{\partial R}{\partial T_s} \right)_T + \left(\frac{\partial R}{\partial T_s} \right)_C + \left(\frac{\partial R}{\partial T_s} \right)_W + \left(\frac{\partial R}{\partial T_s} \right)_L \right)^{-1} \quad (3.3)$$

$$\lambda = (\alpha_T + \alpha_C + \alpha_W + \alpha_L)^{-1}$$

where, for example, α_W is the rate of change of the radiative forcing with respect to the SST, when only the water vapor profile is allowed to change and all other parameters remain fixed. To separate the effects of mean temperature, lapse rate and water vapor, the radiation scheme is run off line for a single atmospheric column using the average profiles from the experiments (e.g. Hansen et al., 1985). The feedback factors are computed for the convective (high cloud) and non-convective (clear sky, low and middle clouds) averages as well as the overall average. An error is associated with using the average profiles instead of the means of the radiative quantities, but it is small here. Non-linear interactions between the feedback factors are not detected with this method. Only the longwave portion of the feedback factors was computed off line, because the shortwave effects, determined by comparing the radiation values of the experiments, are very small for clear skies. There are experiments at 4 different SSTs, so two estimates are made using differences centered at 299 K and 301 K.

Tables 3.2 and 3.3 show the longwave sensitivity parameters estimated by offline calculations using the central SST values of 299 and 301K, respectively. The water

Table 3.2 Clear-sky feedback factors (299 base) obtained from off-line calculations using averaged model results and a radiative transfer model
(units are $W m^{-2} K^{-1}$).

Type of feedback	Convective	All	Non-Convective
water vapor	4.13	4.11	3.75
temperature	-4.03	-4.07	-4.10
lapse rate	-1.87	-1.77	-1.71
total	-1.78	-1.72	-2.06

Table 3.3 Clear-sky feedback factors (301 base) obtained from off-line calculations using averaged model results and a radiative transfer model
(units are $W m^{-2} K^{-1}$).

Type of feedback	Convective	All	Non-Convective
water vapor	4.72	4.56	4.23
temperature	-4.10	-4.13	-4.17
lapse rate	-2.55	-2.43	-2.35
total	-1.93	-2.01	-2.29

vapor feedback is large and positive. It is largest for the total domain and the convective region because the area of the moist convective region increases with SST and the convective region has the highest water vapor content. The smaller feedback in the non-convective region is due to the decrease in the inversion height with increasing SST. The feedback is stronger for the 301 K base SST, because the specific humidity is higher there and the change in specific humidity with SST increases with increasing temperature. The water vapor feedback is smaller than found in TC99, perhaps because the upper troposphere relative humidity and the integrated water vapor

amount are lower in this model. One should expect lower average tropospheric relative humidity when the convection is localized within the model domain (e. g. Held et al. 1993). The upper troposphere relative humidity is lowest in regions of subsidence, and the large domain of these experiments permits regions of persistent subsidence to develop which might not occur in the smaller domain of TC99.

The temperature feedback is found by keeping the specific humidity and lapse rate constant and changing the temperature everywhere by the same amount as the SST. The temperature feedback, which is basically the increase in the Planck function for a uniform temperature change, is approximately canceled by the effect of the water vapor amount acting alone.

The lapse rate feedback is found by using the equilibrium temperature profiles from the perturbation experiments and subtracting the SST perturbation value from the entire temperature profile, then computing the radiative fluxes using the base SST and specific humidity profile. It is negative because the moist adiabatic lapse rate decreases for warmer SST, and slightly larger at the higher base temperature of 301K. The lapse rate effect is slightly stronger in the non-convective region because of the temperature inversion. Because the water vapor and temperature effects nearly cancel, the net clear-sky feedback is negative and approximately equal to the contribution from lapse rate feedback.

Table 3.4 shows the feedback factors obtained from a linear fit of the model experiment results to the imposed SST. The convective region contains high clouds and the non-convective region does not. Values where the explained variance of the linear fit is less than 0.5 are italicized. The first two rows show the total clear-sky feedback factors. The longwave values agree well with the values obtained from the offline radiative transfer calculations shown in Tables 3.2 and 3.3. The clear-sky shortwave feedback factor is small in all regions.

To examine the cloud feedback effect, the net radiation R is separated into its

Table 3.4 Feedback factors obtained from the TOA fluxes of the 12 uniform SST experiments (units are $\text{W m}^{-2} \text{K}^{-1}$).

Type of feedback	Convective	All	Non-Convective
Total clear-sky (LW)	-1.73	-1.68	-1.95
Total clear-sky (SW)	0.09	0.03	0.01
α_c (LW)	3.02	1.79	-0.37
α_c (SW)	-0.14	-0.70	0.15
α_c (net)	2.89	1.09	0.22
Total LW feedback	1.29	0.10	-2.32
Total SW feedback	-0.04	-0.67	0.16
Total net feedback	1.25	-0.56	-2.16

clear and cloudy sky components to calculate the cloud radiative forcing (Charlock and Ramanathan 1985 and others).

$$CRF = R - R_{CS}, \quad (3.4)$$

where R_{CS} represents the net radiative flux at the TOA for the clear-sky regions. I define,

$$\alpha_c = \frac{\Delta CRF}{\Delta T_s}. \quad (3.5)$$

The difference between the clear and cloudy sky TOA fluxes in the model gives the cloud feedback which is summarized in Table 4 for longwave, shortwave and total radiation.

The longwave cloud feedback factor is strongly positive in the convective region because the clear-sky OLR increases and the high cloud OLR decreases slightly with increasing SST. The low clouds in the non-convective region actually have a slightly negative feedback, because the low cloud top height slightly decreases with increasing SST (Fig. 3.12). The shortwave cloud feedback factor is close to zero for the convec-

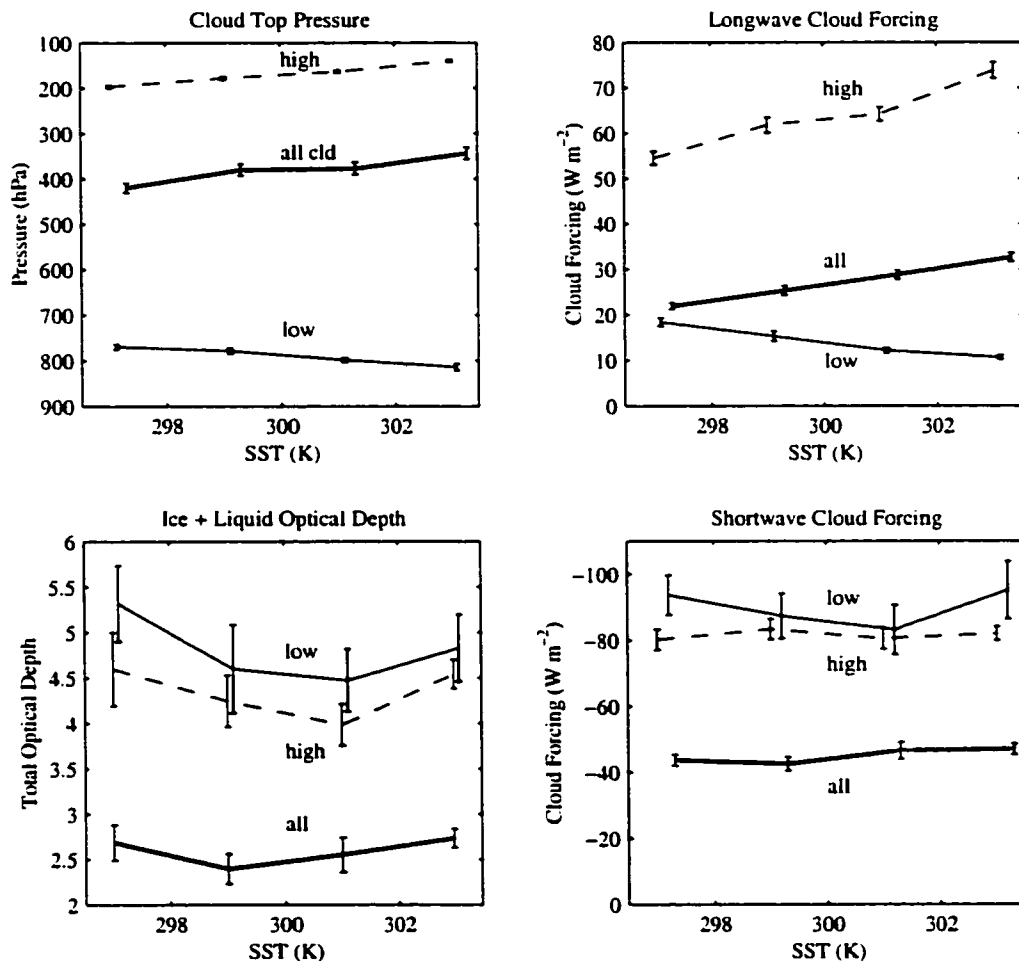


Figure 3.12 Cloud top pressure, cloud visible optical depth, longwave cloud forcing and shortwave cloud forcing for the constant SST experiments. The 95% confidence intervals are noted.

tive and non-convective regions, but negative for the overall average. The cloud optical depth in the two regions does not change significantly with temperature. But because the high cloud area increases with SST, a significant negative shortwave cloud feed-

back occurs for the whole model domain. The high cloud coverage increase also contributes about half of the positive longwave cloud feedback for the whole domain. Clouds produce a net positive feedback overall and in the convective region. The non-convective region has a small negative cloud feedback.

The net clear-sky feedback in these simulations is negative because of the long-wave effects. The cloud feedbacks are positive in the experiments, mostly because the clear-sky OLR increases and the high cloud OLR decreases with increasing SST. For the whole domain, the net feedback is small. For the coarse and high resolution experiments, the TOA radiative fluxes are insensitive to the SST, implying a very sensitive climate.

3.6 Summary and Conclusions

Experiments performed with uniform constant SST, parameterized convection, predicted cloud properties and interactive radiation are able to simulate the observed sensitivity of tropical radiation budget quantities to imposed SST estimated from El Niño events. The sensitivities estimated from the model are almost identical to those inferred from the averages over large regions of the tropics in HM93.

For the thermodynamic variables, the temperature profiles follow an essentially moist adiabatic profile with increasing SST. The relative humidity profile does not show a systematic response to increased SST, though the upper tropospheric relative humidity increases slightly. The altitude of the tropical inversion and the associated boundary layer cloud tops both decrease with increasing SST, as predicted in Larson et al. (1999). The altitude of the cloud ice maximum increases with SST, as is also found in CRMs, and the average rain rate and latent heat flux both increase with SST.

It is important to remember that these simulations depend on cumulus parameterization. No comparisons of the updraft and downdraft mass fluxes are made with CRMs or with observations because those quantities are determined by the cumulus parameterization. The entire domain of the TC99 CRM experiments is smaller than one grid-point in these simulation. These coarse resolution simulations, whose fast

computation is useful for simulations of the entire Pacific, show agreement with the observed sensitivity of clouds to SST, but a colder, drier mean state than other radiative-convective equilibrium CRMs. The mean state may be biased by weaknesses in the model. The increase of the high cloud amount and the size of the convective region with the increase of SST is difficult to validate observationally. The trends are related to the heating in the upper troposphere of the model which is tied to several assumptions made in the parameterizations. A simple two box model predicted a warmer mean temperature with increases in the warm pool size, which is consistent with this model (Larson et al. 1999). In this model, the total integrated cloud water and the convective area based on rain rate are insensitive to the SST, in general agreement with CRMs (TC99, Lau et al. 1994).

The clear-sky feedback factors were computed and the off-line calculation of the temperature, water vapor and lapse rate feedbacks agreed well with the calculations from the actual radiative fluxes. The total clear-sky feedbacks are similar in the convective and non-convective regions and similar to values in other models (TC99, Zhang et al. 1994, Weaver et al. 1994). The water vapor and mean temperature clear-sky feedbacks both have magnitudes close to $4 \text{ W m}^{-2} \text{ K}^{-1}$, and tend to cancel each other out. The lapse rate feedback is about $-2 \text{ W m}^{-2} \text{ K}^{-1}$, similar to the net clear-sky feedback, and is slightly higher than the value found in TC99. Observations (Lau et al. 1997) show a trend in OLR of 1.8 to $2.5 \text{ W m}^{-2} \text{ K}^{-1}$ for subsidence and clear-sky conditions, which is similar to the net clear-sky feedback found in these experiments.

The longwave cloud forcing increases because the high cloud OLR decreases ($1.3 \text{ W m}^{-2} \text{ K}^{-1}$) and the clear-sky OLR increases ($1.7 \text{ W m}^{-2} \text{ K}^{-1}$) with increasing SST. The ice optical depth is increasing with SST and the temperature at the level with the maximum cloud ice concentration is approximately constant, causing the emitting temperature for the high clouds to decrease and produce the small decrease in high cloud OLR as the SST increases. Bony et al. (1997) showed that observed cloud top heights and longwave cloud forcing increase with SST. The increase of longwave cloud forcing with SST is a positive feedback. The visible optical depth of the high

and low clouds do not show significant sensitivities to SST. Observations also show very weak dependence of cloud optical depth on SST for regions without strong vertical forcing (Bony et al. 1997). The high cloud fraction increases with SST, which produces a positive longwave cloud feedback and a negative shortwave cloud feedback. These effects nearly cancel each other because the net high cloud forcing is close to zero. Kiehl (1994) and Hartmann et al. (2001b) focus on the nearly zero net cloud forcing of high clouds, and in chapter 1 the net zero cloud forcing was also shown to weaken the effect of cloud feedback on tropical climate.

The positive cloud feedback and the negative clear-sky feedback are about equal. Together these effects produce a model system in which the TOA radiative fluxes are not very sensitive to the SST, implying a very sensitive climate. The sensitivities calculated in these experiments imply that an external forcing of 1 W m^{-2} would force a SST change of 1.8 K. The uniform SST and lack of energy exchanges with surrounding regions might contribute to the sensitivity of the system. SST gradients, vertical motions, and energy exchanges to the extratropics are not considered here and could affect the sensitivity of tropical climate. Since the model produces responses to SST of clear-sky fluxes and cloud forcing that are similar to observations, I have some confidence in the basic cloud and radiation physics incorporated in the model. In chapter 4 the cloud and water vapor feedbacks are studied in an environment with imposed SST gradients.

Chapter 4: SST Gradients

4.1 Introduction

Convection, clouds and water vapor have the potential to produce large positive or negative feedbacks in the climate system. Feedbacks associated with the dependence of saturation vapor pressure on temperature are strongest in the tropics, where the surface temperature is already high. These feedback processes are coupled in important ways to the large-scale circulation in the tropics, which is, in turn, influenced by the spatial gradients of sea surface temperature (SST) and the distribution of land and sea.

Several different feedback processes are potentially important in the tropics. The dependence of saturation vapor pressure on temperature gives a naturally strong positive feedback (Manabe and Wetherald 1967), which should be particularly strong in the tropics. This feedback is altered by lapse rate feedback in the tropics, because the moist adiabatic lapse rate decreases significantly with temperature in the tropics (e.g. Cess 1975; Knutson and Manabe 1995). The greatest flux of infrared energy in the tropics comes from dry, cloudless regions (Pierrehumbert 1995). If the area of the dry cloudless regions changes with temperature, or the relative humidity changes with temperature, then strong feedbacks might be associated with such changes (Lindzen 1990; Lindzen et al. 2001).

If the albedo of tropical convective clouds is very sensitive to SST in the tropics, then this can produce a strong negative feedback (Ramanathan and Collins 1991). Within the tropics, however, convective cloud albedo is affected both by the absolute value of SST and the gradients of SST (Hartmann and Michelsen 1993). Lau et al. (1994) showed that the convective intensity and associated convective cloud albedo in

a cloud-resolving model were much more sensitive to the imposed mean vertical motion than to the SST. In nature, the mean vertical motion appears to be modulated by the horizontal gradients of SST. In addition, stratocumulus clouds in the tropics are particularly sensitive to SST gradients and may provide an important climate feedback (Miller 1997; Larson et al. 1999). Coupled atmosphere-ocean models indicate that the simulated SST gradients are sensitive to cloud processes (Meehl et al. 2000), so that the cloud properties are determined by mutual interaction between the SST distribution, convection and clouds, and the large-scale circulation. Climate feedback processes may respond differently to changes in mean SST and changes in the gradients of SST in the tropics. In this chapter, the relative roles of mean SST and SST gradients are studied using a set of model experiments with imposed SST distributions with sinusoidal variations.

The effect of imposed SST gradients on tropical convection and clouds has been studied in a variety of atmospheric models. A 2-D cumulus ensemble model (CEM) study by Grabowski et al. (2000) used an imposed sinusoidal SST gradient and studied the effects of cloud-radiative interaction. Bretherton and Sobel (2001, manuscript submitted to *J. Climate*) use quasi-equilibrium theory and the weak temperature gradient approximations to show similar sensitivities to cloud-radiation interaction as Grabowski et al. (2000). Both studies found the addition of cloud-radiation interaction reduces the fraction of the domain where it is raining and covered with deep convection. Bretherton and Sobel (2001, manuscript submitted to *J. Climate*) make the further prediction that the rain area will decrease with increasing SST gradient and the mean atmospheric temperature will increase with increasing SST gradient. Sui et al. (2000, manuscript submitted to *J. Climate*) study a 2-D CEM with a cold pool and a warm pool. The SST difference (δSST) between the pools is varied and the precipitation increases with increasing δSST and the precipitation area decreases. The radiative cooling and the subsidence strength remain constant, but the convective area decreases with increasing δSST in their model. The net change of shortwave radiation is negligi-

ble and the outgoing longwave radiation (OLR) change is due to the water vapor greenhouse effect and the larger longwave effect of cloud forcing (Sui et al. 2000, manuscript submitted to *J. Climate*).

Chapter 3 showed numerical experiments with uniform SSTs had increased high cloud with increasing SST, though the relative humidity profile showed only a weak dependence on SST. The insensitivity of the relative humidity profile to SST was also found in the numerical experiments of Tompkins and Craig (1999). Part one also showed the sensitivity of the radiative fluxes to SST is similar to the sensitivity inferred from observations.

In this chapter, the model of chapter 3 is forced by sinusoidal SST gradients. The resulting large-scale circulations and their effects on the clouds, water vapor and top of the atmosphere (TOA) radiation balances are discussed. Section 2 describes the model and compares it to observations. Section 3 investigates the large-scale circulation. Subsequently, the precipitating area, clouds, and radiation and their sensitivity to mean SST and SST gradients of the model are investigated (sections 4, 5, and 6). Conclusions and discussion are in section 7. This research is will be submitted to the Journal of climate (Larson and Hartmann 2002b).

4.2 Model Description and Validation

The essential physical processes of dynamics, cloud microphysics, convection, radiation and moisture advection are included in the NCAR/PSU mesoscale model (MM5) version 2. The MM5 has been modified as in chapter 3. The Community Climate Model version 3 radiation code has been implemented as well as the shallow cumulus and boundary layer parameterizations based on Grenier and Bretherton (2001), McCaa (2001), McCaa et al. (2001, manuscript submitted to *Mon. Wea. Rev.*), and McCaa and Bretherton (2001, manuscript submitted to *Mon. Wea. Rev.*). The horizontal grid spacing is set to 120 km and the domain is 16 grid-points by 160 grid-

points. The SST is prescribed to vary in the 160 grid-point direction, but it is constant across the 16 grid-point width. The simulations are computed for 90 days and the results reported are from averages of data every 6 hours for days 60 to 90 of the simulation. The data are averaged over the shorter horizontal dimension of the simulations as well, since the SST does not change in that direction.

Equatorial Pacific observations are chosen to validate the model. The Pacific is the largest expanse of equatorial ocean on the planet and normally features a strong east-west temperature gradient along the equator. The model, with equatorial equinox insolation including the diurnal but no annual cycle, is compared to climatologies over the Pacific for the month of September. The average insolation for September is close to the equinox value, and that month has a large SST gradient over the Pacific, producing a strong Walker Circulation.

For comparison with observations, a sinusoidal SST gradient is chosen that approximates the SST distribution in the Equatorial Pacific for September. The SST data are from the Comprehensive Ocean-Atmosphere data set (COADS) climatology (version 1a for years 1980-1995) and are averaged from 5°N - 5°S for 130°E - 230°E and smoothed; the average for September and the annual average are both shown (Fig. 4.1). The doubly periodic model spans a full sine wave, but only part of the domain is compared to observations because the SST distribution of the Pacific does not approximate a full period of a sine function. The range of SSTs used in the model is 3.9°C and the mean is 27.5°C . A narrow range of latitudes (5°N - 5°S) is used for comparison to the model, since the SST does not vary with latitude in the model.

Tropospheric tropical temperatures do not have large horizontal temperature gradients above the boundary layer in the tropics (Sobel et al. 2001). Vertical profiles of temperature for the warmest (5°N - 5°S , 150°E - 170°E) and coldest (5°N - 5°S , 240°E - 260°E) parts of the model and the corresponding regions over the Pacific are shown (Fig. 4.2). Reanalysis data sets incorporate observations and previous results of

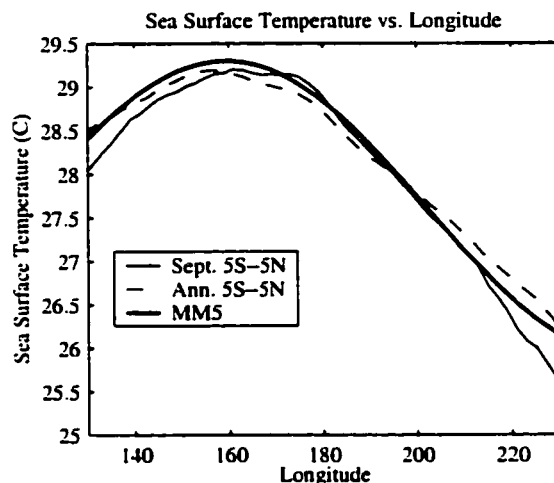


Figure 4.1 SST vs. longitude. The SST are from the COADS data set. The annual averages (dashed) and the September monthly (solid thin) climatology are shown for averaged latitudes 5N-5S. The model SST is denoted with a thick line.

numerical weather prediction. The National Center for Environmental Prediction (NCEP) reanalysis climatology is averaged for the years 1979-1995 and the European Centre for Medium Range Weather Forecasting (ECMWF) reanalysis is averaged for years 1980 - 1989. NCEP and ECMWF reanalysis air temperatures are similar in both regions; the model temperature is cooler in the warm region and the upper troposphere of the cold region. The cold bias of this simulation is similar to the cold bias in the troposphere found in many cloud models when simulating convection over the western Pacific cold pool (Su et. al 1999). Mixing of very dry air from the troposphere to the planetary boundary layer may contribute to a deeper surface boundary layer with colder air temperatures in the warm pool (McCaa et al. 2001, manuscript submitted to *Mon. Wea. Rev.*). The model does not have any land, or advection from land areas that might also act to additionally warm the temperatures. In the cold pool an indication of an inversion appears at about 750 hPa in the model temperature profile that is not found in the ECMWF or NCEP reanalysis. ECMWF and NCEP are long-term climatological means for September and the model is only averaged over 30 days so it is understandable that any inversions in the reanalysis climatology have been smoothed.

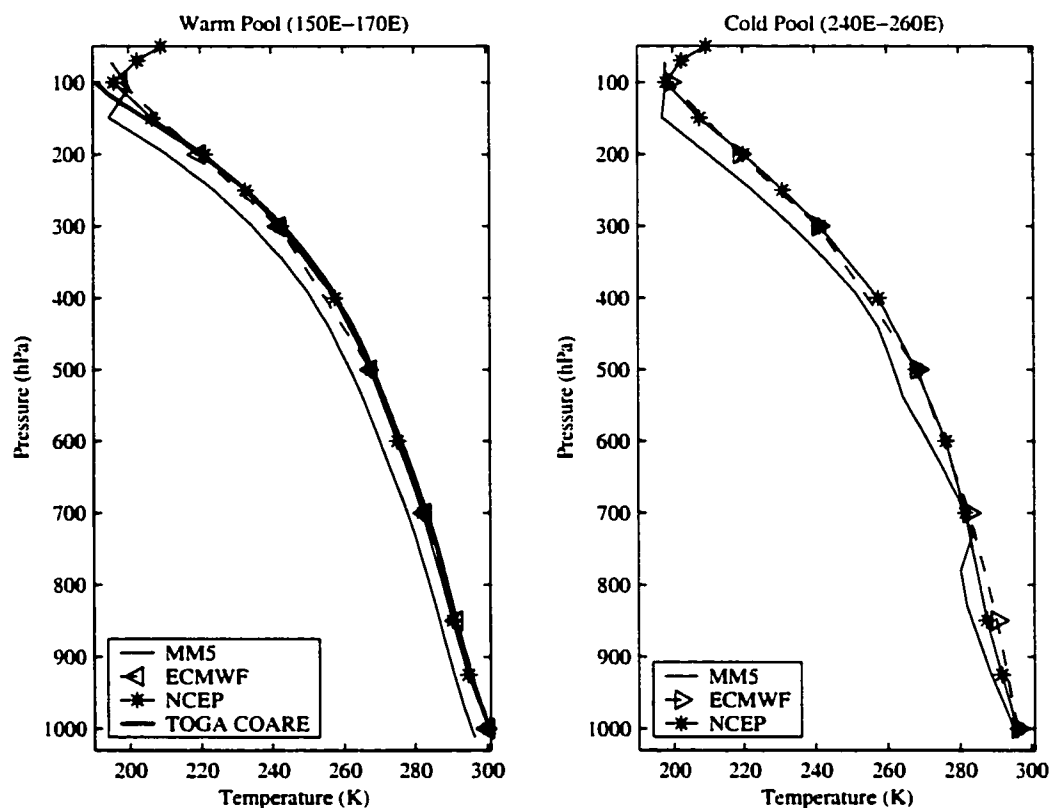


Figure 4.2 Temperature profiles for the warm and cold pools. The warm pool profiles are averaged from 5N-5S and from 150E - 170E. The cold pool profiles are averaged from 5N-5S and 240E - 260 E. The model is denoted with a thin solid line. The ECMWF reanalysis is denoted with a triangle and a dashed line and the NCEP reanalysis is denoted with an asterisk and a solid line.

Soundings over the Eastern Pacific ocean show an inversion at about 800 hPa approximately half of the time (Yin and Albrecht 2000).

Cross sections of relative humidity are shown for ECMWF and NCEP reanalysis September climatologies averaged from 5 °N - 5 °S and the model simulation (Fig. 4.3). NCEP shows a larger variation in upper tropospheric relative humidities than ECMWF, which emphasizes that reanalysis from different weather prediction models are not consistent, especially for simulating the difference between convective and subsidence areas. Relative humidities above 80% cover more area in the model than the reanalysis. The maximum upper tropospheric relative humidities occur at different longitudes: 137 °E for ECMWF, 147 °E for NCEP and 160 °E for the model. The

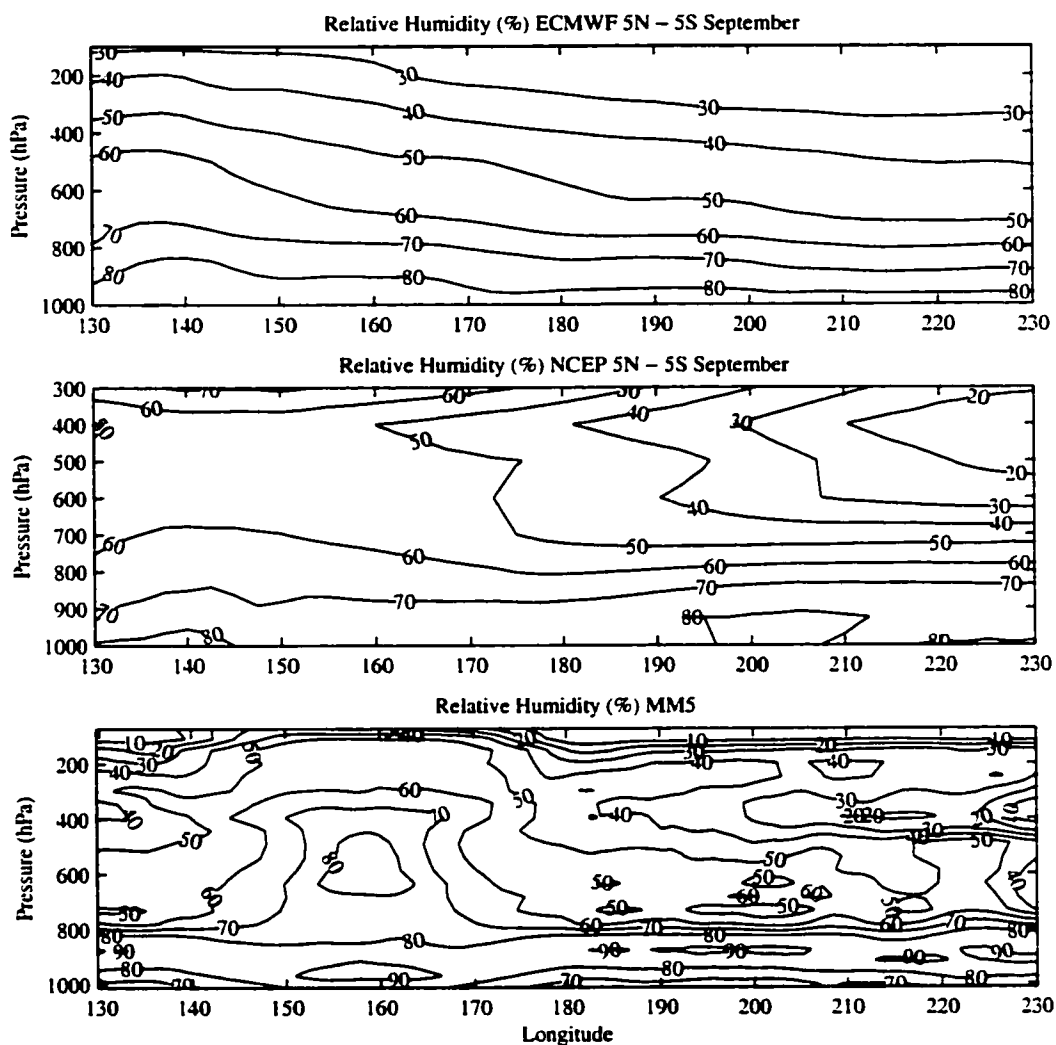


Figure 4.3 Relative humidity cross section vs. longitude for ECMWF and NCEP reanalysis and model data. The cross section is averaged from 5N-5S. The reanalysis is for the September long term mean.

maximum upper tropospheric relative humidity in the model occurs above the maximum SST. The sinusoidal gradient of the model contributes to stronger convergence over the maximum SSTs than elsewhere. The reanalysis maximum of relative humidity may be influenced by the proximity of the maritime continent and warmer SSTs to the west of the warm pool than to the east.

The patterns of rising and sinking motion generally agree between the model and reanalysis data (Fig. 4.4). NCEP reanalysis has stronger vertical motions than

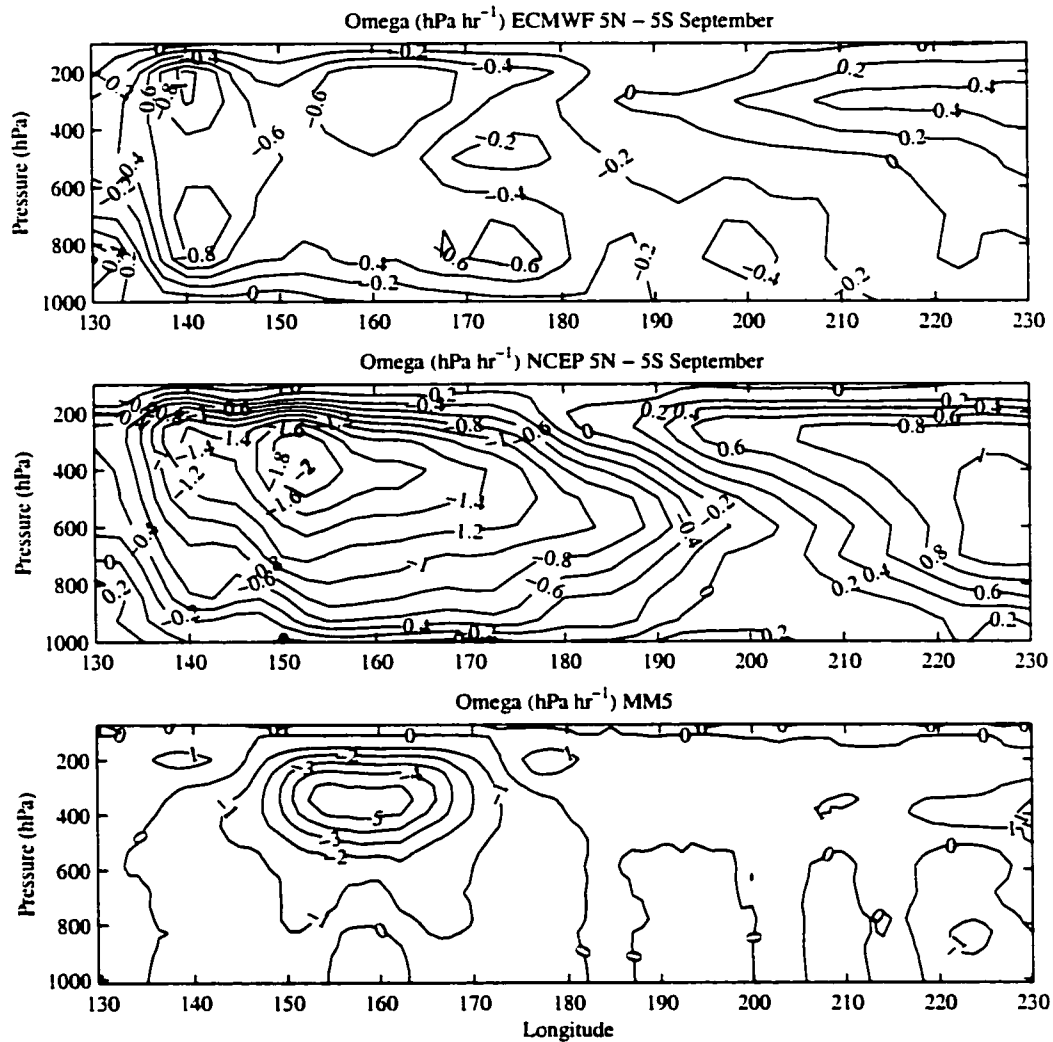


Figure 4.4 Vertical pressure velocity cross section vs. longitude for ECMWF and NCEP reanalysis and model data. The cross section is averaged from 5N-5S. The reanalysis is for the September long term mean. The values for the MM5 have been smoothed in the longitude direction so the zero contour is clearer.

ECMWF. The vertical velocity field is very sensitive to model details in the tropics, and its value is not constrained very well by observations. The fraction of the area covered by the upward and downward motion is similar for all three data sets. The upper troposphere features descending motion and upward vertical motion extends less high as the SST decreases in every case. The vertical velocities are strongest in the model, because the longitudinal SST gradient is the only forcing of the atmosphere and it is constant for the entire simulation. The reanalysis has forcing from the longitudinal

SST gradients, the latitudinal SST gradients, and events like the intraseasonal oscillation, El Niño and dynamical forcing from the extratropics. The model also does not include the effects of Earth's rotation. One should not expect the model employed here to reproduce exactly the observed flow.

The cross section of zonal mass flux highlights the most visible difference between the model and the reanalysis (Fig. 4.5). In the model over the warmest SST there is an

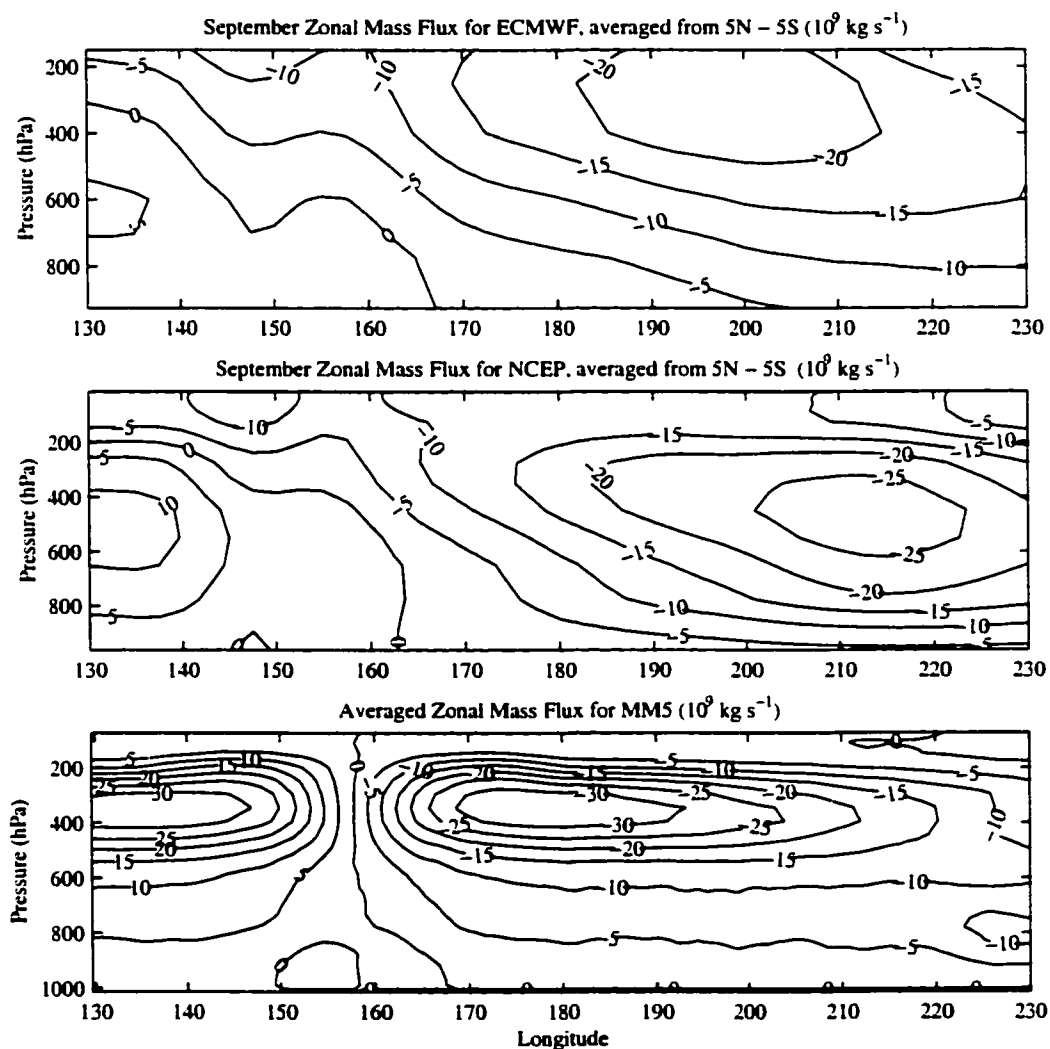


Figure 4.5 Zonal mass flux cross section vs. longitude for ECMWF and NCEP reanalysis and model data. The cross section is averaged from 5N-5S. The reanalysis is for the September long term mean.

upper tropospheric heating, and the resulting circulation in the upper troposphere causes a large zonal mass flux confined to the upper troposphere. The upper tropospheric heating is also associated with high relative humidity, large vertical velocity and large high cloud amount. The zonal mass fluxes for NCEP and ECMWF differ in magnitude and vertical structure. Below 600 hPa the model and the reanalysis agree fairly well.

The cloud properties of the model are compared with the International Satellite Cloud Climatology Project (ISCCP). The ISCCP data set has a 2.5 x 2.5 latitude-longitude grid and data values of cloud percentages, categorized by cloud top height and optical depth (Schiffer and Rossow 1985, Rossow and Schiffer 1999). In the model, radiation variables were stored every 30 minutes. The cloud top was defined to be the pressure where the visible optical depth of the cloud reached 0.1. The amount of cloud cover for each longitude averaged from 5 °N - 5 °S is shown for ISCCP and the model (Fig. 4.6). High clouds are defined to have cloud tops above 440 hPa, and low clouds

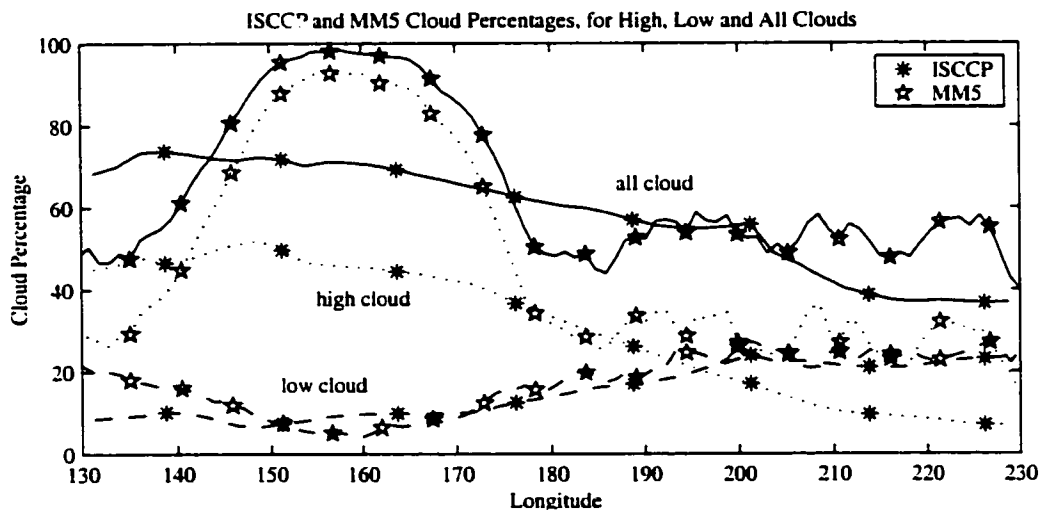


Figure 4.6 Percentage of clouds vs. longitude for ISCCP and model data. The total cloud amount (solid), high cloud amount (dotted) and low cloud amount (dashed) are shown. The annual average is denoted by asterisks', and the model by stars.

are defined to have cloud tops below 680 hPa and the total cloud cover is also shown.

ISCCP data show middle level clouds, but their percentage is about 10% across the entire domain. The percentage of middle clouds in the model is less than 1%. The most cloud cover is in the west due to the SST maxima, and the least is in the east. The model has a region of greater than 80% high cloud coverage over the warmest SSTs that is not seen in ISCCP. The maximum SSTs in the model have convergence in two directions since the model SST distribution is a complete sine wave, unlike the SST distribution in the Pacific. ISCCP also has smaller cloud percentages because the large-scale dynamical forcing in observations is more variable than in the model and the observed SST gradients are two-dimensional, not only longitudinal as in the model. The low cloud amounts for ISCCP and the model are almost identical, and vary similarly with longitude. In summary, the model has a local maximum of high clouds that is not found in ISCCP, but the low cloud amounts agree very well.

The TOA radiation fluxes in the model are compared to observations from the Earth Radiation Budget Experiment (ERBE) data set which are based on satellite measurements over the oceans. In Fig. 4.7, the clear-sky OLR and average sky OLR are shown. The model OLR is much lower than ERBE observations between 152 °E and

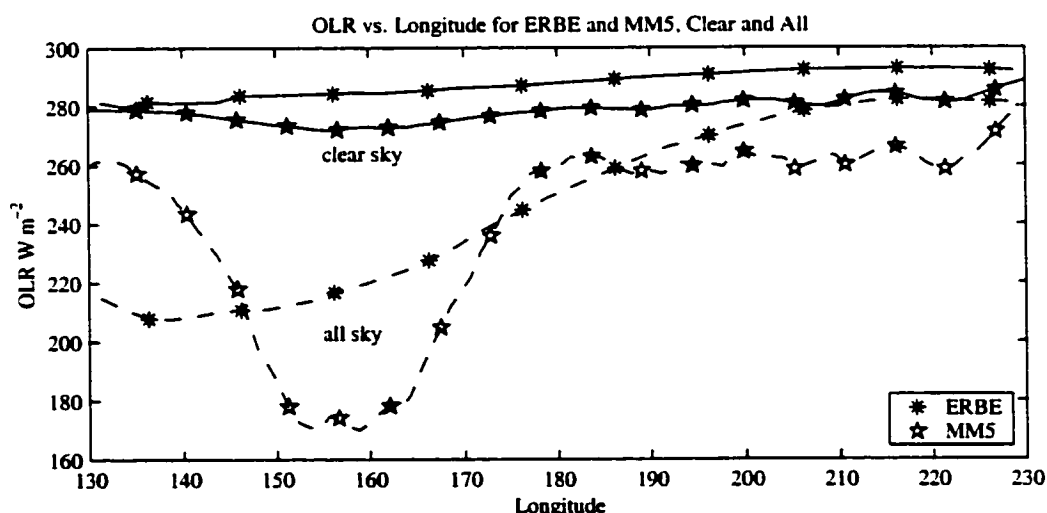


Figure 4.7 OLR vs. Longitude for ERBE and model data. The clear sky (solid) and all sky (dashed) values are shown. The annual average is denoted by asterisks', and the model by stars.

162 °E. This discrepancy arises because the high clouds are concentrated above the warmest SST in the model. The clear-sky OLR has more variation for the ERBE data than for the model. Figure 4.8 shows the net absorbed solar radiation for clear skies and the all sky average. The model has more variations than the ERBE data for the all-

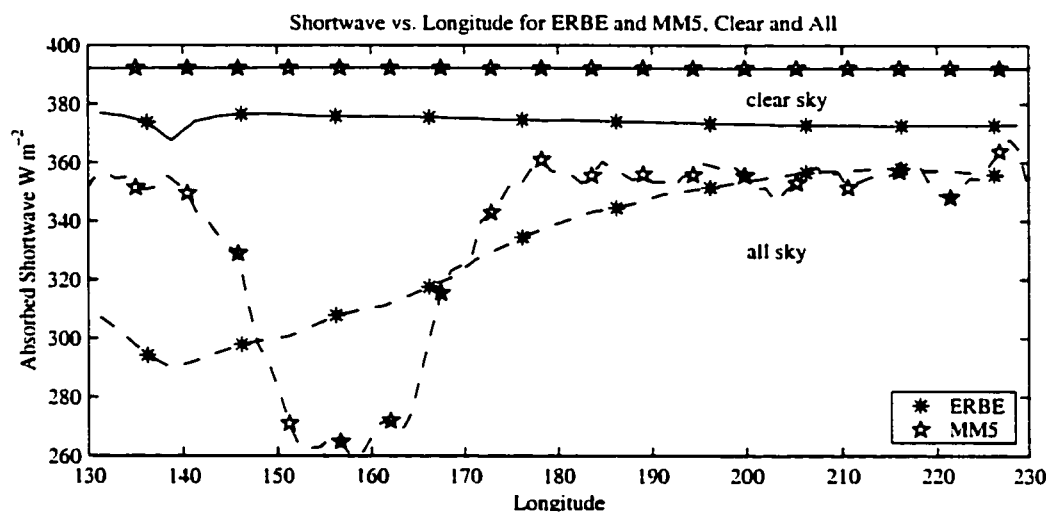


Figure 4.8 The net absorbed solar radiation vs. longitude for ERBE and model data. The clear sky (solid) and all sky (dashed) values are shown. The annual average is denoted by asterisks, and the model by stars.

sky average. The model clear-sky absorbed shortwave is higher and more uniform than the ERBE data. The average ERBE and model values are similar in the east. The region with the model cloud cover maximum has low absorbed shortwave values. The main difference between the model and the cloud and radiation data is that the convective cloud is concentrated over the warmest water in the model and not so in the observations.

The discrepancies between reanalysis data and the model data maybe due to the greater variability of atmospheric forcings experienced in the reanalysis climatologies when compared to the model atmosphere that is forced by a steady SST gradient. Concentrated low level convergence resulting in a large upper tropospheric heating over the maximum SSTs is expected from the sinusoidal SST gradient in the model and is not expected in observations. The increased relative humidities, vertical velocities and

high cloud amounts are all related to the large upper tropospheric heating in the model. The discrepancies with observations would be expected when doing theoretical experiments on a doubly periodic domain without two dimensional SST gradients, changing SST gradients or atmospheric phenomenon like tropical cyclones, intraseasonal oscillation or El Niño. Considering the simplification of the model, the agreement in the values and longitudinal gradients between the model and reanalysis is generally good.

4.3 Large-Scale Circulation, Maximum SST, and SST Gradients

The results of several sinusoidal SST gradient simulations with varying ranges and means provide insights about the role of large-scale circulation. Figure 4.9 shows the SST distribution for five experiments. The experiments are named for the mean SST

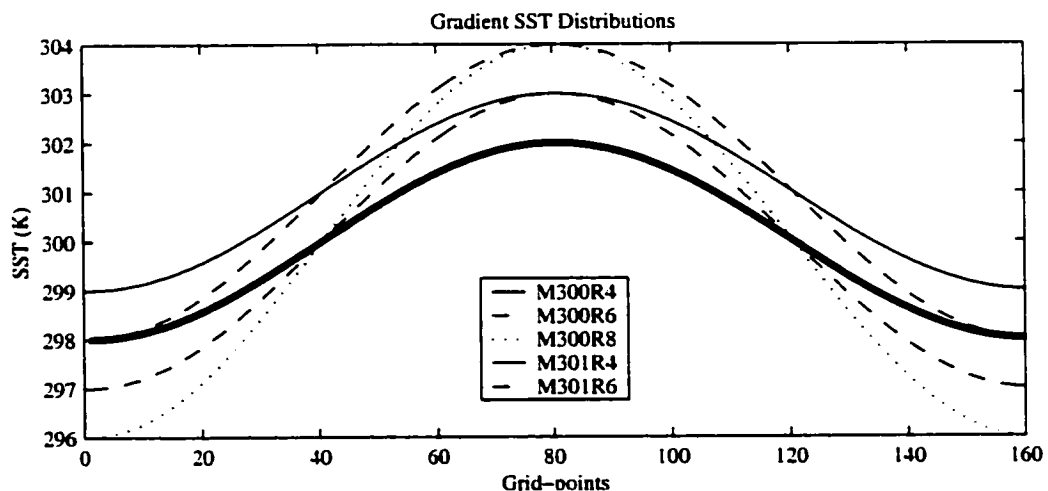


Figure 4.9 SST distributions for five different simulations. M300R4 stands for a mean SST of 300 K and a SST range of 4 K, other abbreviations also show the mean and range of the SST distribution.

and for the range of SSTs in the distribution. Simulation M300R4 has a mean of 300 K and a range of 4 K. Figure 4.10 shows the cloud water variables for simulations with a mean of 300 K and increasing SST ranges of 4, 6 and 8 K. A transition from low stratus clouds in the subsidence region over the coldest SST to high thick ice clouds over the warmest SSTs is evident. The width of the cloud ice 0.001 g kg^{-1} contour narrows as the SST range increases and the extent of the liquid cloud water increases, as shown

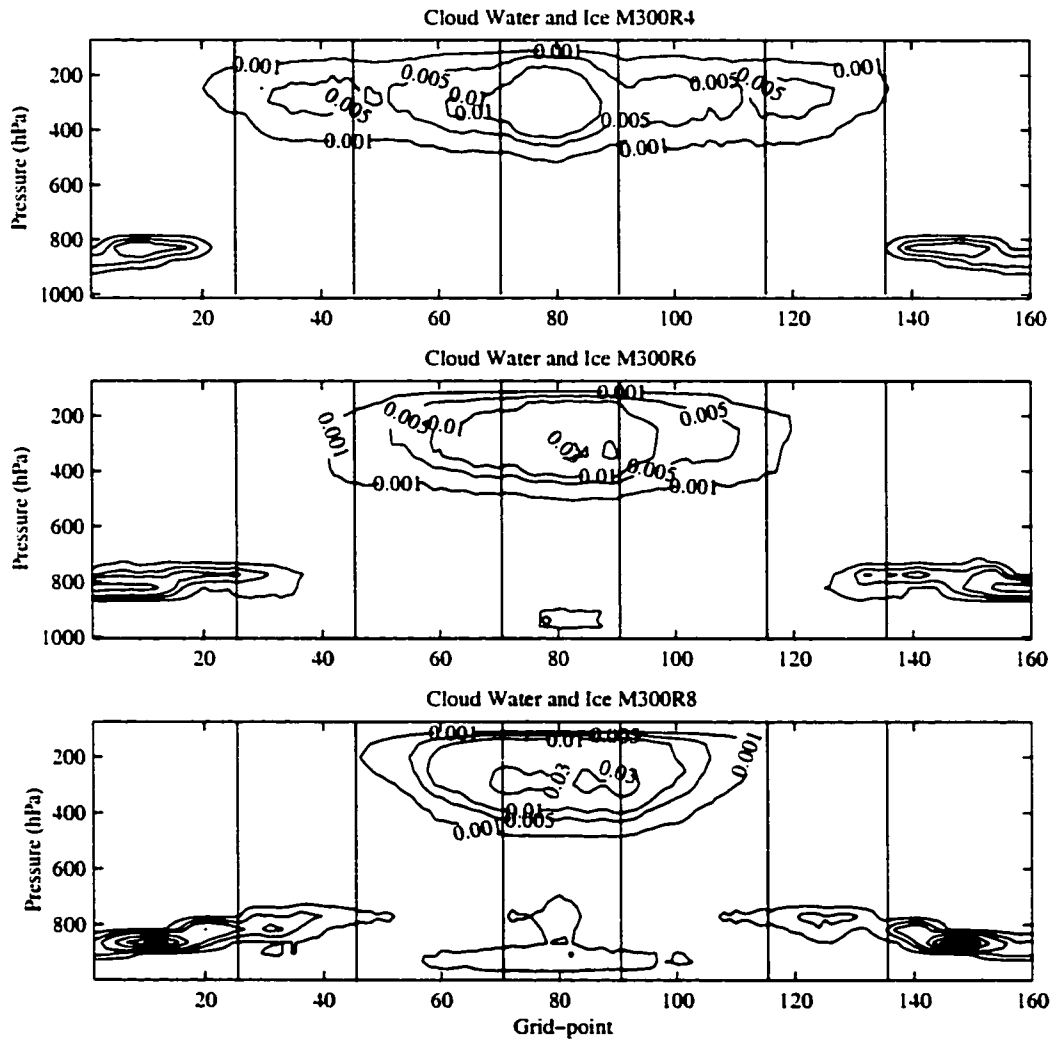


Figure 4.10 Cloud liquid water, and cloud ice for simulations M300R4, M300R6, M300R8. The contours of cloud ice are labeled in g kg^{-1} . The contours of cloud liquid water are 0.01 g kg^{-1} , 0.03 g kg^{-1} , 0.05 g kg^{-1} and every 0.05 g kg^{-1} after that. The contours of cloud ice are 0.001 , 0.005 , 0.01 and at 0.02 intervals until the maximum.

by the 0.01 g kg^{-1} contour. Figure 4.11 shows the temperature tendencies due to dynamical heating (horizontal and vertical advection), moist convection and condensation (diabatic heating), and radiation for the M300R6 simulation. In Figs. 4.10 and 4.11 vertical lines have been drawn to identify regions of subsidence and low clouds, shallow convection, convection and intense deep convection. The boundaries are used

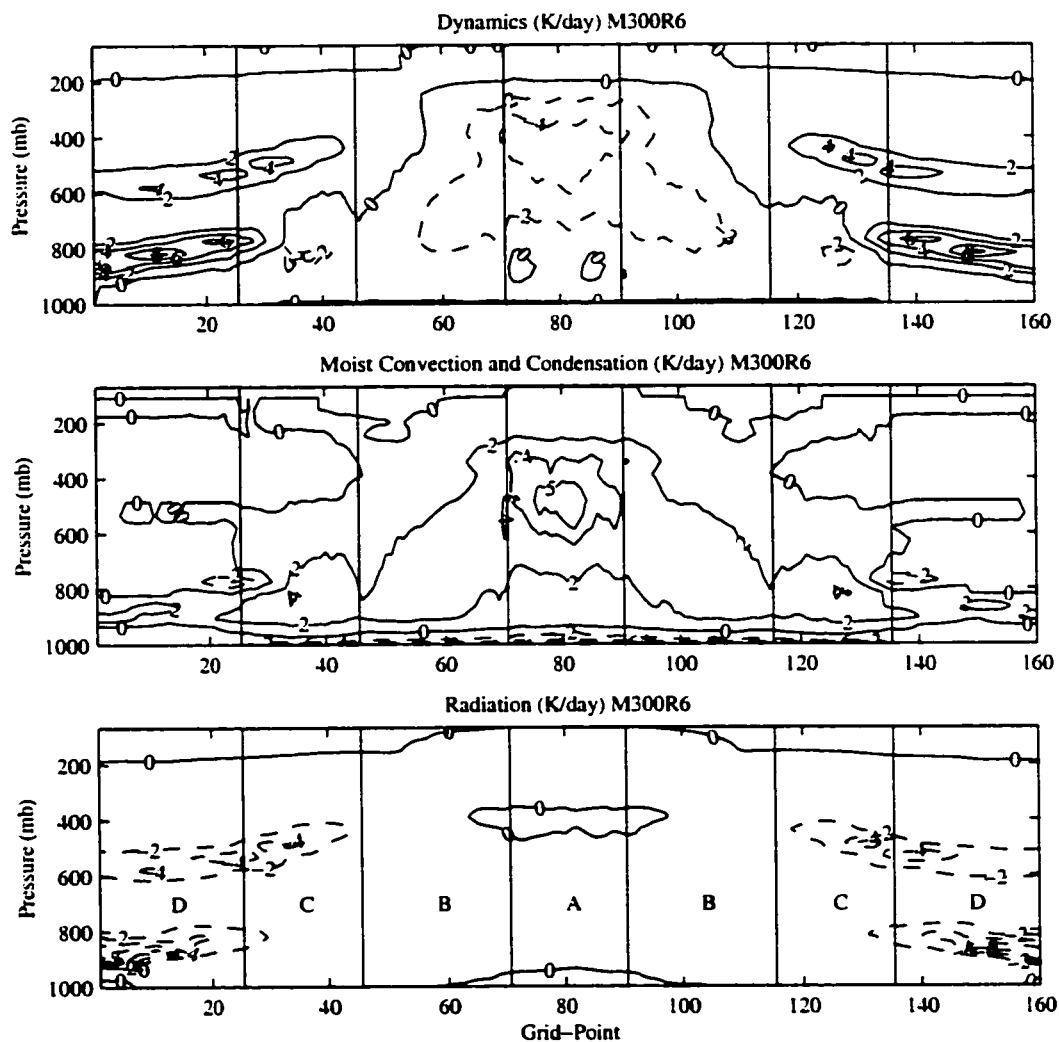


Figure 4.11 The temperature tendency for the dynamics, moist convection and condensation, and radiation in K day^{-1} for the experiment with a SST mean of 300 K and a range of 4K. Negative contours are dashed and positive contours are solid. The contour interval is 2 K day^{-1} . The average for the days 60-90 of the experiments shown. The letters A, B, C, and D represent different regions of the simulation as explained in the text.

to describe regions with different balances between radiation, dynamics and moist convection and condensation, as explained in the next paragraphs.

The intense deep convection region, A, is over the warmest SSTs. This region has high humidity, over 70% high cloud cover, a temperature profile that follows a moist adiabat, and upward motion that peaks at about 2 cm s^{-1} near 300 hPa. The radiative

forcing is small and positive in the upper troposphere and at the ground. The moist convection and condensation peaks at about 400 hPa and is balanced by dynamical cooling forced by rising motion.

The convection region, B, is next to the intense deep convection region. The moist convection and condensation peaks in this region at about 700 hPa and is balanced approximately equally by dynamical cooling and radiative cooling. The temperature profile follows a moist adiabat and the relative humidity is over 50%. The vertical velocity is smaller than in the intense convection region and peaked lower in the atmosphere; it is negative above 250 hPa and positive below that level, never exceeding 0.5 cm s^{-1} . The high cloud covers about half of the region and low clouds cover about 20% of the region.

The shallow convection region, C, is adjacent to the convection region and over SSTs that are on average colder than the mean temperature of the experiment. The temperature profile features a stable layer, which is the trade inversion. The relative humidity is lower above the trade inversion. The vertical velocity is slightly positive near the surface and negative (about 0.5 cm s^{-1}) in the upper troposphere. The level of the zero vertical velocity changes with the SST gradient, and where the velocity is negative, radiative cooling balances subsidence warming. The low cloud amount is about 30% in this region and the high cloud amount decreases as the subsidence increases in this region. Recently, Johnson et al. (1999) have emphasized the role of mid-level convection, cumulus congestus clouds that detrain at the freezing level. The shallow convection and convection regions contain the mid-level convection in these simulations.

The subsidence region, D, is over the coldest SSTs in the experiment. In this region radiative cooling balances subsidence warming. The vertical velocity is negative everywhere below the top three levels of the model. The upper tropospheric relative humidity is only about 15%. The temperature profile has stable layers at the height of the trade inversion and the freezing level.

Figure 4.12 shows the zonal mass flux, rising motion in the center of the domain over the warmest SST and sinking motion over the coldest SSTs for simulation M300R8. The closed circulation in the upper troposphere is also visible in Fig. 4.5 and

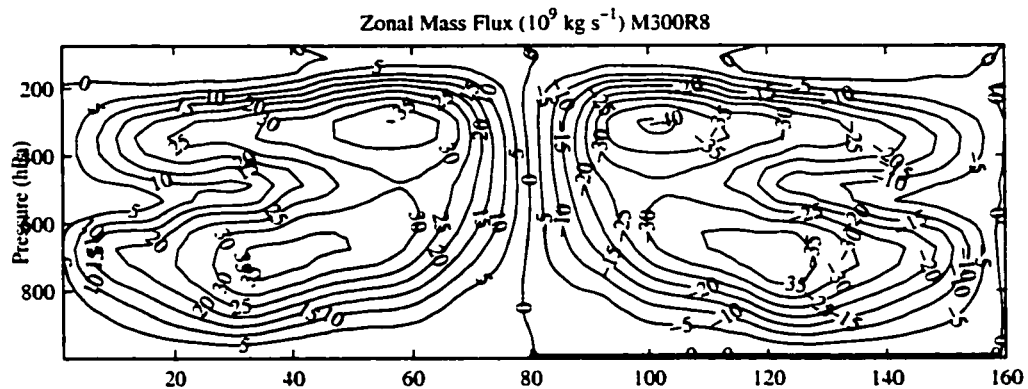


Figure 4.12 Zonal mass flux averaged over latitude for 30 days for the realistic simulation with a mean SST of 300 K and a SST range of 8 K.

there is an additional closed circulation in the lower troposphere near the coldest SSTs. The lower tropospheric circulation becomes more pronounced in the simulations with greater SST ranges and creates a double-celled circulation. Interestingly, Grabowski et al. (2000) also found a double circulation in their CRM simulation forced by a sinusoidal temperature gradient. Their double circulation was attributed to the deviation of their quasi-equilibrium temperature profile from an observed tropical temperature sounding. The temperature profile is established by the radiative heating profile, which features a smaller cooling in the upper troposphere than is found in tropical observations when the radiation interacts with the clouds in the CRM. The radiative cooling profile in these simulations is also smaller than observed in the tropical upper troposphere, contributing to the double-celled circulation. Yano et al. (2002a and 2002b) perform further analysis of the CRM SST gradient simulations, showing the deep mode of the Walker circulation is unstable in their simulations and simple dynamical balances. Above the trade inversion, the vertical velocity given by the balance between radiative cooling and subsidence warming matches the vertical velocities in these simulations, as is shown in Yano et al. (2002b) for CRM simulations and NCEP reanalysis

of the Walker Circulation. Further analysis of the stability and transient dynamics of these simulations will be done in a future study.

The upper circulation is a response to the heating by deep convection, which is strongest between 300 to 500 hPa in the intense deep convection region. The strength of the heating is proportional to the warmest SST. Chapter 3 found convective heating increased with increasing uniform SST which is consistent with increased heating with increased maximum SST. The moist convection and condensation vertical profile in the intense convection region is similar to the profile deduced by Houze (1982) for mature tropical cloud clusters (Fig. 4.11). This profile, with the peak in the upper troposphere, produced a reasonable Walker Circulation in a linear steady-state model (Hartmann et al. 1984). The maximum SST and the maximum zonal mass flux above the freezing level are linearly related, as shown by five representative experiments in Table 4.1. For every degree increase in the maximum SST the upper tropospheric

Table 4.1 The maximum zonal mass flux values in the upper and lower troposphere for 5 experiments with sinusoidal SST gradients.

Name	Maximum SST (K)	Upper Maximum (10^{12} g s^{-1})	Lower Maximum (10^{12} g s^{-1})
M300R4	302	22.3	23.5
M300R6	303	32.4	33.1
M300R8	304	40.4	38.3
M301R4	303	29.3	15.6
M301R6	304	35.6	30.6

zonal mass flux maximum increases 25% of its value for M300R6. The strength of the SST gradient has little effect on the upper zonal mass flux maximum.

In the subsidence region of Fig. 4.11 at about 850 hPa, large negative values of radiative cooling are balanced by subsidence warming, shown by the dynamic temper-

ature tendency. The region of radiative cooling is related to longwave cooling at the top of the stratus clouds, which drives the lower circulation. Nigam (1997) found that lower tropospheric longwave radiative cooling from stratocumulus cloud tops produces a strong dynamical forcing that can be inferred from reanalysis. A maximum of $3\text{-}4\text{ K day}^{-1}$ for the radiative cooling is inferred over the east Pacific, which is comparable to values in the M300R4 experiment. The stratus longwave cooling creates a feedback that produces a rapid development of the coastal southerly surface-wind tendency and stratocumulus clouds from March to May along the equatorial South American coast (Nigam 1997). The maxima of radiative cooling above the stratus clouds produces divergence in the boundary layer, since radiation is balanced primarily by subsidence warming and the maximum subsidence occurs in the layer of maximum cooling. As the range of the SST distribution increases, the radiative cooling above the stratus clouds increases and forces an increase in the lower tropospheric zonal mass flux. The lower tropospheric zonal mass flux increases about 12% of its value in M300R6 for every degree increase in the SST range.

At approximately 550 hPa in the subsidence region there is another region of large radiative cooling and subsidence warming values. A steep gradient in specific humidity produces the large radiative cooling at that level, the temperature profile has a stable layer at that level as well. The lower circulation causes the moisture gradient. Air descending in the upper troposphere rose in the deep convection over the warmest SST and has descended from about 200 mb, decreasing the relative humidity of the parcel. Some air in the lower circulation ascends over the mean SST of the SST distribution and is much more humid because the parcel moves laterally from convection at a much lower altitude in the troposphere. The strong gradient occurs where the dry air from above meets the moister air in the shallow circulation.

Greater longwave radiative cooling forced by the stratus clouds would cause a stronger lower tropospheric circulation. Cloud top longwave cooling is a positive feed-

back on the lower large-scale circulation. Stronger radiative cooling creates more stratus clouds which further strengthens the radiative cooling and would be balanced by stronger subsidence and stronger large-scale circulation. A stronger lower tropospheric circulation may advect more humidity, making the air moister above the boundary layer and reducing the longwave radiative cooling produced by the stratus clouds. Moisture advection by the shallow circulation may act as a negative feedback on the lower tropospheric circulation. A simulation in which the radiative effect of the low cloud was omitted was performed to test how much the radiative cooling above the low clouds contributed to the strength of the large-scale circulation. The lower tropospheric circulation in experiment M300R4 was reduced 13% and the strength of the boundary layer radiative cooling was reduced by eliminating the radiative cooling of low clouds. A stronger humidity gradient developed at the top of the boundary layer that enhanced the cooling, partly compensating for the missing radiative cooling by the boundary layer clouds. The height of the boundary layer and the height of the moisture gradient in the upper troposphere were both decreased in the simulation with radiatively inactive warm clouds. Making the low clouds radiatively inactive decreased the strength of the lower large-scale circulation, showing the cloud top radiative cooling is enhancing the circulation. The atmosphere also compensates by developing a stronger humidity gradient at the inversion and decreasing the height of the inversion and the lower circulation.

For similar SST gradients, when the mean temperature is increased the lower zonal mass flux maximum decreases at a rate of $14\% \text{ K}^{-1}$ for an SST range of 6 K. A decrease in the strength of the large scale circulation when the mean temperature is increased has also been found in other studies (Knutson and Manabe 1995, Larson et al. 1999). Radiative cooling increases slowly with increasing SST, but the atmospheric stability increases because of the non-linear decrease in the moist adiabatic lapse rate for increasing temperatures. The large decrease in lapse rate and increase in dry static

stability forces the strength of the subsidence to decrease in the descending branch of the circulation and causes the large-scale circulation to weaken with increasing SST.

4.4 Rain and Clouds

In these simulations with sinusoidal SST gradients, the largest amounts of rain occur over the warmest SSTs, and the smallest amounts occur over the coldest SSTs. The average precipitation rate for five different experiments is given in Table 4.2. The

Table 4.2The rain rate, rain area and high and low cloud cover amounts for 5 experiments with sinusoidal SST gradients.

Name	Maximum SST (K)	Average Rain Rate (mm/day)	Rain Area (%)	High Cloud Cover (%)	Low Cloud Cover (%)
M300R4	302	3.21	76.9	36.3	27.3
M300R6	303	3.71	70.6	31.3	27.5
M300R8	304	3.87	60.6	32.2	33.4
M301R4	303	3.24	86.3	35.7	22.1
M301R6	304	3.79	70.6	35.4	26.7

rain fraction shows the area of the domain where the average precipitation rate is greater than 1 mm day^{-1} . The mean rain rate increases as the SST range increases and as the mean SST increases. The mean rain rate increases 0.18 mm day^{-1} for a one-degree increase in the SST range because the large-scale circulation (upper and lower) increases with the increasing SST range. The increasing circulation increases the upward mass flux which increases the rain rate. The upper tropospheric circulation also increases with increasing mean temperature. The upper circulation is responsible for the increase of 0.06 mm day^{-1} in mean rain rate for a degree increase in the mean SST. In CRM experiments with a fixed cold pool temperature and increasing warm pool SST, Sui et al. (2000) also found the average rain rate increased because of the increasing strength of the large-scale circulation.

The rain area fraction of the simulations is defined as the percent of grid-points for which the average precipitation is greater than 1 mm day^{-1} . The rain area fraction can be thought of as the convective region of the model. Areas of smaller rain rates are the non-convective region, and often contain low clouds and subsiding motions. The rain area fraction decreases with the strength of the lower tropospheric large-scale circulation (Table 4.2). A stronger lower tropospheric large-scale circulation is associated with increased radiative cooling above stratus clouds which corresponds to increased non-convective area and decreased rain area fraction. The low cloud amount is roughly proportional to the lower tropospheric large-scale circulation and inversely proportional to the rain fraction. The high cloud amount is close to 35% in all the experiments. Figure 4.13a shows the cloud fraction for each longitude for simulations M300R4 and M300R8. The area of the domain covered by at least 20% high clouds

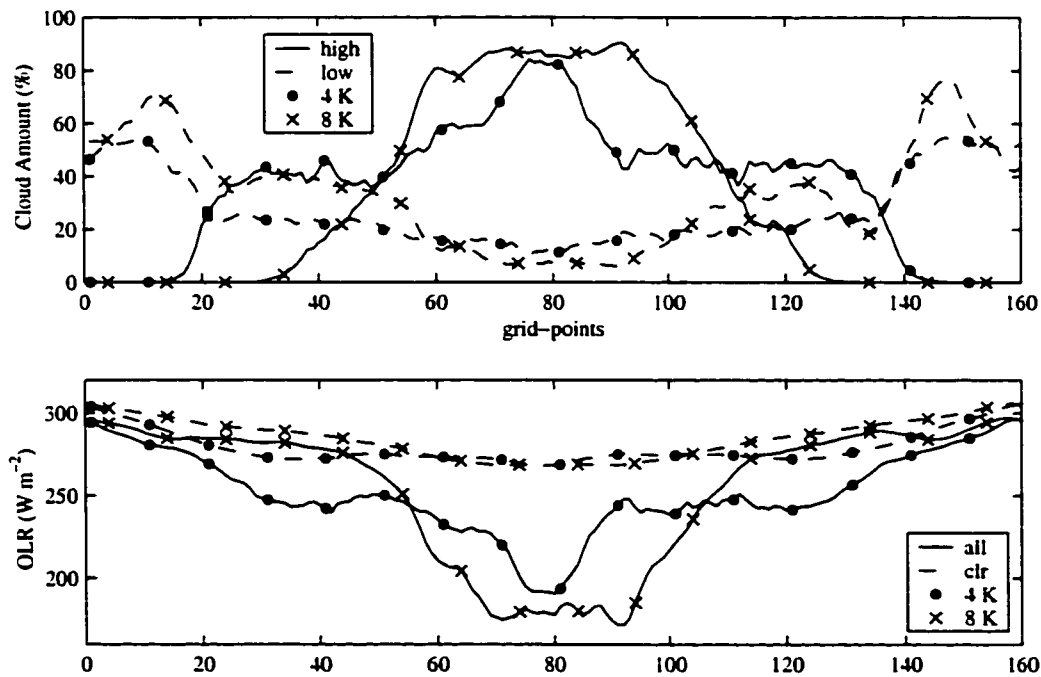


Figure 4.13 The high cloud amount, low cloud amount, average OLR, and clear-sky OLR or each longitudinal grid-point for the third 30 days of the experiment. The numerical experiments with a mean SST of 300 K and a sinusoidal SST gradient of 4K (circle) and 8K (cross) are shown.

decreases, while the area covered by at least 70% high clouds increases as the SST range increases. In other words, the increase of the large-scale circulation acts to concentrate the high clouds in a smaller fraction of the domain. The convective area decreases, and the low cloud amount increases, as the SST range increases.

Sui et al. (2000) found the rain area decreased as the difference between the warm and cold pool temperatures (δSST) increased in their CEM experiments. They further diagnosed that the circulation increased because of the increased SST range. The strength of the radiative cooling in the subsidence areas limited the strength of the subsidence, so in the experiment with the biggest δSST , the area of the subsidence region increased. This expansion of the subsidence region also caused the fraction of the domain that was raining to decrease and the narrower convective area contained stronger vertical motions. The fraction of the domain in their experiments that was raining was always less than 50%, because their SST distribution features a discontinuous temperature change from a warm pool (that covers 31% of the domain) to a cold pool. The raining fraction is always more than 50% in our simulations because the sinusoidal SST gradient creates a gradual transition from deep convection to a trade cumulus regime that more effectively widens the rain area.

4.5 Radiation

The average outgoing longwave radiation (OLR) is not sensitive to the SST distribution, in these simulations, and the net absorbed shortwave radiation (SWI) is very sensitive. Changing the SST gradient and mean SST does not strongly affect the average outgoing longwave radiation, while a degree increase in the SST gradient decreases the SWI approximately -5.6 W m^{-2} (Table 4.3). The average optical depth of clouds in the experiment increases with SST gradient and, generally, the total cloud amount increases with increasing SST gradient. The decrease in SWI is matched by an increase in the lower tropospheric large-scale circulation. An increase in the large-scale circulation corresponds to stronger rising motion which creates more cloud water

Table 4.3 Radiation quantities at the top of the atmosphere averaged over latitude and for 30 days for 5 experiments with sinusoidal SST gradients. The quantities are OLR, SWI, shortwave cloud forcing, longwave cloud forcing, the blackbody emission for the given SST distribution, and the clear-sky greenhouse forcing ($\sigma T^4 - \text{OLR}_{\text{clr}}$).

Name	SWI (W m^{-2})	SW CF (W m^{-2})	OLR (W m^{-2})	OLR clr-sky	LW CF (W m^{-2})	σT^4 (W m^{-2})	G_{clr} (W m^{-2})
M300R4	332.7	-59.4	251.3	279.1	27.8	459.3	180.3
M300R6	324.7	-67.6	256.7	283.3	26.6	459.4	176.1
M300R8	308.4	-84.0	254.0	285.0	31.0	459.5	174.6
M301R4	341.5	-50.8	253.3	281.4	28.1	465.5	184.1
M301R6	324.0	-68.5	255.3	286.0	30.7	465.6	179.5

and higher surface wind speeds, which increase the evaporation at the surface. These effects are consistent with increased water content in the atmosphere, increased shortwave cloud forcing and decreased SWI. The shortwave cloud forcing and the strength of the lower large-scale circulation are both related to the radiative effect of the stratus clouds in the subsidence region.

The domain-averaged OLR is very similar for all the experiments. The cloud top temperature where the visible optical depth reaches 0.1 is approximately constant in all the simulations (Hartmann and Larson 2002). Figure 4.13b shows the OLR distribution for experiments M300R4 and M300R8. The average OLR is 2.7 W m^{-2} higher in simulation M300R8. The average clear-sky OLR is 5.9 W m^{-2} higher in simulation M300R8 which has the greater maximum SST. The temperature profile in the gradient experiments above the boundary layer is similar to the moist adiabatic profile in the intense deep convection region over the warmest SSTs, causing the clear-sky OLR to increase as the maximum SST increases. The clear-sky greenhouse effect is defined as blackbody radiation at the SST minus clear-sky OLR, and it decreases with increasing SST gradient. Changes in the SST gradient do not strongly affect the average surface

blackbody emission, but the clear-sky OLR increases with SST gradient because the maximum SST increases the air temperature everywhere (Table 4.3).

The clear-sky greenhouse effect is greatest in regions of high upper-tropospheric humidity, which have been shown to occur near deep convection (Udelhofen and Hartmann 1995; Salathe and Hartmann 1997). If the SST gradient is held constant and the mean SST is increased, the longwave cloud forcing increases about $2 \text{ W m}^{-2} \text{ K}^{-1}$ and the clear-sky greenhouse effect increases about $3.5 \text{ W m}^{-2} \text{ K}^{-1}$. The sum of these two positive feedbacks approximately cancel the longwave emission increase associated with the imposed temperature increase.

4.6 Conclusions

This research demonstrates the important effects of the SST gradients and large-scale circulation on tropical climate sensitivities. Simulations with imposed fixed SST gradients are similar to averaged observations over the Pacific, when the discrepancies of large-scale dynamical forcing and constant full period sinusoidal SST gradients are taken into account. The simulations with sinusoidal SST gradient give distinct upper and lower zonal mean circulations in the troposphere. The upper circulation is sensitive to the heating from deep convection over the warmest SST and the lower circulation is sensitive to radiative cooling produced by stratus clouds.

Stronger SST gradients are associated with a stronger lower and upper tropospheric large-scale circulation, a smaller extent of rain area, and larger area coverage by low clouds. Other studies (Bretherton and Sobel 2002 and Sui et. al 2002) also find that the fraction of the domain within which rain is occurring decreases with increased SST gradient.

Increasing the mean SST decreases the strength of the lower tropospheric large-scale circulation, which increases the convective area and decreases the subsidence area of the simulation. In a coupled GCM with doubled carbon dioxide, Knutson and

Manabe (1995) found an increase in Pacific SST. In the warm pool region they found precipitation enhanced by 15%, but a decrease in the strength of the ascending vertical motion. Those results were explained as a consequence of the moist adiabatic lapse rate decrease with increasing SST, which is also consistent with these fixed SST gradient experiments.

The absorbed shortwave radiation is found to be extremely sensitive to the SST gradient. The stronger lower tropospheric large-scale circulation produces a higher water content in the high and low clouds, increasing the absolute magnitude of the shortwave cloud forcing. The shortwave effect is larger than the small changes in the OLR, and leads to a decrease in net TOA radiation with increasing SST gradient.

Increasing the mean SST creates a positive feedback in these simulations because of the decrease in the lower tropospheric large-scale circulation and the simultaneous decrease in cloud optical depth. As the mean SST increases, low clouds cover a smaller area in the smaller subsidence region, so that the net negative cloud forcing of the low clouds is reduced, producing a net positive feedback. The increased SST decreases the high cloud OLR value and increases the water vapor amount, both of which are positive feedbacks. These effects are offset by the increase in longwave emission with increasing temperatures, but the positive feedbacks are larger.

The atmospheric large-scale circulation is responsible for the organization of tropical convection, clouds, rain, and relative humidity. The re-organization of those quantities can have strong feedbacks on the tropical climate. Increasing the mean SST decreases the strength of the lower large-scale circulation, while increasing the spatial gradients of SST produces increases in the large-scale circulation. Increasing strength of the circulation produces a reduction in the radiation balance in the current model, primarily through increased cloud shortwave forcing. The large-scale circulation causes the greatest change in the net absorbed shortwave radiation, a 25% increase in the lower maximum zonal mass flux of M300R4 leads to a 7.4 W m^{-2} decrease in the

net absorbed shortwave radiation. A 0.6 K increase in the SST gradient may be able to offset a 1 degree increase in the mean SST. The response of SST gradients and the accompanying changes in large-scale circulation can be responsible for significant climate feedbacks. The effect of the large scale circulation on the cloud optical depth is very large according to these simulations and may play an important role in tropical climate sensitivities.

Our understanding of the tropical climate will benefit from applying the results of these simulations to observations. ENSO (El Niño/Southern Oscillation) produces periods where the east-west SST gradient across the Pacific is decreased and the Pacific mean SST is increased. Both SST tendencies are associated with reduced short-wave cloud forcing, according to these results. Comparing these results to cloud observations associated with ENSO can illuminate the robustness of increasing shortwave cloud forcing with increasing large-scale circulation.

Chapter 5: Conclusions

The physical mechanisms that affect the tropical sea surface temperature (SST) are investigated using a two box model and a mesoscale model with fixed uniform and sinusoidal SST gradients. Emphasis is placed on the large-scale circulation containing rising motion in regions with high humidity and high clouds and subsidence in regions with low upper tropospheric humidity, a trade inversion and low clouds.

The humidity above the inversion in the subsiding region increases rapidly with temperature, but this has less effect on the climate sensitivity than expected, because the inversion lowers as the humidity above the inversion is increased. Some of the increased greenhouse effect of the free troposphere can be offset by decreased greenhouse effect of the boundary layer. This is found in the two box model and using fixed uniform SSTs in the mesoscale model.

Increasing the area of the warm, convective region increases the SSTs, because of the greenhouse effect of the greater upper tropospheric water vapor in the convective region in the two box model. With fixed uniform SSTs in the mesoscale model the high cloud areal coverage and convective area increase with increasing SST. Increasing the mean SST increases the convective area when SST gradients are included in the mesoscale model as well.

The circulation strength is constrained by radiative cooling in the cold pool. The strength of the circulation decreases with increasing convective area, because the increase in dry static stability overwhelms the increase in cooling rate in the two box model and the mesoscale model with SST gradients.

Although they have strong individual effects on longwave and shortwave radiation, high clouds in the convective region do not affect the tropical SSTs strongly, because their net radiative forcing at the top of the atmosphere is small. The high cloud OLR decreases with increasing SST because the strength of the convection increases with temperature and this causes a slight positive feedback on the climate.

Low clouds in the subsidence region have a strong cooling affect on the tropical SST, because they strongly reduce net radiative heating at the top of the atmosphere. A negative feedback is produced if the low clouds are predicted from the observed relationship between stratus cloud amount and lower tropospheric stability in the two box model.

For simulations with uniform SST and zero mean vertical motion, the sensitivities of the top of the atmosphere radiative quantities to SST are similar to observations comparing La Niña and El Niño SSTs and radiative quantities when averaged over an area including the ascending and descending branches of the tropical large-scale circulation. These uniform SST simulations also show the clear-sky temperature and water vapor feedbacks are of about equal magnitude in opposite directions, and the lapse rate feedback is negative with a magnitude of approximately $2 \text{ W m}^{-2} \text{ K}^{-1}$.

The responses of the large-scale circulation, clouds and water vapor to an imposed sea surface temperature (SST) gradient compare reasonably to averaged observations over the Pacific, considering the simplifications applied to the mesoscale model. The mesoscale model responses to sinusoidal SST patterns have distinct circulations in the upper and lower troposphere. The upper circulation is sensitive to the heating from deep convection over the warmest SST. Stronger SST gradients are associated with stronger longwave cooling above stratus clouds in the subsidence region, stronger lower tropospheric large-scale circulation, a reduction of the rain area, and larger area coverage of low clouds. A similar SST gradient with a warmer mean temperature pro-

duces an atmospheric stability increase, slightly weaker lower tropospheric circulation, slightly larger rain area and slightly reduced low cloud coverage.

The outgoing longwave radiation (OLR) is not sensitive to the mean SST or the range of the imposed sinusoidal SST gradient in the mesoscale model. The positive feedbacks of water vapor and decreasing high cloud OLR compensate for the increase in longwave emission with increasing mean temperature in these simulations. As the SST gradient is increased keeping the mean SST constant, the positive high cloud feedback is still active and the air temperature increases in proportion to the maximum SST, increasing the clear-sky OLR value and keeping the average OLR constant.

The net absorbed shortwave radiation (SWI) is found to be extremely sensitive to the SST gradient. The stronger lower tropospheric large-scale circulation produces a higher water content in the high and low clouds, increasing the absolute magnitude of the shortwave cloud forcing. A 25% increase in the maximum zonal mass flux of the lower circulation of the 300K mean, 4K SST range simulation could lead to a 7.4 W m^{-2} decrease in SWI. Increasing the mean SST creates a positive feedback in the mesoscale model because of the decrease in the lower tropospheric large-scale circulation and the resultant decrease in cloud optical depth.

Bibliography

- Albrecht, B. A., 1981: Parameterization of trade-cumulus cloud amount. *J. Atmos. Sci.*, **38**, 97-105.
- Albright, M. D., E. E. Recker, R. J. Reed, and R. Dang, 1985: The Diurnal Variation of Deep Convection and Inferred Precipitation in the Central Tropical Pacific during January-February 1979. *Mon. Wea. Rev.*, **113**, 1663-1680.
- Betts, Alan K., 1985: Mixing Line Analysis of Clouds and Cloudy Boundary Layers. *J. Atmos. Sci.*, **42**, 2751-2763.
- Betts, A. K., and B. A. Albrecht, 1987: Conserved variable analysis of the convective boundary layer thermodynamic structure over the tropical oceans. *J. Atmos. Sci.*, **44**, 83-99.
- Betts, A. K., and W. Ridgway, 1988: Coupling of the Radiative, Convective, and Surface Fluxes over the Equatorial Pacific. *J. Atmos. Sci.*, **45**, 522-546.
- Betts, A. K., and W. Ridgway, 1989: Climatic Equilibrium of the Atmospheric Convective Boundary Layer over a Tropical Ocean. *J. Atmos. Sci.*, **46**, 2621-2641.
- Bony, S. K.-M. Lau and Y. C. Sud, 1997: Sea Surface Temperature and Large-Scale Circulation Influences on Tropical Greenhouse Effect and Cloud Radiative Forcing. *J. Climate*, **10**, 2055-2077.
- Bretherton, C. S., and A. H. Sobel, 2001: A simple model of a convectively-coupled Walker circulation using the weak temperature gradient approximation. *J. Climate*, submitted 11/01.
- Bretherton, C. S., E. Klinker, A. K. Betts, J. A. Coakley, 1995: Comparison of ceilometer, satellite, and synoptic measurements of boundary-layer cloudiness and

- the ECMWF diagnostic cloud parameterization scheme during ASTEX. *J. Atmos. Sci.*, **52**, 2736-2751.
- Brown, Randy G. and Chidong Zhang, 1997: Variability of Midtropospheric Moisture and Its Effect on Cloud-Top Height Distribution during TOGA COARE. *J. Atmos. Sci.*, **54**, 2760-2774.
- Cess, R. D., 1975: Global Climate Change: An investigation of atmospheric feedback mechanisms. *Tellus* **27**(3): 193-198.
- Cess, R. D., and Coauthors, 1996: Cloud feedback in atmospheric general circulation models: An update. *J. Geophys. Res.*, **101**, 12 791- 12 794.
- Charlock, T. P. and V. Ramanathan, 1985: The albedo field and cloud radiative forcing produced by a general circulation model with internally generated cloud optics. *J. Atmos. Sci.*, **42**, 1408-1429.
- Chen, S. S., and R. A. Houze Jr., 1997: Diurnal variation and life-cycle of deep convective systems over the tropical Pacific warm pool. *Quart. J. Roy. Meteor. Soc.*, **123**, 357-388.
- Clement, Amy C. and Richard Seager, 1999: Climate and the tropical oceans. *J. Climate*, **12**, 3383-3401.
- Clement, Amy C. and Richard Seager, Mark A. Cane, and Stephen E. Zebiak, 1996: An Ocean Dynamical Thermostat. *J. Climate*, **9**, 2190-2196.
- Dickinson, R. E., V. Meleshko, D. Randall, E. Sarachik, P Silva-Dias, and A. Slingo, 1996: Climate Processes. *Climate Change 1995: The Science of Climate Change*, J. T. Houghton, L.G. Meira Filho, B. A. Callander, N. Harris, A. Kattenberg, and K. Maskell, Eds., Cambridge University Press, 193-227.
- Dudhia, J., 1993: A nonhydrostatic version of the Penn. State/ NCAR mesoscale model: Validation tests and simulations of an Atlantic cyclone and cold front. *Mon. Wea. Rev.*, **121**, 1493-1513.
- Duvel, J. P., and F. M. Bréon, 1991: The clear-sky greenhouse effect sensitivity to a sea surface temperature change. *J. Climate*, **4**, 1162-1169.

- Fairall, C. W., E. F. Bradley, D. P. Rogers, J. B. Edson, and G. S. Young, 1996: Bulk parameterization of air-sea fluxes for Tropical Ocean-Global Atmosphere Coupled-Ocean Atmosphere Response Experiment. *J. Geophys. Res.*, **101**, 3747-3764.
- Frigo, M. and S. G. Johnson, 1999 FFTW User's Manual, MIT.
- Fu, Q., S. K. Krueger, and K. N. Liou, 1995: Interactions of radiation and convection in simulated tropical cloud clusters. *J. Atmos. Sci.*, **52**, 1310-1328.
- Fu, Rong, Anthony D. Del Genio, William B. Rossow, and W. Timothy Liu, 1992: Cirrus-cloud thermostat for tropical sea surface temperatures tested using satellite data. *Nature*, **358**, 394-397.
- Grabowski, W. W., M. W. Moncrieff, and J. T. Kiehl, 1996: Long-term behaviour of precipitating tropical cloud systems: A numerical study. *Quart. J. Roy. Meteor. Soc.*, **122**, 1019-1042.
- Grabowski, W. W., J.-I. Yano and, M. W. Moncrieff, 2000: Cloud resolving modeling of tropical circulations driven by large-scale SST gradients. *J. Atmos. Sci.*, **57**, 2022-2039.
- Grell, G. A., J. Dudhia and D. R. Stauffer, 1994: A description of the fifth-generation Penn. State/NCAR Mesoscale Model (MM5). NCAR Tech Note, NCAR/TN-398 + STR, 138 pp.
- Grenier, H. and C. S. Bretherton, 2001: A moist PBL parameterization for large-scale models and its application to subtropical cloud-topped marine boundary layers. *Mon. Wea. Rev.*, **129**, 357-377.
- Hansen, J., and G. Russell, A. Lacis, I. Fung, D. Rind, and P. Stone, 1985: Climate Response Times: Dependence on Climate Sensitivity and Ocean Mixing. *Science*, **229**, 857-859.
- Harrison, E. F., P. Minnis, B. R. Barkstrom, V. Ramanathan, R. D. Cess and G. G. Gibson, 1990: Seasonal variation of cloud radiative forcing derived from the Earth Radiation Budget Experiment. *J. Geophys. Res.*, **95**, 18,687-18,703.

- Hartmann, D. L., 1994: Global Physical Climatology. Academic Press, San Diego, 411.
- Hartmann, D.L., and E. Recker, 1986: On the diurnal variation of outgoing longwave radiation in the tropics, *Journal of Climate and Applied Meteorology*, **25**, 800-812.
- Hartmann, D. L. and M. L. Michelsen, 1993: Large-scale effects on the regulation of tropical sea surface temperatures. *J. Climate*, **6**, 2049-2062.
- Hartmann, D. L., H. H. Hendon and R. A. Houze, Jr., 1984: Some implications of the mesoscale circulations in cloud clusters for large-scale dynamics and climate. *J. Atmos. Sci.*, **41**, 113-121.
- Hartmann, Dennis L., James R. Holton, and Qiang Fu: 2001a: The Heat Balance of the Tropical Tropopause, Cirrus and Stratospheric Dehydration., *Geophys. Res. Lett.*, **28**, 1969-1972.
- Hartmann, D. L., L. A. Moy and Q. Fu, 2001b: Tropical Convection and the Energy Balance at the Top of the Atmosphere. submitted to *J. Clim.* 2001.
- Hartmann, D. L., M. E. Ockert-Bell and M. L. Michelsen, 1992: The effect of cloud type on Earth's energy balance: Global Analysis. *J. Climate*, **5**, 1281-1304.
- Held, I. M., R. S. Hemler, and V. Ramaswamy, 1993: Radiative-convective equilibrium with explicit two-dimensional moist convection. *J. Atmos. Sci.*, **50**, 3909-3927.
- Held, Isaac M. and Arthur Y. Hou, 1980: Nonlinear axially symmetric circulations in a nearly inviscid atmosphere. *J. Atmos. Sci.*, **37**, 515-533.
- Houze, R. A., Jr., 1982: Cloud clusters and large-scale vertical motions in the tropics. *J. Meteor. Soc. Japan*, **60**, 396-410.
- Ikawa, M. and Sito, K., 1991: Description of a nonhydrostatic model developed at the forecast research department of the MRI. Tech. Report of MRI, 28.
- Inamdar, A. K. and V. Ramanathan, 1994: Physics of greenhouse effect and convection in warm oceans. *J. Climate*, **7**, 715-731.

- Janowiak, J. E., Phillip A. Arkin and M. Morrissey, 1994: An Examination of the Diurnal Cycle in Oceanic Tropical Rainfall Using Satellite and In Situ Data. *Mon. Wea. Rev.*, **122**, 2296-2311.
- Johnson, R. H., T. M. Rickenbach, S. A. Rutledge, P. E. Ciesielski, and W. H. Schubert, 1999: Trimodal Characteristics of Tropical Convection. *J. Climate*, **12**, 2397-2418.
- Kain J. S., and J. M. Fritsch, 1990: A one-dimensional entraining/detraining plume model and its application in convective parameterization. *J. Atmos. Sci.*, **47**, 2784-2802.
- Kiehl, J. T., 1994: On the observed near cancellation between longwave and shortwave cloud forcing in tropical regions. *J. Climate*, **7**, 559-565.
- Kiehl, J. T., J. J. Hack, G. B. Bonan, B. A. Boville, B. P. Briegleb, D. L. Williamson, P. J. Rasch, 1996: Description of the NCAR Community Climate Model (CCM3). NCAR Tech Note, NCAR/TN-420 + STR, 152 pp.
- Kingsmill, D. E., and R. A. Houze, Jr., 1999: Kinematic characteristics of air flowing into and out of precipitating convection over the west Pacific warm pool: An airborne Doppler radar survey. *Quart. J. Roy. Meteor. Soc.*, **125**, 1165-1207.
- Key, J., 1996, Streamer User's Guide, Technical Report 96-01, Department of Geography, Boston University, 85 pp.
- Klein, Stephen A., and Dennis L. Hartmann, 1993: The Seasonal Cycle of Low Strati-form Clouds. *J. Climate*, **6**, 1587-1606.
- Klemp, J. B., and D. R. Durran, 1983: An upper boundary condition permitting internal gravity wave radiation in numerical mesoscale models. *Mon. Wea. Rev.*, **111**, 430-444.
- Knutson, T. R., and S. Manabe, 1995: Time-Mean Response over the Tropical Pacific to Increased CO₂ in a Coupled Ocean-Atmosphere Model. *J. Climate*, **8**, 2181-2199.
- Knutson, T. R., and S. Manabe, 1998: Model assessment of decadal variability and trends in the tropical Pacific Ocean. *J. Climate*, **11**, 2273-2296.

- Krueger, S. K., and S. M. Lazarus, 1998: Intercomparison of multi-day simulations of convection during TOGA COARE with several cloud-resolving and single-column models. *Proceedings of the Eighth Atmospheric Radiation Measurement (ARM) Science Team Meeting*, Tucson, Arizona, DOE, 391-397.
- Krueger, S. K., and S. M. Lazarus, 1999: Intercomparison of multi-day simulations of convection during TOGA COARE with several cloud-resolving and single-column models. *Preprints, 23rd Conference on Hurricanes and Tropical Meteorology*, Dallas, TX, Amer. Meteor. Soc., 643-647.
- Larson, K. and D. L. Hartmann, 2002a: Interactions among Cloud, Water Vapor, Radiation and Large-scale Circulation in the Tropical Climate Part 1: Sensitivity to Uniform Sea Surface Temperature Changes. *J. Climate*, submitted August 2002.
- Larson, K. and D. L. Hartmann, 2002b: Interactions among Cloud, Water Vapor, Radiation and Large-scale Circulation in the Tropical Climate Part 2: Sensitivity to Spatial Gradients of Sea Surface Temperature. *J. Climate*, submitted August 2002.
- Larson, K., D. L. Hartmann and S. A. Klein, 1999: The Role of Clouds, Water Vapor, Circulation, and Boundary Layer Structure in the Sensitivity of the Tropical Climate. *J. Climate*, **12**, 2359-2374.
- Lau, K. M. and C. H. Sui, M. D. Chou and W. K. Tao, 1994: An inquiry in to the cirrus-cloud thermostat effect for tropical sea surface temperature. *Geo. Res. Lett.*, **21**, 1157-1160.
- Lau, K.-M., H.-T. Wu, and S. Bony, 1997: The Role of Large-Scale Atmospheric Circulation in the Relationship between Tropical Convection and Sea Surface Temperature. *J. Climate*, **10**, 381-392.
- Li, X., C.-H. Sui, K.-M. Lau, and M.-D. Chou, 1999: Large-scale forcing and cloud-radiation interaction in the tropical deep convective regime. *J. Atmos. Sci.*, **56**, 3028-3042.

- Lin, Y.-L., Farley, R. D. and Orville, H. D., 1983: Bulk parameterization of the snow field in a cloud model. *J. Clim. Appl. Meteorol.*, **22**, 1065-1092.
- Lindzen, R. S., 1990: Some coolness concerning global warming. *Bul. Amer. Met. Soc.* **71**, 288-299.
- Lindzen, R. S., M. D. Chou and A. Y. Hou, 2001: Does the earth have an adaptive infrared iris? *Bul. Amer. Met. Soc.* **82**, 417-432.
- Liu, C. and M. W. Moncrieff, 1998: A numerical study of the diurnal cycle of tropical oceanic convection. *J. Atmos. Sci.*, **55**, 2329-2344.
- Manabe, S., and R. T. Wetherald, 1967: Thermal equilibrium of the atmosphere with convective adjustment, *J. Atmos. Sci.*, **24**, 241-259.
- Mapes, Brian E. and Robert A Houze, Jr., 1995: Diabatic divergence profiles in western Pacific mesoscale convective systems. *J. Atmos. Sci.*, **52**, 1807-1828.
- McCaa, J. R., 2001: A New Parameterization of Marine Stratocumulus and Shallow Cumulus Clouds For Climate Models, Ph.D. Dissertation, Department of Atmospheric Sciences, University of Washington, 161 pp.
- McCaa, J., and C. S. Bretherton, 2001: A new parameterization for shallow cumulus convection and its application to marine subtropical cloud-topped boundary layers, Part II: Regional simulations of marine boundary layer clouds. Submitted to *Mon. Wea. Rev.*
- McCaa, J., C. S. Bretherton, and H. Grenier, 2001: A new parameterization for shallow cumulus convection and its application to marine subtropical cloud-topped boundary layers, Part I: Description and 1-D results. Submitted to *Mon. Wea. Rev.*
- Meehl, G. A., W. D. Collins, B. A. Boville, J. T. Kiehl, T. M. L. Wigley, and J. M. Arblaster, 2000: Response of the NCAR climate system model to increased CO₂ and the role of physical processes. *J. Climate*, **13**, 1879-1898.
- Miller, R. L., 1997: Tropical Thermostats and Low Cloud Cover, *J. Climate*, **10**, 409-440.

- Nigam, S., 1997: The Annual Warm to Cold Phase Transition in the Eastern Equatorial Pacific: Diagnosis of the Role of Stratus Cloud-Top Cooling. *J. Climate*, **10**, 2447-2467.
- Ockert-Bell, M. E. and D. L. Hartmann, 1992: The effect of cloud type on Earth's energy balance: Results for selected regions. *J. Climate*, **5**, 1157-1171.
- Peixoto, J. P., and A. H. Oort, 1992: Physics of Climate. Amer. Inst. Phys., 520 pp.
- Philander, S. G. H., D. Gu, D. Halpern, G. Lambert, N.-C. Lau, T. Li, and R. C. Pacanowski, 1996: Why the ITCZ is Mostly North of the Equator. *J. Climate*, **9**, 2958-2972.
- Pierrehumbert, R. T., 1995: Thermostats, Radiator Fins, and the Local Runaway Greenhouse. *J. Atmos. Sci.*, **52**, 1784-1806.
- Ramanathan, V., and W. Collins, 1991: Thermodynamic regulation of ocean warming by cirrus clouds deduced from the 1987 El Nino. *Nature*, **351**, 27-32.
- Raval, A. and V. Ramanathan, 1989: Observational determination of the greenhouse effect. *Nature*, **342**, 758-761.
- Reisner, J., R. M. Rasmussen, and R. T. Brintjes, 1998: Explicit forecasting of super-cooled liquid water in winter storms using the MM5 mesoscale model. *Quart. J. Roy. Meteor. Soc.*, **124 B**, 1071-1107.
- Reynolds, R. W. and T. M. Smith, 1995: A high-resolution global sea surface temperature climatology. *J. Climate*, **8**, 1571-1583.
- Robe, F. R. and K. A. Emanuel, 1996: Moist convective scaling: some inferences from three-dimensional cloud ensemble simulations. *J. Atmos. Sci.*, **53**, 3265-3275.
- Rossow W. B. and R. A. Schiffer, 1999: Advances in understanding clouds from ISCCP. *Bull. Amer. Soc.*, **80**, 2261-2287.
- Rozendaal, M. A., and C. B. Leovy and S. A. Klein, 1995: An Observational Study of Diurnal Variations of Marine Stratiform Cloud. *J. Climate*, **8**, 1795-1809.
- Rutledge, S. A. and Hobbs, P. V., 1983: The mesoscale and microscale structure and organization of clouds and precipitation in midlatitude cyclones. Part XII: A

- diagnostic modeling study of precipitation development in narrow cold-frontal rain bands. *J. Atmos. Sci.*, **41**, 2949-2972.
- Salathe, E. P. and D. L. Hartmann, 1997: A Trajectory Analysis of Tropical Upper-Tropospheric Moisture and Convection. *J. Climate*, **10**, 2533-2547.
- Schiffer, R. A. and W. B. Rossow, 1985: ISCCP global radiance data set: a new resource for climate research. *Bull. Amer. Meteor. Soc.* **66**, 1498-505.
- Schubert, Wayne H., Paul E. Ciesielski, Chungu Lu, and Richard H. Johnson, 1995: Dynamical Adjustment of the Trade Wind Inversion Layer. *J. Atmos. Sci.*, **52**, 2941 -2952.
- Schneider, Edwin K., 1977: Axially symmetric steady-state models of the basic state for instability and climate studies, Part II, Nonlinear calculations. *J. Atmos. Sci.*, **34**, 280-296.
- Shine, K. P. and A. Sinha, 1991: Sensitivity of the Earth's climate to height-dependent changes in the water vapor mixing ratio. *Nature*, **354**, 382-4.
- Sobel A. H., J. Nilsson and L. M. Polvani 2001: The weak temperature gradient approximation and balanced tropical moisture waves. *J. Atmos. Sci.*, **58**, 3650-3665.
- Stephens, G. L., 1990: On the relationship between water vapor over the oceans and sea surface temperature. *J. Climate*, **3**, 634-645.
- Su, H., S. S. Chen, and C. S. Bretherton, 1999: Three-dimensional week-long simulations of TOGA-COARE convective systems using the MM5 mesoscale model. *J. Atmos. Sci.*, **56**, 2326-2344.
- Sui, C.-H., K.-M. Lau, X. Li, and M.-D. Chou, 2000: A Regulation of tropical climate by radiative cooling as simulated in a cumulus ensemble model. Submitted to *J. Climate*, 2000.
- Sui, C. H., K. M. Lau, W. K. Tao, M. D. Chou, and J. Simpson, 1993: Simulated water and radiation budgets in the Tropics. Preprints, *20th Conf. on Hurricanes and Tropical Meteorology*, San Antonio, TX, Amer. Meteor. Soc., 431-434.

- Sui, C. H., K. M. Lau, W. K. Tao, and J. Simpson, 1994: The tropical water and energy cycles in a cumulus ensemble model. Part 1: Equilibrium climate. *J. Atmos. Sci.*, **51**, 711-728.
- Sun, D.-Z., and R. S. Lindzen, 1993: Distribution of tropical tropospheric water vapor. *J. Atmos. Sci.*, **50**, 1643-1660.
- Sun, De-Zheng and Zhengyu Liu, 1996: Dynamic Ocean-Atmosphere Coupling: A Thermostat for the Tropics. *Science*, **22**, 1148-1150.
- Tompkins, A. M., and G. C. Craig, 1999: Sensitivity of tropical convection to sea surface temperature in the absence of large-scale flow. *J. Climate*, **12**, 462-476.
- Udelhofen, P., and D. L. Hartmann, 1995: Influence of tropical convective cloud systems on the relative humidity in the upper troposphere. *J. of Geophys. Res.*, **100**, 7423-7440.
- Wallace, John M., 1992: Effect of deep convection on the regulation of tropical sea surface temperature. *Nature*, **357**, 230-231.
- Weaver, C. P., W. D. Collins, and H. Grassel, 1994: Relationship between clear-sky atmospheric greenhouse effect and deep convection during the Central Equatorial Pacific Experiment: Model calculations and satellite observations. *J. Geophys. Res.*, **99**, 25 891 - 25 901.
- Wu, X., W. W. Grabowski, and M. W. Moncrieff, 1998: Long-term behavior of cloud systems in TOGA COARE and their interactions with radiative and surface processes. Part 1: two-dimensional modeling study. *J. Atmos. Sci.*, **55**, 2693-2714.
- Xu, Kuan-Man and Kerry A. Emanuel, 1989: Is the tropical atmosphere conditionally unstable? *Mon. Wea. Rev.*, **117**, 1471-1479.
- Xu, K.-M., and D. Randall, 1999: A sensitivity study of radiative-convective equilibrium in the tropics with a convection -resolving model. *J. Atmos. Sci.*, **56**, 3385-3399.

- Xu, K.-M., A. Arakawa, and S. K. Krueger, 1992: The Macroscopic Behavior of Cumulus Ensembles Simulated by a Cumulus Ensemble Model. *J. Atmos. Sci.*, **49**, 2402-2420.
- Yang, H. and R. T. Pierrehumbert, 1994: Production of dry air by isentropic mixing. *J. Atmos. Sci.*, **51**, 3437-3454.
- Yano, J.-I., M. W. Moncrieff and W. W. Grabowski, 2002: Walker-Type Mean Circulation and Convectively Coupled Tropical Waves as an Interacting System. *J. Atmos. Sci.*, **59**, 1566-1577.
- Yano, J.-I., W. W. Grabowski, and M. W. Moncrieff, 2002: Mean-State Convective Circulations over Large-Scale Tropical SST Gradients. *J. Atmos. Sci.*, **59**, 1578-1592.
- Yin, B. and B. A. Albrecht, 2000: Spatial Variability of Atmospheric Boundary Layer Structure over the Eastern Equatorial Pacific. *J. Climate*, **13**, 1574-1592.
- Zhang, Guang Jun and Michael J. McPhaden, 1995: The Relationship between Sea Surface Temperature and Latent Heat Flux in the Equatorial Pacific. *J. Climate*, **8**, 589-605.

Vita

Kristin Ann Larson was born a twin in Washington, D. C. on May 15, 1972. She attended Boulder High School in Boulder, Colorado, until her graduation in 1990. She went on to college, and in 1994 received her Bachelor of Science in Engineering degree in Mechanical and Aerospace Engineering from Princeton University in Princeton, New Jersey.